eshre
SCIENCE MOVING
PEOPLE
MOVING SCIENCE

OXFORD
UNIVERSITY PRESS

molecular
human
reproduction

ORIGINAL ARTICLE

Isoform-specific GSK3A activity is negatively correlated with human sperm motility

M.J. Freitas[1], J.V. Silva[1,2,3], C. Brothag[4], B. Regadas-Correia[5,6,7], M. Fardilha ![ORCID] [1,*], and S. Vijayaraghavan[4]

[1]Signal Transduction Laboratory, Institute for Research in Biomedicine—iBiMED, Medical Sciences Department, University of Aveiro, Aveiro, Portugal [2]Reproductive Genetics & Embryo-fetal Development Group, Institute for Innovation and Health Research (I3S), University of Porto, Porto, Portugal [3]Department of Microscopy, Laboratory of Cell Biology, and Unit for Multidisciplinary Research in Biomedicine (UMIB), Institute of Biomedical Sciences Abel Salazar (ICBAS), University of Porto, Porto, Portugal [4]Kent State University, Kent, OH 44242, USA [5]CNC.IBILI—Institute for Biomedical Imaging and Life Sciences, Faculty of Medicine, University of Coimbra, Coimbra, Portugal [6]CIBIT—Coimbra Institute for Biomedical Imaging and Translational Research, University of Coimbra, Coimbra, Portugal [7]Department Quantitative Methods and Information and Management Systems, Coimbra Business School, Coimbra, Portugal

*Correspondence address. Signal Transduction Laboratory, Institute for Research in Biomedicine—iBiMED, Medical Sciences Department, University of Aveiro, Aveiro, Portugal. Tel: +351-234-247-242; E-mail: mfardilha@ua.pt ![ORCID] orcid.org/0000-0001-7459-9173

Submitted on December 6, 2018; resubmitted on January 29, 2019; editorial decision on February 18, 2019; accepted on February 19, 2019

In mouse and bovine sperm, GSK3 activity is inversely proportional to motility. Targeted disruption of the GSK3A gene in testis results in normal spermatogenesis, but mature sperm present a reduced motility, rendering male mice infertile. On the other hand, GSK3B testis-specific KO is fertile. Yet in human sperm, an isoform-specific correlation between GSK3A and sperm motility was never established. In order to analyze GSK3 function in human sperm motility, normospermic and asthenozoospermic samples from adult males were used to correlate GSK3 expression and activity levels with human sperm motility profiles. Moreover, testicular and sperm GSK3 interactomes were identified using a yeast two-hybrid screen and coimmunoprecipitation, respectively. An extensive *in-silico* analysis of the GSK3 interactome was performed. The results proved that inhibited GSK3A (serine phosphorylated) presents a significant strong positive correlation ($r = 0.822$, $P = 0.023$) with the percentage of progressive human sperm, whereas inhibited GSK3B is not significantly correlated with sperm motility ($r = 0.577$, $P = 0.175$). The importance of GSK3 in human sperm motility was further reinforced by *in-silico* analysis of the GSK3 interactome, which revealed a high level of involvement of GSK3 interactors in sperm motility-related functions. The limitation of techniques used for GSK3 interactome identification can be a drawback, since none completely mimics the physiological environment. Our findings prove that human sperm motility relies on isoform-specific functions of GSK3A within this cell. Given the reported relevance of GSK3 protein–protein interactions in sperm motility, we hypothesized that they stand as potential targets for male contraceptive strategies based on sperm motility modulation.

Key words: sperm motility / sperm biochemistry / interactome / GSK3

Introduction

Glycogen synthase kinase 3 (GSK3), a serine/threonine kinase, has been involved in a wide range of cellular processes such as apoptosis, mitosis and proliferation (Kaidanovich-Beilin and Woodgett, 2011; Beurel *et al.*, 2015). Moreover, deregulation of GSK3 functions has been associated with pathological conditions such as cancer, Alzheimer's disease and diabetes (Amar *et al.*, 2011; Gao *et al.*, 2011). GSK3 is ubiquitously expressed and is encoded by two genes giving rise to two isoforms: GSK3A and GSK3B. The isoforms differ in their N-termini, with GSK3A having a unique glycine-rich N-terminus which is highly conserved in mammals, suggesting an isoform-specific function (Azoulay-Alfaguter *et al.*, 2011).

GSK3 plays a central role in the male reproductive system. In mouse testis, GSK3A is expressed in the seminiferous tubules and its expression increases during the onset of spermatogenesis, peaking in the adult testis (Bhattacharjee *et al.*, 2015). GSK3B expression is present in cells entering meiosis, spermatids and Sertoli cells (Guo *et al.*, 2003). Curiously, targeted disruption of GSK3A gene in testis, results in normal spermatogenesis, but the mature sperm present a reduced motility and metabolism, rendering male mice infertile (Bhattacharjee *et al.*, 2015, 2018). On the other hand, the GSK3B testis-specific knock-out was fertile (Bhattacharjee *et al.*, 2018). In mouse and bovine sperm, GSK3 activity is inversely proportional to sperm motility and in immotile caput sperm, GSK3 activity is six times higher than that of motile caudal sperm (Vijayaraghavan *et al.*, 1996, 2000). GSK3 activity

is controlled by its phosphorylation state. When serine phosphorylated, GSK3 catalytic activity is low (GSK3A Ser9 and GSK3B Ser21) but when tyrosine phosphorylated, it is activated (GSK3A Tyr 279 and GSK3B Tyr 216) (Wang *et al.*, 1994).

Although in bovine and mouse, the role of GSK3 in male fertility is well established, in human sperm the knowledge is limited. With that in mind, we performed a GSK3 characterization, by determining its activity levels in asthenozoospermic and normozoospermic ejaculated human samples and its subcellular location in human sperm. The observation that mouse GSK3B cannot substitute for GSK3A implies that GSK3A is essential for normal sperm physiology. We considered that the unique role of GSK3A in sperm motility is reliant on its interactors and, as such, identified the GSK3A and GSK3B interactomes in both human testis and sperm.

Materials and Methods

Ethical approval

This study was approved by the Ethics and Internal Review Board of the Hospital Infante D. Pedro E.P.E. (Aveiro, Portugal) (Process number: 36/AO) and was conducted in accordance with the ethical standards of the Helsinki Declaration. All donors signed an informed consent forms allowing the samples to be used for scientific purposes.

All procedures using mice were performed at the Kent State University animal facility and were approved by the National Institute of Environmental Health Sciences institutional Animal Care and Use Committee (IACUC) and the Kent State Animal Ethics Committee under the IACUC protocol number 362DK 13-11. Immediately after CO_2 euthanization, testis and epididymis of 3–4-month-old CD1 mice (*Mus musculus*) were removed.

Sperm extracts

Human ejaculate semen samples were obtained from healthy donors by masturbation into a sterile container. Basic semen analysis was performed by qualified technicians according to World Health Organization (WHO) guidelines (Organization, 2010). There was no significant presence of non-sperm cells in the sample (round cells $<1.0 \times 10^6$ cells/mL). After semen liquefaction, sperm cells were washed in phosphate buffered saline (PBS1x, Fisher Scientific, Loures, Portugal).

Immunoblotting

Washed human sperm were lysed in either: Tris buffer (20 mM Tris–HCl, pH 7.4, 1 mM EDTA, 1 mM EGTA) (Fisher Scientific); 1xRIPA (0.05 M Tris–HCl, pH 7.4, 0.150 M NaCl, 0.25% deoxycholic acid, 1% NP-40, 1 mM EDTA) (Millipore Iberica, Madrid, Spain); 1xRIPA modified (0.05 M Tris–HCl, pH 7.4, 0.150 M NaCl, 0.25% deoxycholic acid, 2% NP-40, 1 mM EDTA); or 1%SDS (Fisher Scientific, Loures, Portugal), for 30 min on ice and centrifuged at 16 000 *g*, 15 min, 4°C. The supernatant was recovered (protein extract). Mouse sperm cells and testis were lysed in 1xRIPA, centrifuged at 16 000 *g*, 15 min, 4°C and the protein extract was recovered. Human testis protein extract was acquired from Takara, Enzifarma, Lisboa, Portugal (ref: 635 309).

Sperm protein extracts were mass normalized using BCA assay (ref: 23 225, Pierce, Fisher Scientific) separated by SDS-PAGE and electrotransfered to a nitrocellulose membrane. Afterwards, the membrane was incubated with one of the following antibodies: mouse anti-GSK3A/B (Invitrogen, Fisher Scientific, ref: 44-610, 1:2000) rabbit anti-GSK3A (Cell Signaling Technology, Danvers, MA, USA, ref: #9338, 1:1000) rabbit anti-GSK3B (Cell Signaling ref: #9315, 1:1000); mouse anti-GSK3A pS21 (Santa Cruz Technologies, Heidelberg, Germany, ref: sc-365 483, 1:1000); mouse anti-GSK3B pS9 (Santa Cruz Technologies ref: sc-373 800, 1:1000) and rabbit anti-LRP6 (Cell Signaling, ref: #2560, 1:1000), 4°C, ON. Finally, the membrane was incubated with the appropriate infrared secondary antibody (1:5000, Li-Cor Biosciences UK Ltd, Cambridge, UK). The images were obtained using Odyssey Infrared Imaging Bands System (Li-Cor Biosciences). Bands were quantified with the Quantity One 1-D Analysis Software (Bio-Rad, Amadora, Portugal). Phosphoserine GSK3 levels were calculated by determining the ratio between phosphoserine signal and total GSK3 signal. GSK3 levels were normalized to the loading control Ponceau S. The statistical measures used were the mean and SEM. A test of normality (Shapiro–Wilk test) was performed to assess normality of quantitative variables. The Pearson correlation coefficient *r* was determined to assess the relationship between two variables. Statistical analysis was conducted using the Statistical Package for Social Sciences, version 19 (SPSS®, Chicago, IL, USA). The significance level was set at 0.05.

Immunocytochemistry

Washed human sperm were spread onto a glass coverslip, allowed to dry and fixed in 4% formaldehyde (Fisher Scientific) for 10 min. Afterwards, sperm were permeabilized in 0.1% Tween (Fisher Scientific) in 1% goat serum (Sigma-Aldrich Química, S.A., Sintra) and 5% BSA (NZYTech, Lisboa, Portugal) for 20 min. Blocking was performed with 1% goat serum and 5% BSA for 1 h 30 min and then incubated with primary antibodies: rabbit anti-GSK3A (Cell Signaling ref: #9338, 1:50) or rabbit anti-GSK3B (Cell Signaling ref: #9315, 1:50) overnight at 4°C; or rabbit anti-LRP6 (Cell Signaling, ref: #2560, 1:50), rabbit anti-pLRP6 1490 (Cell Signaling, ref: #2568, 1:50) or rabbit anti-AKAP11 (Invitrogen, Fisher Scientific, ref: PA5-39 868, 1:100) for 1 h 20 min. The sperm cells were incubated with anti-rabbit Alexa 594 nm (Life Technologies S.A., Madrid, Spain, 1:800) for 45 min at room temperature. Coverslips were washed in PBSx1 + 0.1% Tween, followed by one wash step in PBS1x. Finally, Hoechst was added, and coverslips were mounted onto a glass slide with ProLong™ Gold Antifade Mountant (Invitrogen, Fisher Scientific, ref: 10 144). Negative controls were processed in parallel. Fluorescence images were obtained using an Imager.Z1, Axio-Cam HRm camera and AxioVision software (Zeiss, Jena, Germany). Three normospermic human sperm samples were analyzed and around 100 cells per sample were assessed.

Yeast two-hybrid screen

Homo Sapiens GSK3A (NM_019 884.2) was subcloned using EcoRI and BamHI (New England Biolabs, Herts, UK) and Homo Sapiens GSK3B (NM_002 093.3) was subcloned using NdeI and SalI (New England Biolabs) into pAS2-1 plasmid. Both vectors were sequenced to ensure that GSK3A and GSK3B were in frame with Gal-AD. The pAS2-1-GSK3A and pAS2-1-GSK3B vectors were transformed into AH109 yeast strain by a standard lithium acetate method (Clontech, Takara). GSK3A and GSK3B are not cytotoxic to AH109 yeast cells. Expression of GSK3A and GSK3B was confirmed and both proteins did not activate the reporter genes per se (Supplementary Fig. S1). For library screening, AH109 transformed with either pAS2-1-GSK3A or pAS2-1-GSK3B was mated with yeast strain Y187 expressing human testis cDNA library in pGADT7-Rec (Mate&Plate Library—Human testis ref. 630 470, Clontech, Takara) according to manufacture instructions. Half of the mating mixture was plated onto high-stringency medium (Quadruple dropout medium: SD/-Ade/-His/-Leu/-Trp) and the other half was placed onto low-stringency medium (Triple dropout medium: SD/-His/-Leu/-Trp) and the plates were incubated at 30°C. Colonies obtained in the low-stringency plates were replica plated onto medium with X-A-Gal and incubated at 30°C to check for MEL-1 expression (blue color colonies).

For GSK3A, 93 positive clones were obtained from a total 2.64×10^7 screened clones. For GSK3B, 54 positive clones were obtained from a total of 2.75×10^7 screened clones. The Matchmaker Insert Check PCR mix 2 (Clontech, Takara, ref:630 497) was used to identify positive clone cDNA. DNA sequences were compared to the GeneBank database to identify the corresponding protein.

Coimmunoprecipitation

Sperm cells (50×10^6) were lysed in 1xRIPA, supplemented with 1 mM of Phenylmethylsulfonyl fluoride (PMSF) (Fisher Scientific) and 0.2 mM of sodium orthovanadate (Na_3VO_4) (Fisher Scientific) for 60 min on ice and centrifuged at 16 000 g, 4°C, 15 min. Sperm extracts were pre-cleared using Dynabeads Protein G (ref: 10 003D, Invitrogen, Fisher Scientific) and incubated with either rabbit anti-GSK3A (Cell Signaling ref: #9338, 1:50), rabbit anti-GSK3B (Cell Signaling ref: #9315, 1:50) or rabbit anti-IgG (ref: sc-2027, Santa Cruz Technologies) at 4°C ON with rotation. After incubation, 50 μL of dynabeads were added and incubated for 2 h. After washing with PBS1x, the dynabeads were resuspended in 50 mM glycine (Fisher Scientific) for 5 min. Finally, the supernatant was recovered and 1%SDS was added to the dynabeads, which were incubated 5 min, boiled and recovered.

Alternatively, GSK3 antibodies were crosslinked using BS3 (bis(sulfosuccinimidyl)suberate) (Invitrogen, Fisher Scientific, ref: 21 580) to Dynabeads Protein G, according to manufacturer instructions. Sperm extracts were pre-cleared and incubated with crosslinked beads for 1 h. After washing, the beads were resuspended in trypsin digestion buffer (20 mM Tris–HCl pH 8.0, 2 mM $CaCl_2$).

Mass spectrometry

Mass spectrometry studies of GSK3 human sperm interactors were performed in two facilities (two distinct samples).

In the Lerner Research Institute's Proteomics and Metabolomics Laboratory, the LC–MS system was a Dionex Ultimate 3000 nano-flow HPLC interfacing with a Finnigan Orbitrap LTQ Elite hybrid ion trap mass spectrometer system. The HPLC system used an Acclaim PepMap 100 precolum (75 μm × 2 cm, C18, 3 μm, 100 A) followed by an Acclaim PepMap RSLC analytical column (75 μm × 15 cm, C18, 2 μm, 100 A). The data was analyzed by using all CID spectra collected in the experiment to search the human UniProtKB protein database with the search programs, Sequest and Mascot. Only results with mascot score $P < 0.05$ and at least two identifying peptides with mascot ion scores of at least 40 were considered. Specifically, GSK3A and GSK3B sequences searches were performed in the Sequest program.

In the VIB Proteomics Core Facility, the LC–MS-MS system was Ultimate 3000 RSLCnano system in-line connected to a Q Exactive mass spectrometer (Thermo, Fisher Scientific, Loures, Portugal). Peptides were loaded on a reverse-phase column (made in-house, 75 μm I.D. × 20 mm, 3 μm beads C18 Reprosil-Pur, Dr. Maisch). Each sample was injected three times and analyzed in triplicate. Data analysis was performed with MaxQuant (version 1.5.6.5) (Cox and Mann, 2008), using the Andromeda search engine on default search settings, including a false discovery rate of 1% at both the peptide and protein levels. The spectra were searched against human proteins in the UniProtKB database (release version January 2017), with only proteins containing at least one unique or razor peptide being retained. Proteins were quantified by the MaxLFQ algorithm integrated in the MaxQuant software (Cox et al., 2014), with quantification requiring a minimum ratio count of two unique or razor peptides. Further data analysis was performed with the Perseus software (version 1.5.5.3) (Tyanova et al., 2016) after uploading the protein groups file from MaxQuant. Proteins were identified by site, reverse database hits and contaminants were removed, and the technical replicate samples of GSK3A,

GSK3B and the negative control were grouped. Proteins with fewer than three valid values in at least one group were removed and the missing values were imputed from a normal distribution around the detection limit. Finally, t-tests were performed (FDR = 0.0001 and S0 = 5) to compare samples of GSK3A and GSK3B with the negative control (Silva et al., 2017).

In-silico analysis

Either UniProtKB or FASTA sequence was retrieved for all GSK3 interactors and used for subsequent in-silico analysis (only Homo sapiens information was considered). The presence of GSK3 consensus phosphorylation site (xxx[ST]xxx[ST]P) (Wu et al., 2009) was analyzed in: Eukaryotic Linear Motif (ELM) resource (Dinkel et al., 2016); PhosphoSitePlus (Hornbeck et al., 2015); Kinase Net (http://www.kinasenet.ca); NetPhos 3.1 Server (Blom et al., 2004); ScanProsite (de Castro et al., 2006); and GPS 3.0 (Xue et al., 2011). Only data obtained with high threshold, high conservation scores and reported in at least three tools were considered. GSK3A and GSK3B interactomes were retrieved from IMEx-curated databases (Orchard et al., 2012) and Human Integrated Protein–Protein Interaction rEference (HIPPIE) database (Alanis-Lobato et al., 2017). Only interactions for human GSK3A and GSK3B with human proteins were considered (March 2018).

Gene expression patterns (mRNA) for all interactors (whether identified in this study or obtained from databases) were retrieved from: The Human Protein Atlas (Uhlén et al., 2015); Pattern Gene Database (PaGenBase) (Pan et al., 2013) Expression atlas EMBL-EBI (68 FANTOM5 project-adult; 32 Uhlen´s Lab and GTEx) (Petryszak et al., 2014); BioGPS (Wu et al., 2016); and UniGene (Pontius et al., 2003). mRNA expression values for all databases (Transcripts per million or fragments per kilobase of exon model per million mapped reads) were retrieved and testis expression values were normalized by calculating the percentage of testis expression taking into account the expression of all tissues. Only interactors that presented more than 50% of expression in testis in at least two databases used were considered highly expressed in testis and were classified in three categories: 50–75%, 75–90% and >90%. Differently expressed proteins in asthenozoospermic samples were collected from peer reviewed papers and compared with GSK3 interactors (Cai et al., 2006; Chen et al., 2009; An et al., 2011; Jing et al., 2011; Li et al., 2010, 2011; Shen et al., 2013b; Amaral et al., 2014; Bhagwat et al., 2014; Salvolini et al., 2014; Hashemitabar et al., 2015; Zhou et al., 2015; Saraswat et al., 2017).

Phenotypes associated with all interactors (genes) were retrieved form Mouse Genome Informatics (MGI) (Eppig et al., 2015) and OMIM (Amberger et al., 2015). Manually curated genes associated with phenotypes of male infertility retrieved from DisGeNet (Piñero et al., 2017), Phenopedia (Yu et al., 2010) and DISEASE database. Altered accessory glands, genetic disorders, sexual behavior and tumor incidence were excluded. Also, GSK3A and GSK3B interactors annotated to testis and sperm physiology on GeneOntology enrichment tool (PANTHER version 12.0, 25 August 2017) (Gene Ontology Consortium, 2015) were classified according to those annotations. GSK3A and GSK3B protein–protein interaction (PPIs) networks were built using Cytoscape v 3.6.0 (Shannon et al., 2003). The inner connections between those proteins were captured. To construct sperm motility and testis related GSK3A and GSK3B PPI networks, GSK3A and GSK3B interactors associated with sperm motility and testis phenotypes were extracted from GSK3A and GSK3B interactome network.

Statistical analysis

The statistical measures used were the mean and SEM. A test of normality (Shapiro–Wilk test) was performed to assess normality of quantitative

variables. The Pearson correlation coefficient, r, was determined to assess the relationship between two variables. Statistical analysis was conducted using the Statistical Package for Social Sciences, version 19 (SPSS®, Chicago, IL, USA). The significance level was set at 0.05.

Results

GSK3A is required for human progressive spermatozoa motility

Characterization of GSK3 in mouse, bovine and primates sperm is well stablished (Smith *et al.*, 1999; Vijayaraghavan *et al.*, 1996, 2000). Yet, in human spermatozoa, characterization of GSK3 is deficient. We evaluated the expression and activation of both GSK3 isoforms in human testis and ejaculated human sperm (Fig. 1).

Figure 1A shows that GSK3A and GSK3B were expressed in human testis and sperm, similar to what was previously described in mouse and bovine. The levels of inhibited GSK3A and GSK3B (serine phosphorylation) were assessed in human testis and sperm. In human testis, no serine phosphorylated GSK3 was detected, while in human sperm both phosphorylated GSK3 isoforms were detected (Fig. 1A). Moreover, different lysis-buffer strength recovered different amounts of GSK3 in human sperm (Supplementary Fig. S2).

To assess the correlation between GSK3 activity with ejaculated sperm motility, total and serine phosphorylated GSK3A and GSK3B (low activity) were evaluated in normospermic and asthenozoospermic samples (see Supplementary Table SI for sample information). Total GSK3A and serine phosphorylated GSK3A levels appear to be lower in asthenozoospermic samples compared to normospermic (Fig. 1B and C), while expression of total and serine phosphorylated GSK3B appeared to be similar in both normospermic and asthenozoospermic samples (Fig. 1B and C). Also, Fig. 1D shows that there was a significant strong positive correlation ($r = 0.822$, $P = 0.023$) between the percentage of progressive sperm and the levels of inhibited GSK3A, whereas inhibited GSK3B was not significantly correlated with sperm motility ($r = 0.577$, $P = 0.175$). Although the levels of total GSK3 were not significantly correlated with the percentage of progressive motility, GSK3A presented an apparent positive correlation with the percentage of progressive motile spermatozoa (Fig. 1E). The correlation between GSK3 levels and the percentage of immotile spermatozoa was also analyzed, and the results comply with that previous described (Supplementary Table SII).

GSK3A and GSK3B have distinct distributions in human spermatozoa

The subcellular localization of GSK3A and GSK3B in ejaculated human sperm was analyzed. Figure 2 shows that GSK3A was primarily located in the flagellum (98.0%) and 75.7% of sperm cells also showed immunoreactivity in the head. Curiously, 24.2% of the spermatozoa showed a strong immunoreactivity for GSK3A in the equatorial region, particularly at the edges. In contrast, GSK3B was mainly located in the sperm head (97.0%); 23.9% of sperm showed GSK3B distributed throughout the entire head and flagellum and in 76.0% of sperm cells, it was present only in the sperm head (Fig. 2). Within the flagellum, both GSK3A and GSK3B present a punctate like staining.

## GSK3 human testis and sperm interactome

A yeast two-hybrid screen of a human cDNA testis library revealed 46 putative interactors for GSK3A and 21 for GSK3B (Supplementary Tables SIII and SIV, respectively). For GSK3A, 76% were new putative interactors while 24% were previously described as GSK3 interactors. Of GSK3A interactors identified, 58.7% contained the GSK3 consensus phosphorylation site (xxx[ST]xxx[ST]P). Finally, 34.8% of GSK3A interactors were already described to be present in either testis and/or sperm of mammals. For GSK3B, 77.8% were identified for the first time as GSK3B putative interactors. Around 38% of the GSK3B identified interactors had the GSK3 consensus phosphorylation site and 61.1% were previously reported to be present in testis and/or sperm of mammals.

GSK3A and GSK3B interactors were isolated from ejaculated human sperm by coimmunoprecipitation using isoform-specific GSK3 antibodies in two independent experiments by mass spectrometry analysis. Endogenous GSK3A and GSK3B were successfully immunoprecipitated in both experiments (Supplementary Fig. S3) and five GSK3A peptides and four GSK3B peptides were identified in mass spectrometry (Supplementary Table SV). Note that neither GSK3A nor GSK3B were detected in the negative control. There were 17 and 34 interactors identified as sperm GSK3A and GSK3B interactors, respectively (Supplementary Tables SVI and SVII, respectively). Regarding GSK3A interactors, 82.4% were potentially novel interactors and 17.6% contained the GSK3 consensus phosphorylation site. Also, 58.8% of GSK3A identified interactors were described as expressed in either mammalian testis and/or sperm by previous studies. For GSK3B interactors, 85.3% were new putative interactors and 47.1% were shown to be expressed in either mammalian testis and/or sperm. Finally, the GSK3 consensus phosphorylation site was present in 14.7% of GSK3B interactors.

GSK3 interactomes are associated with sperm motility and testis functions

To enrich the GSK3 human testis and spermatozoa interactome, GSK3A and for GSK3B interactomes were retrieved from public available databases; 75 GSK3A interactors and 413 GSK3B had been previously identified (Supplementary Tables SVIII and SIX, respectively). With the goal of identifying key GSK3 interactors for sperm and testis physiology, gene expression for GSK3 interactors was retrieved from five different tissue-expression databases (Supplementary Tables SVIII and SIX). Four GSK3A interactors are testis-enriched, with more than 90% of their expression restricted to testis: DDI1, GOLGA6C (testis interactors), ACR and PRSS37 (sperm interactors). Although not testis-enriched, TTC16 expression is enhanced in testis (Supplementary Table SX). For GSK3B interactors, besides ACR and PRSS37, TEKT5, CMTM2 (testis interactors), HIST1H1T, PRKACG, TSKS (databases interactors) were classified as highly enriched in testis and CABYR expression is enhanced in testis (Supplementary Table SX). To further characterize the GSK3 interactome, differently expressed proteins in asthenozoospermic samples were retrieved from the proteomics studies. Overall, eleven GSK3 testis or sperm interactors are increased, eight are decreased and one has conflicting reports in asthenozoospermic samples (Supplementary Tables SIII, SIV, SVI and SVII).

PPI networks were constructed using data obtained from this study and retrieved from databases. The GSK3A interactome network
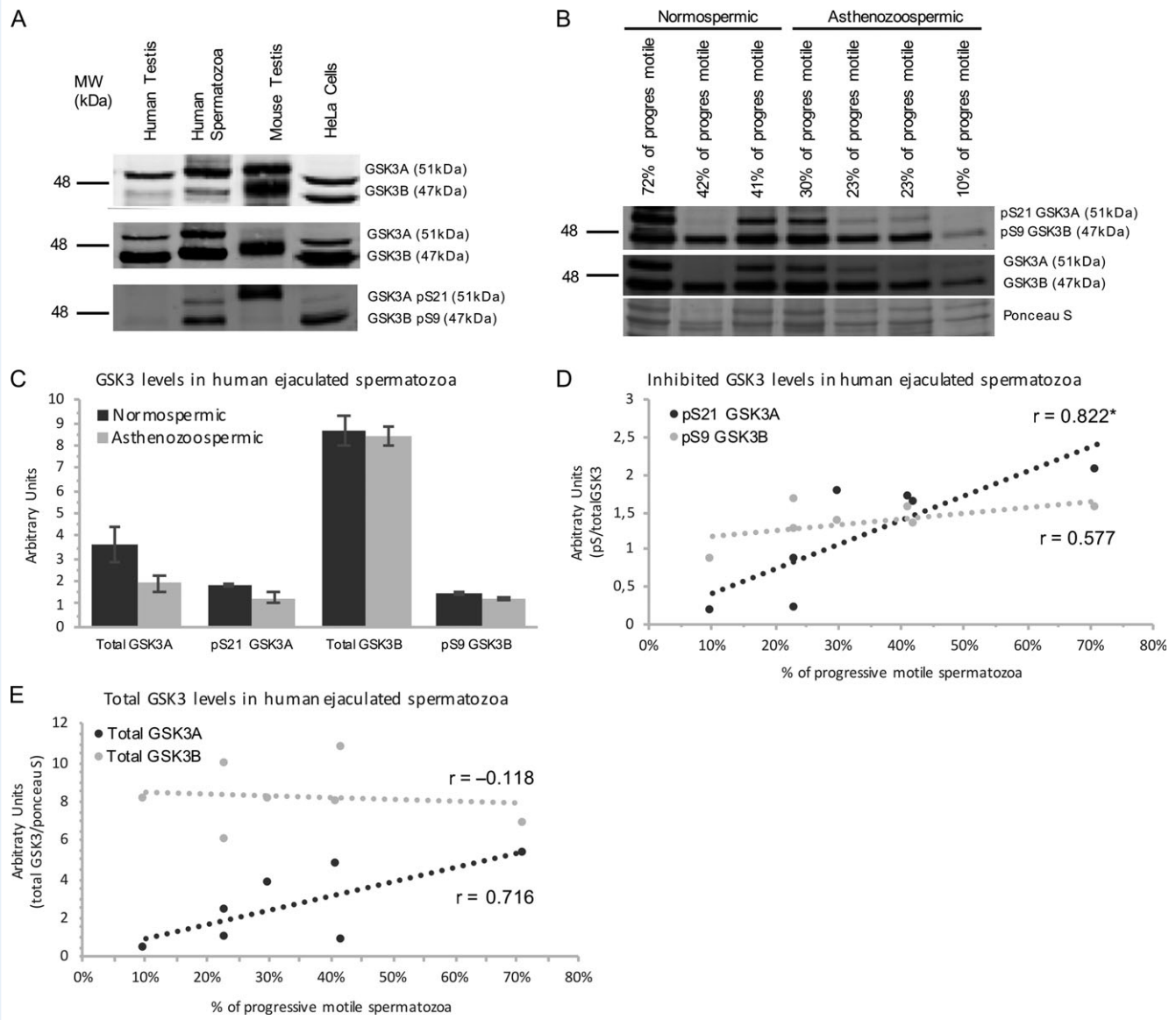
Figure 1 GSK3 in human testis and spermatozoa and correlation with sperm motility. (**A**) Western blot analysis of total GSK3 and serine phosphorylated GSK3 isoforms in human testis and spermatozoa, mouse testis and HeLa cells; 30 μg of protein obtained in RIPA1x were loaded per sample. From top to bottom, GSK3 was immunodetected with the following antibodies: anti-GSK3A/B antibody, anti-GSK3A antibody and anti-GSK3B antibody, anti-GSK3A pS21 and anti-GSK3B pS9. (**B**) Immunoblot of total and serine phosphorylated GSK3 isoforms in human normospermic ($n = 3$) and asthenozoospermic ($n = 4$) ejaculated spermatozoa. (**C**) Total and serine phosphorylated GSK3 isoforms protein levels in human normospermic and asthenozoospermic (bar chart with error bars (SEM)). (**D**) Pearson Correlation between the percentage of progressive motile ejaculated sperm and protein levels of serine phosphorylated GSK3A and GSK3B (scatter plot with regression line). (**E**) Pearson Correlation between the percentage of progressive motile ejaculated sperm and protein levels of total GSK3A and GSK3B. Blots were cropped. *Correlation is statistically significant at the 0.05 level.

(Supplementary Fig. S4) presents 130 proteins, including GSK3A. Between GSK3A interactors, 257 interactions are formed. The GSK3B interactome is composed by 456 proteins that form 1813 interactions among them (data not shown).

To add biological meaning to the GSK3 interactome, phenotype and Gene Ontology information were retrieved (Supplementary Tables SXI and SXII). Here, two subnetworks were extracted: sperm motility-related and testis-related GSK3-based networks. Of the GSK3A interactors, 26 have been associated with motility-related functions, phenotypes and/or subcellular locations (Fig. 3). From those, five (PRSS37, DRC1, RPS19, HSPA5 and AP3D1) were identified in this study as GSK3A interactors and only one was classified as testis-enriched protein (PRSS37). PRKACA and DRC1 stand out by presenting five motility-related annotations followed by GLI3 with four such annotations. Note that GSK3A itself has been associated with locomotion and cell motility processes. For GSK3B, 100 interactors are
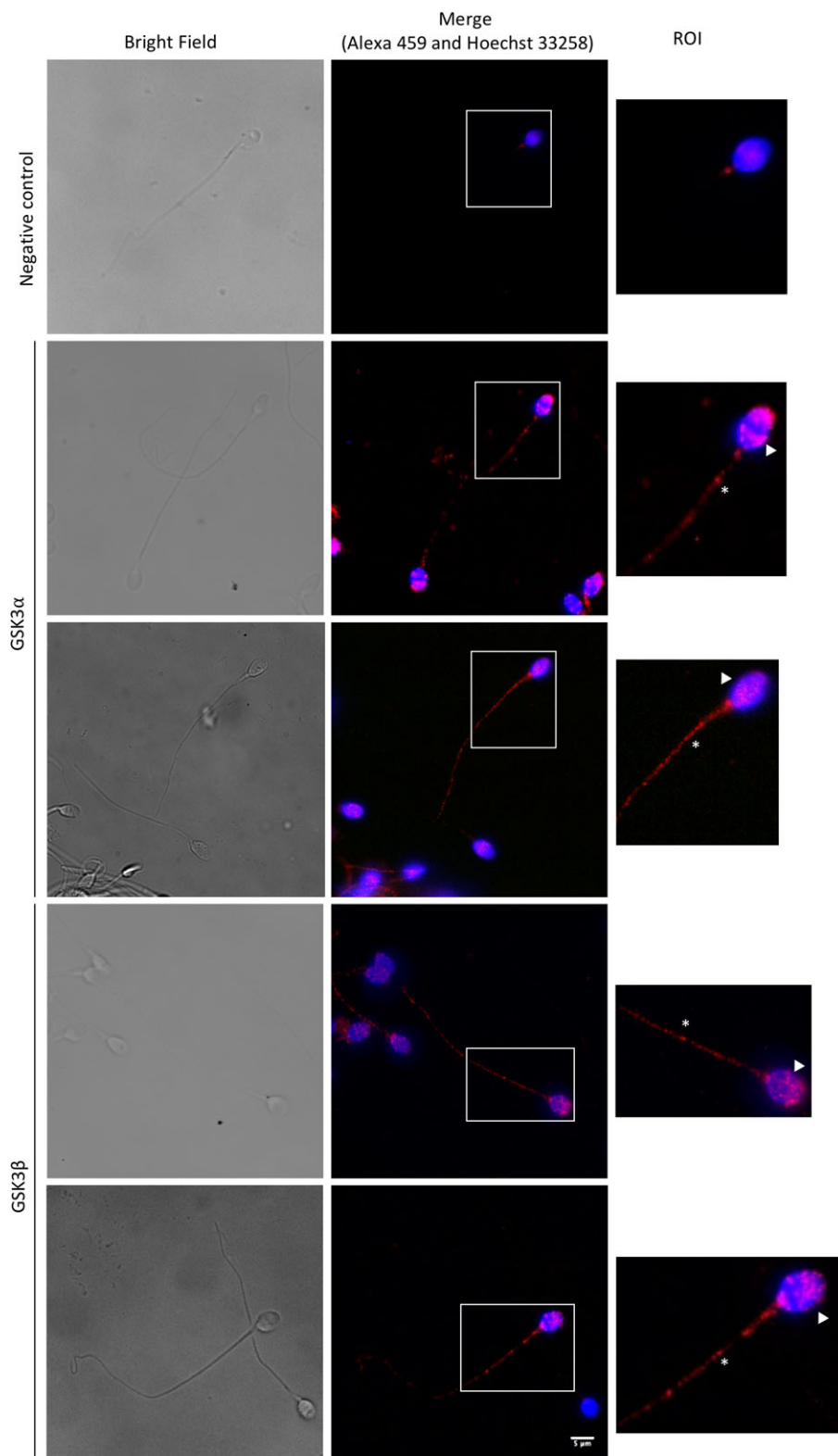
Figure 2 Subcelular localization of GSK3A and GSK3B in normospermic ejaculated human sperm. GSK3A is located in the flagellum (star) and head (arrowhead), more specifically in the equatorial region. GSK3B is located through the entire head (arrowhead) and occasionally in the flagellum (star). Per sample, 100 sperm cells were counted. The experiment was done in triplicate. Scale bar is 5 μm. Nucleus is marked in blue. ROI: region of interest. All images were obtained with 63× magnification.
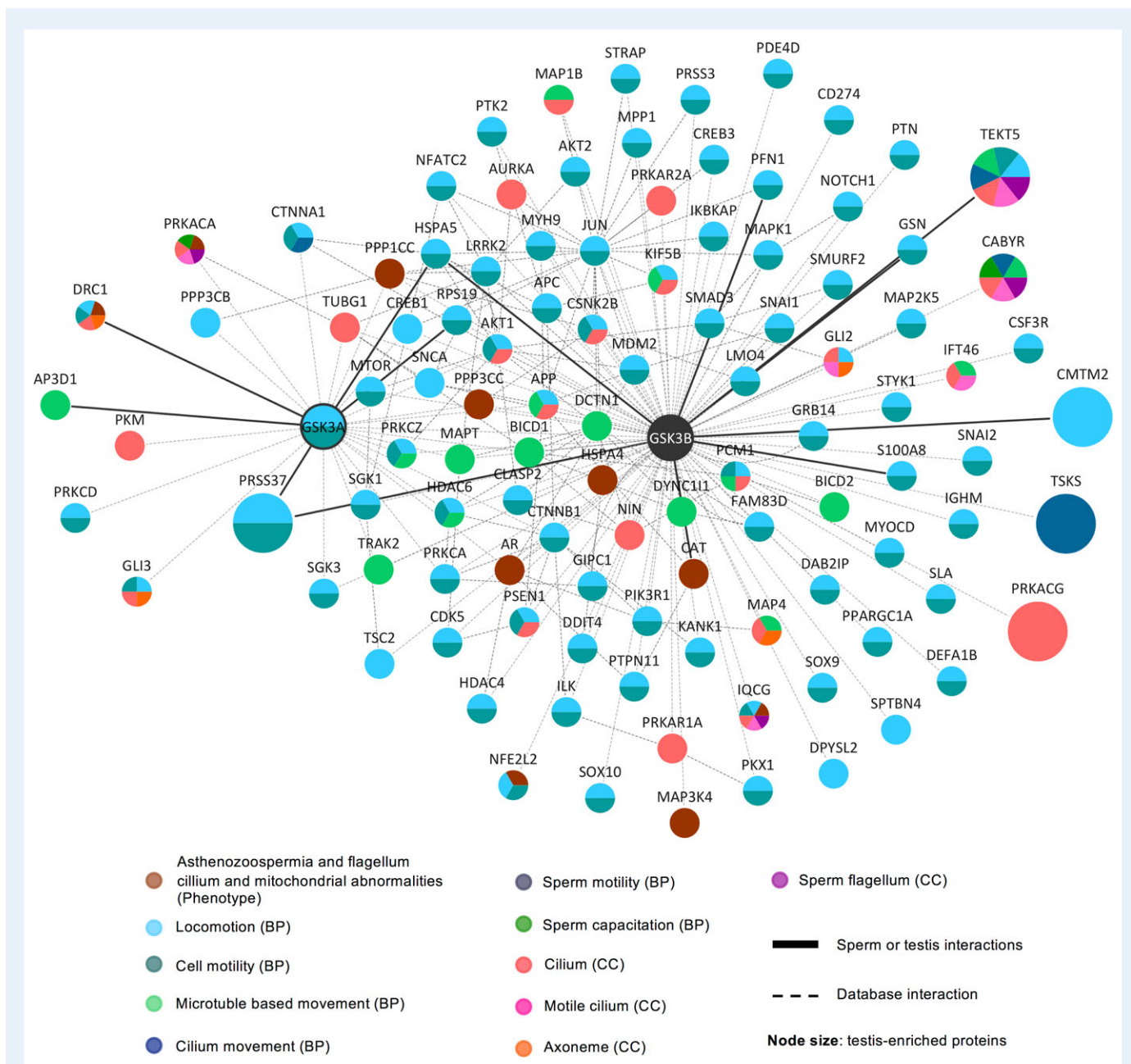
Figure 3 **GSK3-centered subnetwork for sperm motility extracted from GSK3 interactome network.** All GSK3 interactors associated with motility-related annotations were used to build the network. Solid lines: testis or sperm GSK3 interactions. Dashed lines: databased-retrieved GSK3 interactions. Node size: according to testis expression. Node colors: represent motility-related phenotypes, biological processes (BP) or cellular components (CC).

annotated to motility-related categories, and of those, six are highly expressed in testis (CABYR, TEKT5, PRKACG, PRSS37, TSKS and CMTM2) (Fig. 3).

Analyzing the GSK3 testis subnetwork (Fig. 4), 10 GSK3A interactors were associated with testis-related annotations and 2 of those were identified in this study (PRSS37 and HSP90AA1). Only PRSS37 was described as highly expressed in testis. With five testis-related annotations, we highlight AKAP9 and AR. For testis-related categories, GSK3B presents 45 interactors related to testis-related categories (Fig. 4).

Although not directly related to sperm motility and testis function, several GSK3 interactors are associated with more general annotations linked to the male reproductive system (Supplementary Fig. S5).

AKAP11 and LRP6 subcellular localization in human sperm

Two GSK3 interactors identified in this study, A-kinase anchor protein 11 (AKAP11) and low-density lipoprotein receptor-related protein 6 (LRP6), were chosen for further characterization, since they have been

Figure 4 GSK3-centered subnetwork for testis-related annotations extracted from GSK3 interactome network. All GSK3 interactors associated with testis annotations were used to build the network. Solid lines: testis or sperm GSK3 interactions; Dashed lines: databased-retrieved GSK3 interactions. Node size: according to testis expression. Node colors: represent testis related phenotypes, biological processes (BP) or cellular components (CC).
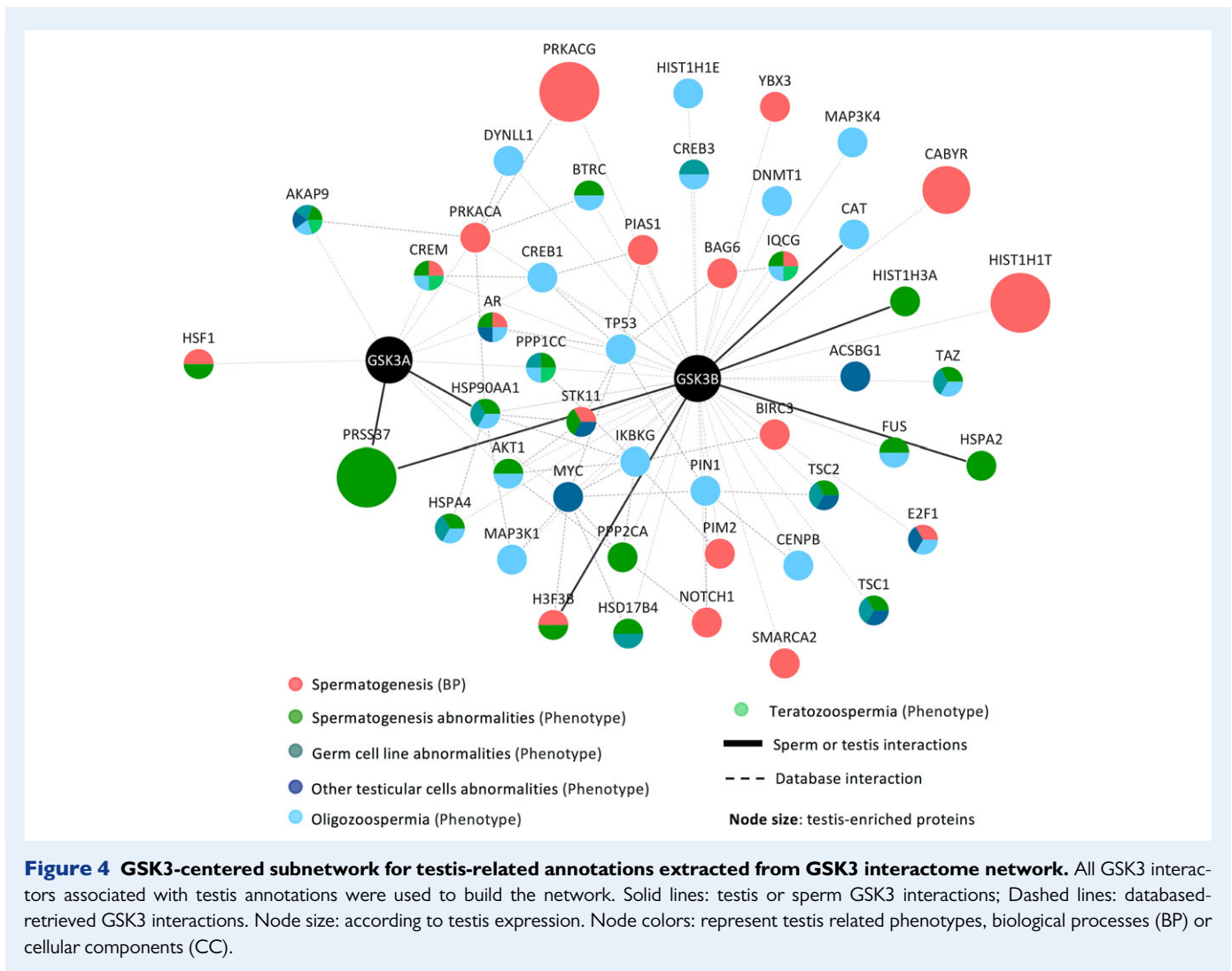
previously implicated in the regulation of male fertility. Figure 5A shows that LRP6 is present in human testis and sperm at 180 kDa, the expected molecular weight of the protein. The band at the higher molecular weight could be due to post-translational modification, such as phosphorylation and N-glycosylation, known to occur in LRP6 (Khan *et al.*, 2007; Niehrs and Shen, 2010). Immunocytochemistry studies (Fig. 5B), revealed that total LRP6 is localized to the entire length of the flagellum and occasionally at the post-acrosomal area. However, phosphorylated LRP6 (p1490LRP6) is restricted to the midpiece. Moreover, a closer analysis showed that not all sperm cells present immunoreactivity towards LRP6 and p1490LRP6. Only 18 and 29% of sperm cells present immunoreactivity for LRP6 and p1490LRP6, respectively (Fig. 5B). Regarding AKAP11, this protein is localized on the anterior portion of the head and the equatorial area of ejaculated human sperm (Fig. 5B).

Discussion

GSK3 has been long associated with sperm motility acquisition and maintenance in mammals (Smith *et al.*, 1999; Vijayaraghavan *et al.*, 2000; Somanath *et al.*, 2004). Recently, an isoform-specific function of

GSK3A in mice sperm primary motility acquisition has been suggested. However, the characterization of both GSK3 isoforms (GSK3A and GSK3B) in human sperm and testis physiology has been sparse. Assessment of a similar isoform-specific function of GSK3A in human sperm motility acquisition was thus necessary. This work aimed to characterize GSK3 isoforms in human sperm as well as identify and analyze the GSK3A and GSK3B interactome in human sperm and testis. Ultimately, this can help decipher the role of isoform-specific functions of GSK3 in human sperm physiology.

In this study we provided evidence to support that mature human sperm cells are unique in their need for GSK3A isoform to achieve progressive motility. Similar to other mammals, both GSK3 isoforms are present in human testis and sperm (Fig. 1). Characterization of GSK3 levels in normospermic and asthenozoospermic samples proved that in ejaculated human sperm, serine phosphorylated GSK3A presents a strong positive correlation with progressive sperm motility, but serine phosphorylation GSK3B does not show any correlation with sperm motility (Fig. 1). Furthermore, correlation between the percentage of immotile spermatozoa (Supplementary Table SII) and levels of serine phosphorylated GSK3A is in accordance with the correlation observed with progressive motile spermatozoa. This shows that
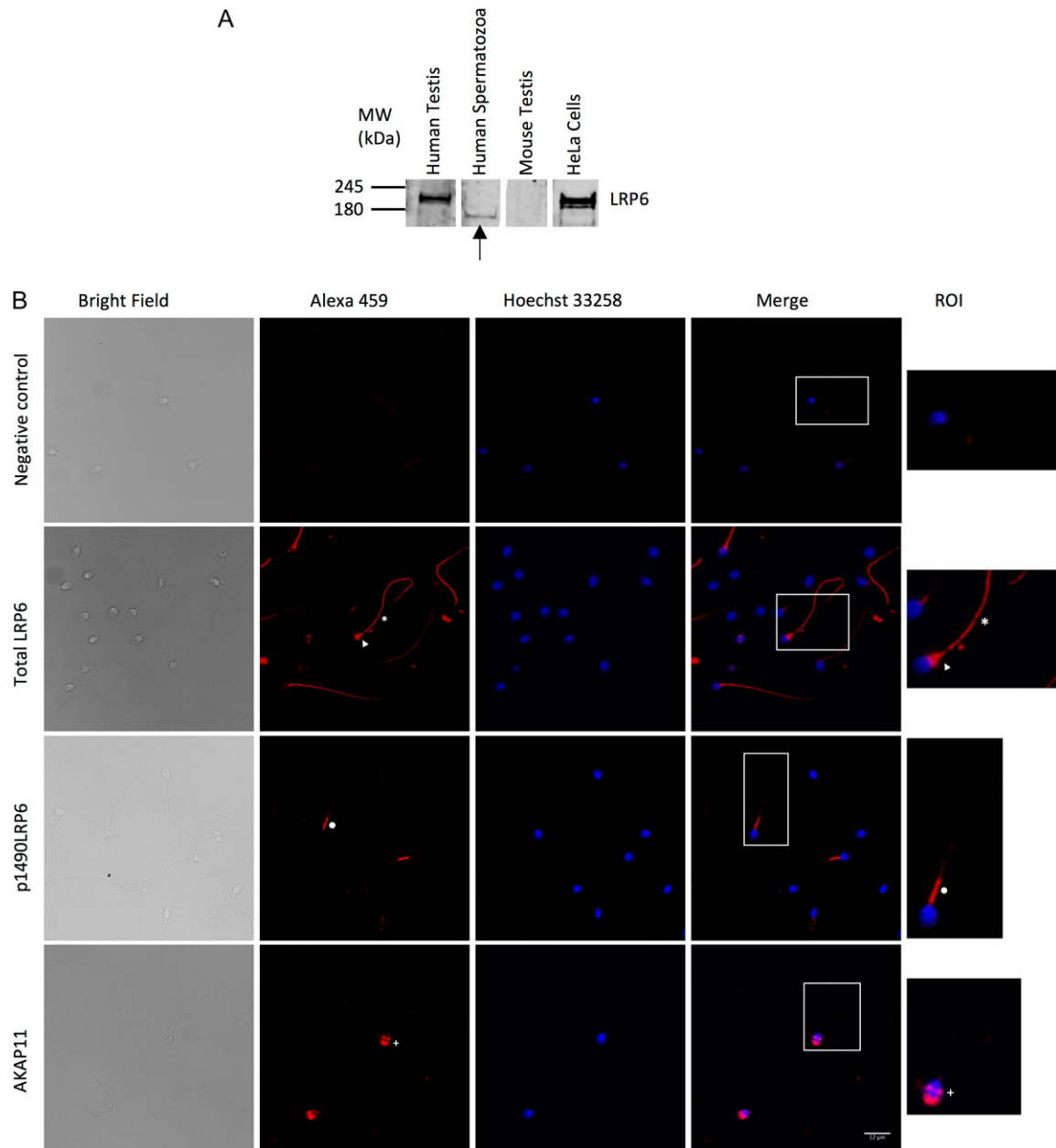
Figure 5 LRP6 and AKAP11 in human testis and ejaculated normospermic sperm. (**A**) Western blot analysis of LRP6 in human testis and ejaculated sperm, mouse testis and HeLa cells. For human testis, mouse testis and HeLa cells 30 µg of protein were loaded per sample. For ejaculated human sperm, 100 µg of proteins were loaded. Note according to the antibody datasheet, the antibody only recognizes human and rat LRP6. Arrow highlights the LRP6 presence in human sperm. (**B**) Subcellular localization of LRP6, p1490LRP6 and AKAP11 in mature human sperm. Total LRP6 is located in the entire flagellum (star) and occasionally in the post-acrosomal area (arrowhead). The phosphorylated form of LRP6 at serine 1490 is restricted to the midpiece (circle). AKAP11 is located to the head, specifically to the anterior and equatorial area (plus sign). Blots were cropped; 100 sperm cells were counted per samples. The experiment done in triplicate. Scale bar is 10 µm. Nucleus is marked in blue. ROI, region of interest. All images were obtained with 63× magnification.

GSK3A activity is strongly correlated with human sperm motility, being a negative modulator, while GSK3B appears does not influence sperm motility. This is the first observation that GSK3 activity is associated with human sperm motility and that this function is a GSK3A isoform-specific function. The power of the study was limited by the relatively small samples size (three normozoospermic samples and four asthenozoospermic samples). However, recent studies reinforce the results obtained. Using, knock-out technology a GSK3A isoform-specific function in mice sperm motility has been proved by Bhattacharjee and colleagues (Bhattacharjee et al., 2015, 2018).

A possible explanation for the inability of GSK3B to substitute for GSK3A in human sperm relies on a distinct spatial expression pattern

between GSK3 isoforms in human sperm cells. The immunocytochemistry studies performed, showed that GSK3A is consistently present in the tail, but in only 75% of the cases was it also present in the head. Opposing GSK3A, GSK3B is always present on the head of human sperm, while its localization on the tail is irregular. A more plausible explanation for isoform-specific function of GSK3 in human sperm is GSK3 isoform-specific interactors that bind, target and modulate each isoform in human sperm. Work by Zeidner *et al.*, showed that RACK1 is a GSK3A isoform-specific interactor in the central nervous system, and that this interaction requires the unique glycine-rich GSK3A N-termini (Zeidner *et al.*, 2011).

With the purpose of identifying GSK3 isoform-specific interactions in the male reproductive system, the GSK3A and GSK3B interactomes in human testis and sperm were identified and characterized (Supplementary Tables III, IV, VI and VII). Due to technical restrains (human testis availability and sperm physiology), the human testis GSK3 interactome was constructed using an yeast two-hybrid approach, while for the human sperm GSK3 interactome, coimmunoprecipitation followed by mass spectrometry was undertaken. The yeast-two hybrid system relies on the yeast cell environment, not fully mimicking mammalian cells. Yet, it is one of the only techniques that indicates binary interactions. Coimmunoprecipitation does not prove direct interaction, and weak interactions are usually lost but retains intracellular environment conditions. Approximately 27% of the GSK3 interactions identified in this study have been previously described, which results in high confidence in the GSK3 interactomes identified. Furthermore, the interaction between GSK3 and AXIN2 was acknowledged, for the first time, in testis. This interaction is extensively described in somatic cells (Stamos and Weis, 2013; Voronkov and Krauss, 2013; Song *et al.*, 2014; Pronobis *et al.*, 2015), reinforcing our confidence in the results obtained for the GSK3 interactome.

With the purpose of constructing the most complete GSK3 interactome, GSK3 interactions available on PPIs databases were retrieved and GSK3-centered networks were constructed (Figs 3 and 4, Supplementary Figs S4 and S5). To identify GSK3 interactions key for sperm physiology (more specifically sperm motility), tissue-expression, phenotypes and gene ontology annotations were integrated into the GSK3 networks. It may be noted that the knowledge of protein tissue expression is still limited and typically does not take into account tissue-specific alternatively spliced transcripts. This is particularly relevant for testis, since testis is a tissue with a higher number of alternative transcripts splice variants (Elliott and Grellscheid, 2006; Uhlén *et al.*, 2015). None of GSK3A interactors listed on databases showed a testis-specific or -enriched expression. We identified the first testis-enriched or -specific GSK3A interactors which reflects the importance for deepening the knowledge on sperm physiology of our results. Regarding GSK3A interactions, 20.1% have a motility-related annotation and for GSK3B, 21% of interactors have been previously link to cell motility. This is relevant considering the sperm cells are the only human cells that possesses a progressive motile function. The fact that almost a quarter of the GSK3 interactome may be involved in the motility cell function reflects that the molecular mechanisms that control sperm cell motility are still partially unknown. Focusing on GSK3A interactions that have previously been shown to be involved, we highlight PRSS37. This protein is the only GSK3A interactor that is known to be associated with sperm motility, testis annotations, and categorized as enriched in testis (Fig. 3). Previous studies demonstrated that

when PRSS37 is absent in mice testis, fertilization is compromised due to inadequate spermatogenesis, decreased sperm oviduct-migration and decreased sperm-zona binding (Shen *et al.*, 2013a). Concerning testis functions, our analysis revealed that AR, PPP1CC and AKAP9 appear to have a prominent role since germ cells and other types of testicular cells are greatly affected by their absence (Fig. 4). These findings are in accordance with former studies (Varmuza *et al.*, 1999; Wang *et al.*, 2009; Schimenti *et al.*, 2013).

LRP6 and AKAP11, two GSK3 interactors identified in this study, were chosen for further characterization, as being previously involved in male reproduction. LRP6 was already described as involved in sperm motility and testis physiology, and AKAP11 in mouse spermatogenesis (Reinton *et al.*, 2000; Koch *et al.*, 2015). While the interaction between AKAP11 and GSK3B has been previously described (Tanji *et al.*, 2002), to our knowledge this is the first description of the interaction with GSK3A and the first time the interaction is described in human testis. In contrast with earlier studies in human sperm (Reinton *et al.*, 2000), we showed that AKAP11 is localized in the anterior portion of the head and equatorial region (Fig. 5B). In somatic cells, AKAP11 has been associated with cell migration (Logue *et al.*, 2011) and in 2002, Tanji *et al.* showed that AKAP11, PPP1, PRKACA and GSK3B formed a multimeric complex in which PPP1 and PRKACA controlled GSK3B activity. Since both PPP1 and PRKACA have been extensively described in mammalian testis and sperm (Smith *et al.*, 1996; Davidson *et al.*, 2005; Schimenti *et al.*, 2013), we may assume that similar multimeric complex may be formed to control GSK3 activity.

Bioinformatics analysis revealed that in mice, absence of LRP6 correlates with male infertility (Supplementary Fig. S5 and Supplementary Table SXI). Expression studies showed that LRP6 is present in human testis and sperm and is localized along the entire flagellum (Fig. 5A and B). Furthermore, when LRP6 is phosphorylated on S1490 (in somatic cells a GSK3 substrate (Davidson *et al.*, 2005; Zeng *et al.*, 2005)), its subcellular location is restricted to the human sperm midpiece (Fig. 5B). This is in accordance to earlier studies in mice and bovine sperm (Koch *et al.*, 2015). Interestingly, only a small percentage of the sperm cells within the same sample present staining for both LRP6 and S140 phosphorylated LRP6. Further studies to understand why this expression pattern occurs may prove useful. Koch *et al.* (2015) explored the non-genetic effects of B-catenin signaling on human sperm and suggested that the interaction between LRP6 and GSK3 is required for protein stabilization and consequently sperm motility. Therefore, despite the fact that in somatic cells GSK3/LRP6 interaction is involved in gene expression, our results reinforce that in human sperm this interaction can be fundamental for sperm physiology.

In conclusion, our data revealed an isoform-specific need for GSK3A in human progressive sperm motility modulation. The GSK3 interactome identified in this work uncovers the extent to which GSK3 can be involved in sperm motility and reveals new potential players in the molecular mechanisms of sperm motility. Even more, study of GSK3A interactors such as PRSS37 deserve to be pursued since the likelihood of this protein being involved in sperm motility is high. Furthermore, although we attempted to identify specific GSK3A interactors, no interaction was validated as GSK3A-unique. Selective GSK3A inhibitors and identification of specific targets of GSK3A can facilitate the development of a new group of male contraceptives based on sperm motility arrest.

Supplementary data

Acknowledgements

Authors' roles

M.J.F. designed the study, performed experiments, acquired, analyzed and interpreted the data and produced the article. J.V.S. performed experiments, interpreted the data and drafted the article. C.B. performed experiments and analyzed the data. B.R.C. analyzed and interpreted the data (statistical analysis). M.F. and S.V. designed the study and analyzed and interpreted the data. All authors critically revised the article and approved the final version.

Funding

Conflict of interest

The authors declare that there are no conflicts of interest.

References

Alanis-Lobato G, Andrade-Navarro MA, Schaefer MH. HIPPIE v2.0: enhancing meaningfulness and reliability of protein-protein interaction networks. *Nucleic Acids Res* 2017;**45**:D408–D414.

Amar S, Belmaker RH, Agam G. The possible involvement of glycogen synthase kinase-3 (GSK-3) in diabetes, cancer and central nervous system diseases. *Curr Pharm Des* 2011;**17**:2264–2277.

Amaral A, Paiva C, Attardo Parrinello C, Estanyol JM, Ballescà JL, Ramalho-Santos J, Oliva R. Identification of proteins involved in human sperm motility using high-throughput differential proteomics. *J Proteome Res* 2014;**13**:5670–5684.

Amberger JS, Bocchini CA, Schiettecatte F, Scott AF, Hamosh A. OMIM. org: online Mendelian inheritance in man (OMIM®), an online catalog of human genes and genetic disorders. *Nucleic Acids Res* 2015;**43**:D789–D798.

An C-N, Jiang H, Wang Q, Yuan R-P, Liu J-M, Shi W-L, Zhang Z-Y, Pu X-P. Down-regulation of DJ-1 protein in the ejaculated spermatozoa from Chinese asthenozoospermia patients. *Fertil Steril* 2011;**96**:19–23.e2.

Azoulay-Alfaguter I, Yaffe Y, Licht-Murava A, Urbanska M, Jaworski J, Pietrokovski S, Hirschberg K, Eldar-Finkelman H. Distinct molecular regulation of glycogen synthase kinase-3alpha isozyme controlled by its N-terminal region: functional role in calcium/calpain signaling. *J Biol Chem* 2011;**286**:13470–13480.

Beurel E, Grieco SF, Jope RS. Glycogen synthase kinase-3 (GSK3): regulation, actions, and diseases. *Pharmacol Ther* 2015;**148**:114–131.

Bhagwat S, Dalvi V, Chandrasekhar D, Matthew T, Acharya K, Gajbhiye R, Kulkarni V, Sonawane S, Ghosalkar M, Parte P. Acetylated α-tubulin is reduced in individuals with poor sperm motility. *Fertil Steril* 2014;**101**:95–104.e3.

Bhattacharjee R, Goswami S, Dey S, Gangoda M, Brothag C, Eisa A, Woodgett J, Phiel C, Kline D, Vijayaraghavan S. Isoform specific requirement for GSK3α in sperm for male fertility. *Biol Reprod* 2018;**99**:384–394. Available from: http://www.ncbi.nlm.nih.gov/pubmed/29385396.

Bhattacharjee R, Goswami S, Dudiki T, Popkie AP, Phiel CJ, Kline D, Vijayaraghavan S. Targeted disruption of glycogen synthase kinase 3A (GSK3A) in mice affects sperm motility resulting in male infertility. *Biol Reprod* 2015;**92**:65.

Blom N, Sicheritz-Pontén T, Gupta R, Gammeltoft S, Brunak S. Prediction of post-translational glycosylation and phosphorylation of proteins from the amino acid sequence. *Proteomics* 2004;**4**:1633–1649.

Cai Z-M, Gui Y-T, Guo X, Yu J, Guo L-D, Zhang L-B, Wang H, Yu J. Low expression of glycoprotein subunit 130 in ejaculated spermatozoa from asthenozoospermic men. *J Androl* 2006;**27**:645–652.

de Castro E, Sigrist CJA, Gattiker A, Bulliard V, Langendijk-Genevaux PS, Gasteiger E, Bairoch A, Hulo N. ScanProsite: detection of PROSITE signature matches and ProRule-associated functional and structural residues in proteins. *Nucleic Acids Res* 2006;**34**:W362–W365.

Chen J, Wang Y, Xu X, Yu Z, Gui Y, Cai Z. [Differential expression of ODF1 in human ejaculated spermatozoa and its clinical significance]. *Zhonghua Nan Ke Xue* 2009;**15**:891–894.

Cox J, Hein MY, Luber CA, Paron I, Nagaraj N, Mann M. Accurate proteome-wide label-free quantification by delayed normalization and maximal peptide ratio extraction, termed MaxLFQ. *Mol Cell Proteomics* 2014;**13**:2513–2526.

Cox J, Mann M. MaxQuant enables high peptide identification rates, individualized p.p.b.-range mass accuracies and proteome-wide protein quantification. *Nat Biotechnol* 2008;**26**:1367–1372.

Davidson G, Wu W, Shen J, Bilic J, Fenger U, Stannek P, Glinka A, Niehrs C. Casein kinase 1 gamma couples Wnt receptor activation to cytoplasmic signal transduction. *Nature* 2005;**438**:867–872.

Dinkel H, Roey K Van, Michael S, Kumar M, Uyar B, Altenberg B, Milchevskaya V, Schneider M, Kühn H, Behrendt A *et al.* ELM 2016–data update and new functionality of the eukaryotic linear motif resource. *Nucleic Acids Res* 2016;**44**:D294–D300.

Elliott DJ, Grellscheid SN. Alternative RNA splicing regulation in the testis. *Reproduction* 2006;**132**:811–819.

Eppig JT, Richardson JE, Kadin JA, Ringwald M, Blake JA, Bult CJ. Mouse Genome Informatics (MGI): reflecting on 25 years. *Mamm Genome* 2015;**26**:272–284.

Gao C, Hölscher C, Liu Y, Li L. GSK3: a key target for the development of novel treatments for type 2 diabetes mellitus and Alzheimer disease. *Rev Neurosci* 2011;**23**:1–11.

Gene Ontology Consortium. Gene Ontology Consortium: going forward. *Nucleic Acids Res* 2015;**43**:D1049–D1056.

Guo TB, Chan KC, Hakovirta H, Xiao Y, Toppari J, Mitchell AP, Salameh WA. Evidence for a role of glycogen synthase kinase-3 beta in rodent spermatogenesis. *J Androl* 2003;**24**:332–342.

Hashemitabar M, Sabbagh S, Orazizadeh M, Ghadiri A, Bahmanzadeh M. A proteomic analysis on human sperm tail: comparison between normozoospermia and asthenozoospermia. *J Assist Reprod Genet* 2015;**32**:853–863.

Hornbeck PV, Zhang B, Murray B, Kornhauser JM, Latham V. Skrzypek E. PhosphoSitePlus, 2014: mutations, PTMs and recalibrations. *Nucleic Acids Res* 2015;**43**:D512–D520.

Jing X, Xing R, Zhou Q, Yu Q, Guo W, Chen S, Chu Q, Feng C, Mao X. [Expressions of cysteine-rich secretory protein 2 in asthenospermia]. *Zhonghua Nan Ke Xue* 2011;**17**:203–207.

Kaidanovich-Beilin O, Woodgett JR. GSK-3: functional insights from cell biology and animal models. *Front Mol Neurosci* 2011;**4**:40.

Khan Z, Vijayakumar S, la Torre TV, de, Rotolo S, Bafico A. Analysis of endogenous LRP6 function reveals a novel feedback mechanism by which Wnt negatively regulates its receptor. *Mol Cell Biol* 2007;**27**:7291–7301.

Koch S, Acebron SP, Herbst J, Hatiboglu G, Niehrs C. Post-transcriptional Wnt signaling governs epididymal sperm maturation. *Cell* 2015;**163**: 1225–1236.

Li Y-S, Feng X-X, Ji X-F, Wang Q-X, Gao X-M, Yang X-F, Pan Z-H, Sun L, Ma K. [Expression of SEPT4 protein in the ejaculated sperm of idiopathic asthenozoospermic men]. *Zhonghua Nan Ke Xue* 2011;**17**:699–702.

Li H, Yu N, Zhang X, Jin W, Li H. Spermatozoal protein profiles in male infertility with asthenozoospermia. *Chin Med J (Engl)* 2010;**123**:2879–2882.

Logue JS, Whiting JL, Tunquist B, Sacks DB, Langeberg LK, Wordeman L, Scott JD. AKAP220 protein organizes signaling elements that impact cell migration. *J Biol Chem* 2011;**286**:39269–39281.

Niehrs C, Shen J. Regulation of Lrp6 phosphorylation. *Cell Mol Life Sci* 2010;**67**:2551–2562.

Orchard S, Kerrien S, Abbani S, Aranda B, Bhate J, Bidwell S, Bridge A, Briganti L, Brinkman FSL, Brinkman F et al. Protein interaction data curation: the International Molecular Exchange (IMEx) consortium. *Nat Methods* 2012;**9**:345–350.

Pan J-B, Hu S-C, Shi D, Cai M-C, Li Y-B, Zou Q, Ji Z-L. PaGenBase: a pattern gene database for the global and dynamic understanding of gene function. *PLoS One* 2013;**8**:e80747.

Petryszak R, Burdett T, Fiorelli B, Fonseca NA, Gonzalez-Porta M, Hastings E, Huber W, Jupp S, Keays M, Kryvych N et al. Expression Atlas update—a database of gene and transcript expression from microarray- and sequencing-based functional genomics experiments. *Nucleic Acids Res* 2014;**42**:D926–D932.

Piñero J, Bravo À, Queralt-Rosinach N, Gutiérrez-Sacristán A, Deu-Pons J, Centeno E, García-García J, Sanz F, Furlong LI. DisGeNET: a comprehensive platform integrating information on human disease-associated genes and variants. *Nucleic Acids Res* 2017;**45**:D833–D839.

Pontius JU, Wagner L, Schuler GD. UniGene: a unified view of the transcriptome. *NCBI Handb* 2003;**1**:1–12.

Pronobis MI, Rusan NM, Peifer M. A novel GSK3-regulated APC:Axin interaction regulates Wnt signaling by driving a catalytic cycle of efficient βcatenin destruction. *Elife* 2015;**4**:e08022.

Reinton N, Collas P, Haugen TB, Skålhegg BS, Hansson V, Jahnsen T, Taskén K. Localization of a novel human A-kinase-anchoring protein, hAKAP220, during spermatogenesis. *Dev Biol* 2000;**223**:194–204.

Salvolini E, Buldreghini E, Lucarini G, Vignini A, Giulietti A, Lenzi A, Mazzanti L. Primio R Di, Balercia G. Interleukin-1β, cyclooxygenase-2, and hypoxia-inducible factor-1α in asthenospermia. *Histochem Cell Biol* 2014;**142**:569–575.

Saraswat M, Joenväärä S, Jain T, Tomar AK, Sinha A, Singh S, Yadav S, Renkonen R. Human spermatozoa quantitative proteomic signature classifies normo- and asthenozoospermia. *Mol Cell Proteomics* 2017;**16**: 57–72.

Schimenti KJ, Feuer SK, Griffin LB, Graham NR, Bovet CA, Hartford S, Pendola J, Lessard C, Schimenti JC, Ward JO. AKAP9 is essential for spermatogenesis and sertoli cell maturation in mice. *Genetics* 2013;**194**: 447–457.

Shannon P, Markiel A, Ozier O, Baliga NS, Wang JT, Ramage D, Amin N, Schwikowski B, Ideker T. Cytoscape: a software environment for integrated models of biomolecular interaction networks. *Genome Res* 2003;**13**:2498–2504.

Shen C, Kuang Y, Liu J, Feng J, Chen X, Wu W, Chi J, Tang L, Wang Y, Fei J et al. Prss37 is required for male fertility in the mouse. *Biol Reprod* 2013a;**88**:123.

Shen S, Wang J, Liang J, He D. Comparative proteomic study between human normal motility sperm and idiopathic asthenozoospermia. *World J Urol* 2013b;**31**:1395–1401.

Silva JV, Yoon S, De Bock P-J, Goltsev AV, Gevaert K, Mendes JFF, Fardilha M. Construction and analysis of a human testis/sperm-enriched interaction network: unraveling the PPP1CC2 interactome. *Biochim Biophys Acta* 2017;**1861**:375–385.

Smith GD, Wolf DP, Trautman KC. Cruz e Silva EF da, Greengard P, Vijayaraghavan S. Primate sperm contain protein phosphatase 1, a biochemical mediator of motility. *Biol Reprod* 1996;**54**:719–727.

Smith GD, Wolf DP, Trautman KC, Vijayaraghavan S. Motility potential of macaque epididymal sperm: the role of protein phosphatase and glycogen synthase kinase-3 activities. *J Androl* 1999;**20**:47–53.

Somanath PR, Jack SL, Vijayaraghavan S. Changes in sperm glycogen synthase kinase-3 serine phosphorylation and activity accompany motility initiation and stimulation. *J Androl* 2004;**25**:605–617.

Song X, Wang S, Li L. New insights into the regulation of Axin function in canonical Wnt signaling pathway. *Protein Cell* 2014;**5**:186–193.

Stamos JL, Weis WI. The β-catenin destruction complex. *Cold Spring Harb Perspect Biol* 2013;**5**:a007898.

Tanji C, Yamamoto H, Yorioka N, Kohno N, Kikuchi K, Kikuchi A. A-kinase anchoring protein AKAP220 binds to glycogen synthase kinase-3beta (GSK-3beta) and mediates protein kinase A-dependent inhibition of GSK-3beta. *J Biol Chem* 2002;**277**:36955–36961.

Tyanova S, Temu T, Sinitcyn P, Carlson A, Hein MY, Geiger T, Mann M, Cox J. The Perseus computational platform for comprehensive analysis of (prote)omics data. *Nat Methods* 2016;**13**:731–740.

Uhlén M, Fagerberg L, Hallström BM, Lindskog C, Oksvold P, Mardinoglu A, Sivertsson Å, Kampf C, Sjöstedt E, Asplund A et al. Proteomics. Tissue-based map of the human proteome. *Science* 2015;**347**:1260419.

Varmuza S, Jurisicova A, Okano K, Hudson J, Boekelheide K, Shipp EB. Spermiogenesis is impaired in mice bearing a targeted mutation in the protein phosphatase 1cgamma gene. *Dev Biol* 1999;**205**:98–110.

Vijayaraghavan S, Mohan J, Gray H, Khatra B, Carr DW. A role for phosphorylation of glycogen synthase kinase-3alpha in bovine sperm motility regulation. *Biol Reprod* 2000;**62**:1647–1654.

Vijayaraghavan S, Stephens DT, Trautman K, Smith GD, Khatra B. Cruz e Silva EF da, Greengard P. Sperm motility development in the epididymis is associated with decreased glycogen synthase kinase-3 and protein phosphatase 1 activity. *Biol Reprod* 1996;**54**:709–718.

Voronkov A, Krauss S. Wnt/beta-catenin signaling and small molecule inhibitors. *Curr Pharm Des* 2013;**19**:634–664.

Wang QM, Fiol CJ, DePaoli-Roach AA, Roach PJ. Glycogen synthase kinase-3 beta is a dual specificity kinase differentially regulated by tyrosine and serine/threonine phosphorylation. *J Biol Chem* 1994;**269**: 14566–14574.

Wang R-S, Yeh S, Tzeng C-R, Chang C. Androgen receptor roles in spermatogenesis and fertility: lessons from testicular cell-specific androgen receptor knockout mice. *Endocr Rev* 2009;**30**:119–132.

World Health Organization. *WHO Laboratory Manual for the Examination and Processing of Human Semen*, 5th edn. Geneva: WHO, 2010.

Wu G, Huang H, Garcia Abreu J, He X. Inhibition of GSK3 phosphorylation of beta-catenin via phosphorylated PPPSPXS motifs of Wnt coreceptor LRP6. *PLoS One* 2009;**4**:e4926.

Wu C, Jin X, Tsueng G, Afrasiabi C, Su AI. BioGPS: building your own mash-up of gene annotations and expression profiles. *Nucleic Acids Res* 2016;**44**:D313–D316.

Xue Y, Liu Z, Cao J, Ma Q, Gao X, Wang Q, Jin C, Zhou Y, Wen L, Ren J. GPS 2.1: enhanced prediction of kinase-specific phosphorylation sites with an algorithm of motif length selection. *Protein Eng Des Sel* 2011;**24**: 255–260.

Yu W, Clyne M, Khoury MJ. Gwinn M. Phenopedia and Genopedia: disease-centered and gene-centered views of the evolving knowledge of human genetic associations. *Bioinformatics* 2010;**26**:145–146.

Zeidner LC, Buescher JL, Phiel CJ. A novel interaction between Glycogen Synthase Kinase-3α (GSK-3α) and the scaffold protein Receptor for Activated C-Kinase 1 (RACK1) regulates the circadian clock. *Int J Biochem Mol Biol* 2011;**2**:318–327.

Zeng X, Tamai K, Doble B, Li S, Huang H, Habas R, Okamura H, Woodgett J, He X. A dual-kinase mechanism for Wnt co-receptor phosphorylation and activation. *Nature* 2005;**438**:873–877.

Zhou J-H, Zhou Q-Z, Lyu X-M, Zhu T, Chen Z-J, Chen M-K, Xia H, Wang C-Y, Qi T, Li X *et al*. The expression of cysteine-rich secretory protein 2 (CRISP2) and its specific regulator miR-27b in the spermatozoa of patients with asthenozoospermia. *Biol Reprod* 2015;**92**:28.

ORIGINAL ARTICLE

Adipose tissue-derived stem cells boost vascularization in grafted ovarian tissue by growth factor secretion and differentiation into endothelial cell lineages

D.D. Manavella[1], L. Cacciottola[1], V.L. Payen[2], C.A. Amorim [ID] [1], J. Donnez[3], and M.M. Dolmans [ID] [1,4,*]

[1]Pôle de Recherche en Gynécologie, Institut de Recherche Expérimentale et Clinique, Université Catholique de Louvain, Av. E. Mounier 52, 1200 Brussels, Belgium [2]Pôle de Recherche en Pédiatrie, Institut de Recherche Expérimentale et Clinique, Université Catholique de Louvain, Av. E. Mounier 52, 1200 Brussels, Belgium [3]Society for Research into Infertility, Av. Grandchamp 143, 1150 Brussels, Belgium [4]Service de Gynécologie, Cliniques Universitaires Saint-Luc, Av. Hippocrate 10, 1200 Brussels, Belgium

*Correspondence address. Pôle de Recherche en Gynécologie, Institut de Recherche Expérimentale et Clinique, Université Catholique de Louvain, Avenue Mounier 52, bte B1.52.02, 1200 Brussels, Belgium. Tel: +32-2-764-5237; Fax: +32-2-764-9507; E-mail: marie-madeleine. dolmans@uclouvain.be [ID] orcid.org/0000-0002-6331-3026

Adipose tissue-derived stem cells (ASCs) have multilineage differentiation potential, proangiogenic properties, and the ability to enhance vascularization in xenografted human ovarian tissue. The aim of the present study was to identify the mechanisms behind the proangiogenic effects of ASCs. For this purpose, severe combined immunodeficient (SCID) mice were grafted with frozen–thawed human ovarian tissue. ASCs were labeled by lentiviral transfection for expression of enhanced green fluorescent protein (eGFP), and human ovarian tissue was grafted using a previously described two-step procedure. In the control group, ovarian tissue was transplanted using the standard one-step approach. Samples were collected and analyzed after 7 days. Detection of the eGFP antigen by immunofluorescence showed ASCs surrounding and infiltrating ovarian tissue grafts. Significantly higher vessel density was observed in the ASC group ($P = 0.0182$ versus control) on Day 7. Co-expression of eGFP, CD34 and CD31 was demonstrated in human vessels, confirming ASC differentiation into human endothelial cell lineages. Increased gene expression of vascular endothelial growth factor (VEGF) was also shown in the ASC group ($P = 0.0182$ versus control). Immunohistochemistry targeting anti-human VEGF revealed significantly higher expression levels in the ASC group ($P = 0.033$ versus control), while VEGF and eGFP immunofluorescence showed greater growth factor expression in areas surrounding ASCs. In conclusion, ASCs differentiate into human vessels and promote secretion of VEGF when transplanted together with human ovarian tissue to SCID mouse peritoneum using a two-step ovarian tissue grafting procedure. This is a promising step towards potentially improving ovarian tissue quality and lifespan. Long-term studies should be conducted to investigate ASC safety and efficacy in the context of ovarian tissue transplantation.

Key words: ovarian tissue transplantation / adipose tissue-derived stem cells / differentiation / vascular endothelial growth factor / fibroblast growth factor / endothelial cells

Introduction

Ovarian tissue cryopreservation and transplantation has gained ground as a valid fertility preservation and restoration approach owing to its established effectiveness. More than 130 live births have been achieved so far, showing a logarithmic increase over the past decade (Donnez and Dolmans, 2017).

Of all available fertility preservation strategies, including oocyte and embryo cryopreservation among others, ovarian tissue cryopreservation remains the only option for prepubertal girls and young women in whom cancer treatment cannot be delayed (Donnez and Dolmans, 2013; Donnez et al., 2015). Yet, however, successful this fertility preservation and restoration treatment may be, there are still issues that arise from the avascular nature of the grafting procedure itself, as up to

70–80% of follicles may be lost (Baird *et al.*, 1999; Nisolle *et al.*, 2000) during the first days post-grafting due to hypoxia (Van Eyck *et al.*, 2009). For this reason, shortening the early post-grafting hypoxic/ ischemic period is the focus of current research as a means of improving follicle survival in human ovarian tissue transplants (Manavella *et al.*, 2018b).

A recently described ovarian tissue transplantation technique using adipose tissue-derived stem cells (ASCs) delivered inside a fibrin scaffold 2 weeks prior to grafting was shown to enhance follicle survival, decrease apoptosis, and boost angiogenesis and oxygenation in grafted ovarian tissue (Manavella *et al.*, 2018a,b) compared to both the sham group (empty fibrin) and one-step ovarian tissue transplantation. In the two-step transplantation model, ASCs proved their ability to proliferate and induce formation of capillary-like structures in a peritoneal grafting site (Manavella *et al.*, 2018a). Furthermore, by preparing the transplantation site using ASCs, their proangiogenic role was also demonstrated, as a more extensive vasculature issuing from both host and graft was found in grafted ovarian tissue 7 days after transplantation (Manavella *et al.*, 2018b).

The aim of the present study was to investigate the mechanisms underlying the proangiogenic behavior of ASCs in the context of two-step ovarian tissue transplantation.

Materials and Methods

Experimental design

Ten severe combined immunodeficient (SCID) mice were grafted intraperitoneally with frozen–thawed human ovarian tissue from five different patients. Five mice were subjected to a two-step transplantation approach, whereby ovarian tissue was grafted to a peritoneal site that had been previously prepared with an ASC-loaded fibrin implant (ASC group) for 14 days prior to grafting, as reported in a previous study (Manavella *et al.*, 2018a). The remaining five mice underwent the standard one-step transplantation procedure (no site preparation, no stem cell addition, just thawed ovarian tissue) and served as controls (OT group) (Fig. 1). One piece of ovarian tissue per patient was fixed for analysis to serve as non-grafted controls. Samples were collected after euthanizing the mice on Day 7.

ASCs

Human ASCs from female donors were commercially acquired (Stempro® Human ASCs, Invitrogen, Carlsbad, USA). These cells have been shown to express a flow cytometry cell-surface protein profile positive for CD29, CD44, CD73, CD90, CD105 and CD166 (>95%), but negative for CD34, CD14, CD31, CD45 and Lin1 (<2%), which meets the specific surface antigen criteria to characterize mesenchymal stem cells (MSCs) (Dominici *et al.*, 2006). ASCs were cultured and expanded as previously described (Manavella *et al.*, 2018a). All cells used in this study were at passage 5. The viability of cultured ASCs was assessed using trypan blue solution (Sigma, Irvine, UK).

ASC transfection with enhanced green fluorescent protein

HEK293FT cells (Invitrogen) maintained in culture according to the provider's instructions were transfected with pRRLSIN.cPPT.PGK-GFP.WPRE (Addgene, Watertown, USA) and pCMV-VSV-G, pMDLg/pRRE and pRSV-Rev third-generation packaging systems (Addgene, Watertown, NY, USA) using Lipofectamine LTX and Plus Reagent (Invitrogen, Ghent,

Belgium) in Opti-MEM reduced serum medium, in line with the manufacturer's recommendations. Six hours after transfection, the Opti-MEM was replaced with culture medium supplemented with 10% undecomplemented fetal bovine serum. Twenty-four and 48 h after transfection, lentivirus-containing supernatant was harvested, titrated and used to infect target cells. Fluorescent cells were selected by fluorescence-activated cell sorting (FACS) using an Aria III cell sorter (BD Biosciences,San Jose, CA, USA). Data were processed by BD FACSDiva 8.0.1 software (BD Biosciences, San Jose, CA, USA) in order to obtain a 100% enhanced green fluorescent protein (eGFP)-positive ASC population (Fig. 2A) for subsequent expansion and transplantation.

Ethical approval

Animal welfare guidelines were strictly followed and the protocol was approved by the Committee on Animal Research of the Université Catholique de Louvain.

Ovarian tissue transplantation

Human ovarian tissue thawing procedure

The Institutional Review Board of the Université Catholique de Louvain approved use of human ovarian tissue for this study. Frozen ovarian tissue samples from five patients (aged 25–35 years) who underwent surgery for non-ovarian pathologies were taken from the ovarian tissue bank, after obtaining written informed consent.

Frozen ovarian tissue was thawed at room temperature for 2 min, immersed in a water bath at 37°C for another 2 min, and then washed three times with fresh HEPES-MEM medium (Gibco, Paisley, UK) to remove the cryoprotectant (Amorim *et al.*, 2012).

Ovarian tissue transplantation

Three ovarian tissue fragments of approximately $5 \times 4 \times 1\,mm^3$ were taken from each patient, thawed and distributed equally between three groups as follows: the fragment was cut into two, with one piece immediately fixed in 4% formaldehyde and the other placed in RNAlater (Invitrogen, Ghent, Belgium) and stored at −20°C for PCR analysis (non-grafted control group); the entire fragment was used for the two-step transplantation procedure (ASC group); and the remaining fragment was grafted following the standard one-step protocol (OT group).

In mice undergoing the two-step procedure, a previously described protocol was implemented (Manavella *et al.*, 2018a). Briefly, an incision was made 14 days after preparing the site with ASC-loaded fibrin implants, which were gently detached using blunt-tip forceps. Ovarian tissue fragments were then placed below the remaining fibrin layer (between the peritoneum and detached fibrin). In the OT group, ovarian fragments were fixed with stitches to the lower third of the parietal peritoneum after scratching the inner peritoneal surface with a scalpel (Luyckx *et al.*, 2014).

Sample collection and processing

Analyses were performed on frozen–thawed non-grafted samples and 7-day grafted tissues. Each and every grafted ovarian tissue sample was cut into two pieces; one piece was fixed in 4% formaldehyde, embedded in paraffin and serially sectioned (5-μm-thick sections), while the other piece was stored in RNAlater at −20°C for PCR analysis. Every fifth slide was stained with hematoxylin and eosin (HE) (Merck, Darmstadt, Germany) and all the rest were used for immunolabeling. All sections were digitized after immunofluorescence by automated whole-slide image capture using the Pannoramic P250 Flash III scanner (3DHISTECH, Budapest, Hungary) and slides obtained after immunohistochemistry were scanned using the Leica SCN400 scanner (Leica Biosystems, Ireland). Three sections per

Figure 1 **Design of experiment to determine how adipose tissue-derived stem cells boost vascularization in grafted human ovarian tissue.** Ten severe combined immunodeficient (SCID) mice were intraperitoneally grafted with frozen–thawed human ovarian tissue from five different patients. Five mice underwent two-step transplantation, whereby ovarian tissue (OT) was grafted to a peritoneal transplantation site that had been previously prepared using an adipose tissue-derived stem cell (ASC)-loaded fibrin implant (ASC group) for 14 days prior to grafting. Five mice were grafted using the standard one-step transplantation approach and served as experimental controls (OT group). One piece of ovarian tissue per patient was fixed for analysis to serve as non-grafted tissue controls. Samples were collected after euthanizing the mice on day 7OTT: ovarian tissue transplantation.
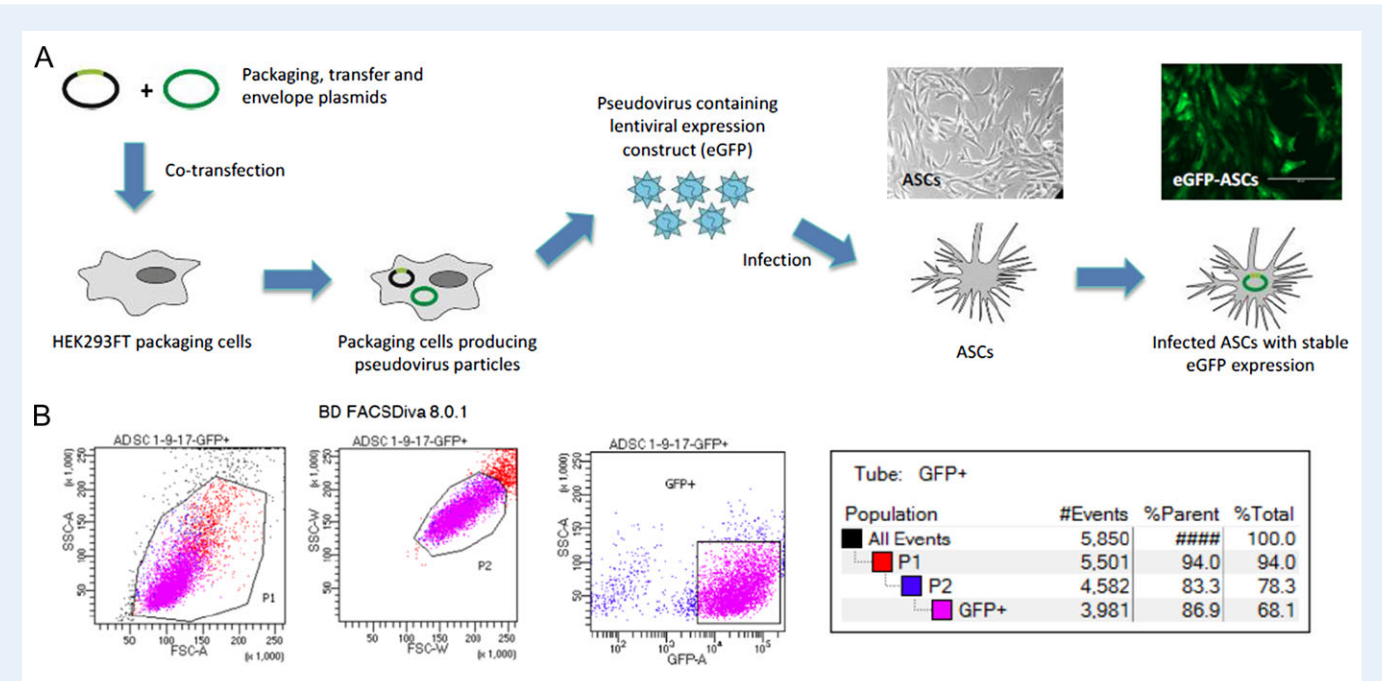
Figure 2 **Enhanced green fluorescent protein labeling protocol and cell sorting results.** (**A**) Description of the steps followed to achieve stable enhanced green fluorescent protein (eGFP) expression in infected ASCs. Magnification: ×10. (**B**) Cell sorting performed to obtain a pure eGFP-ASC population. HEK293FT: human embryonic kidney 293 cell line. ADSC: P1: P2: FSC-A FSC-W.

graft were analyzed with CaseViewer (3DHISTECH, Budapest, Hungary) or the Tissue IA system (Leica Biosystems, Wetzlar, Germany).

Immunolabeling

ASC tracking, graft vascularization and ASC differentiation

The slides were subjected to a triple immunofluorescence protocol targeting CD34 of human and murine origin to assess graft vascularization, and eGFP to reveal the localization and investigate endothelial lineage differentiation of ASCs. Briefly, deparaffinization was performed with X-Solv paraffin-clearing solvent (Yvsolab, Turnhout, Belgium), followed

by immersion in quenching buffer (NH_4Cl, 50 mM). Antigen retrieval was achieved by immersion in citrate buffer for 75 min in a 98°C water bath. The sections were then incubated for 30 min at room temperature with 5% bovine serum albumin (BSA, Sigma Aldrich, Overijse, Belgium) in PBS (Gibco, Paisley, UK) containing 0.1% Tween (VWR, Briare, France) to minimize non-specific antigen binding. Primary antibodies diluted in 1% BSA/PBS-Tween included rabbit eGFP antibody (dilution 1:1500; Novus Biologicals, CO, USA), mouse anti-human CD34 (dilution 1:500; Biocare Medical, Pacheco, CA, USA) and rat anti-mouse CD34 (dilution 1:100; Hycult Biotech, Uden, Netherlands). The fragments were then incubated for 1 hour at room temperature with secondary antibodies, namely

Alexa Fluor 488 anti-rat immunoglobulin (Ig) antibody (Cell Signaling, Leiden, Netherlands), Alexa Fluor 555 anti-rabbit Ig antibody (Cell Signaling, Leiden, Netherlands) and Alexa Fluor 647 anti-mouse Ig antibody (Molecular Probes, OR, USA), all at a dilution of 1:1000. Thereafter, the slides were incubated in Hoechst 33342 (dilution 1:1000, ThermoFisher, Brussels, Belgium) for 30 min at room temperature for nuclear counterstaining and mounted with HIGHDEF IHC fluoromount (Enzo, NY, USA). Negative controls were incubated with secondary antibodies only. Cytospin sections with eGFP-positive cultured ASCs, mouse ovary and human ovarian tissue slides were used as positive controls. Vascularization was calculated and expressed as the number of CD34-positive vessels per section area, in other words, vessel density. To digitize the slides, the following filters were utilized: green (SR-FITC-Zero) for Alexa Fluor 488, yellow (SPGold) for Alexa Fluor 555, orange (SP-CY5-4040c-Zero) for Alexa Fluor 647, and blue (DAPI-5060c-000-Zero) for Hoechst 33342, to detect cell nuclei.

Additional double immunofluorescence protocols targeting CD31 for human vessels and eGFP were also applied to better investigate ASC differentiation (Supplementary Data 1).

Quantitative-RT-PCR for proangiogenic growth factor expression

To evaluate gene expression profiles for the proangiogenic factors vascular endothelial growth factor (VEGF) and fibroblast growth factor (FGF-2), quantitative RT-PCR (RT-qPCR) was performed in grafted tissue from both groups. All stored samples were thawed and transferred to 10-ml tubes containing RLT Plus lysis buffer (with 10 μl/ml β-mercaptoethanol). Disruption and homogenization were carried out using the TissueRuptor (IKA T25 digital ULTRA-TURRAX, Staufen, Germany) for 30 seconds and RNA was extracted immediately after. Nucleic acid extraction and purification were achieved using RNeasy Plus micro kits (Qiagen, Hilden, Germany), as instructed by the manufacturer. DNA/RNA yield was determined using a NanoDrop ND-1000 spectrophotometer (ThermoFisher, Waltham, MA, USA). Reverse transcription for cDNA synthesis was carried out using the Advantage RT-for-PCR kit (Clontech, Fitchburg, USA) on 200 or 500 ng total RNA, as specified in the recommendations. Briefly, total RNA was placed in 12.5 μl diethylpyrocarbonate-treated water, to which 0.5 μl oligo-dT and 0.5 μl random-hexamer primers were added and heated at 70°C for 2 min. After cooling, 6.5 μl cDNA synthesis reagent (5X reaction buffer, 10 mM dNTP mix, recombinant RNase inhibitor and moloney murine leukemia virus reverse transcriptase) was added to each tube, reactions were incubated at 42°C for 1 h and heated at 94°C for 5 min to stop the reaction. The cDNA was used immediately.

For qPCR, selected target probes were VEGF-A (Hs0090055_m1) and FGF-2 (Hs00266645_m1) TaqMan Gene Expression Assays (Applied Biosystems, Thermo Fisher, Waltham, MA, USA). RT-qPCR was performed using the TaqMan Fast Advanced Master Mix (Thermo Fisher, Waltham, MA, USA) in a final volume of 25 μl, containing 5 μl cDNA. Thermal cycling was carried out with an initial denaturation step at 50°C for 2 min and 95°C for 10 min, followed by 50 cycles at 95°C for 15 s and then 60°C for 1 min (StepOnePlus, Applied Biosystems, Stockton, CA, USA). Beta 2 microglobulin (B2M, Hs00187842_m1) was selected as the housekeeping gene after performing preliminary gene expression stability tests (data not shown). The abundance of mRNA for sequences of interest was expressed relative to the constitutively expressed B2M. All samples were amplified in triplicate.

Immunolabeling for growth factor secretion

To assess protein expression and distribution of the proangiogenic factors VEGF and FGF-2, immunohistochemistry was performed, analyzing three sections per sample. Sections were deparaffinized with Histosafe (Yvsolab, Turnhout, Belgium) and rehydrated in 2-propanol (Merck, Darmstadt, Germany). After blocking endogenous peroxidase activity, they were decloaked in citrate buffer for 75 min at 98°C, before incubation for 30 min with goat serum to block non-specific binding sites. The slides were then incubated with mouse anti-human VEGF (dilution 1:200, mAb MA512-184, Invitrogen, Ghent, Belgium) or rat anti-human FGF-2 (dilution 1:2000, pAb, ab8880, Abcam, Burlingame, CA, USA) for 1 h at room temperature. Thereafter, they were incubated for 30 min at room temperature with peroxidase-coupled goat anti-mouse IgG (dilution 1:2, Dako, K4001, Santa Clara, CA, USA) for VEGF and goat anti-rabbit IgG (dilution 1:2, Dako, k4003, Santa Clara, CA,USA) for FGF-2. Diaminobenzidine was used as a chromogen and human pancreatic tissue sections as positive controls. Negative controls were obtained by incubating slides only with secondary antibodies. Growth factor expression in grafts was detected by computer-assisted quantification of staining concentrations using Leica's proprietary artificial intelligence (TissueIA, Wetwlar, Germany) (Courtoy et al., 2018). Double immunofluorescence targeting VEGF and eGFP was also performed for co-localization of growth factor secretion (Supplementary Data 2).

Gene expression profile for proangiogenic growth factors: VEGF, FGF-2

For each sample, the relative amount of RT-qPCR product was determined based on the cycle threshold (Ct) value. Ct values for the B2M housekeeping gene were ascertained for normalization purposes, and ΔCt values were calculated between VEGF and B2M, and between FGF-2 and B2M. Relative quantification was then performed; results for each gene were expressed as the difference in expression levels between the ASC and OT groups, using non-grafted samples as negative controls, following the equation: $2^{-\Delta\Delta Ct}$, with $\Delta\Delta Ct = \Delta Ct_{sample} - \Delta Ct_{negative\ control}$. Samples from one patient were excluded from the analysis due to insufficient DNA yield.

Statistical analysis

Results are presented as means ± SEM. GraphPad Prism, version 7.00 for Windows, (GraphPad Software, San Diego, CA, USA), was utilized for statistical analyses. One-way ANOVA, Fisher's least squares difference multiple comparison and/or Student's t-tests were applied where appropriate. A P value <0.5 was considered statistically significant.

Results

Cell sorting of eGFP-positive ASCs

FACS was performed to sort ASCs in passage 3 according to eGFP expression to obtain a 100% eGFP-positive cell population in order to track ASCs after transplantation. Results of the sorting procedure revealed high efficiency of the transfection protocol, with 68.1% of the population shown to be viable single-cell eGFP-positive ASCs (Fig. 2B), which were subsequently cultured and expanded up to passage 5 prior to transplantation. Repeated tests showed viability of more than 95%.

Macroscopic evaluation of recovered grafts

The graft recovery rate was 100%. On post-grafting Day 7, all recovered ovarian tissue fragments were found to be adherent to the peritoneum, but grafts from the OT group had a visibly more whitish appearance than those from the ASC group. Adhesions were also
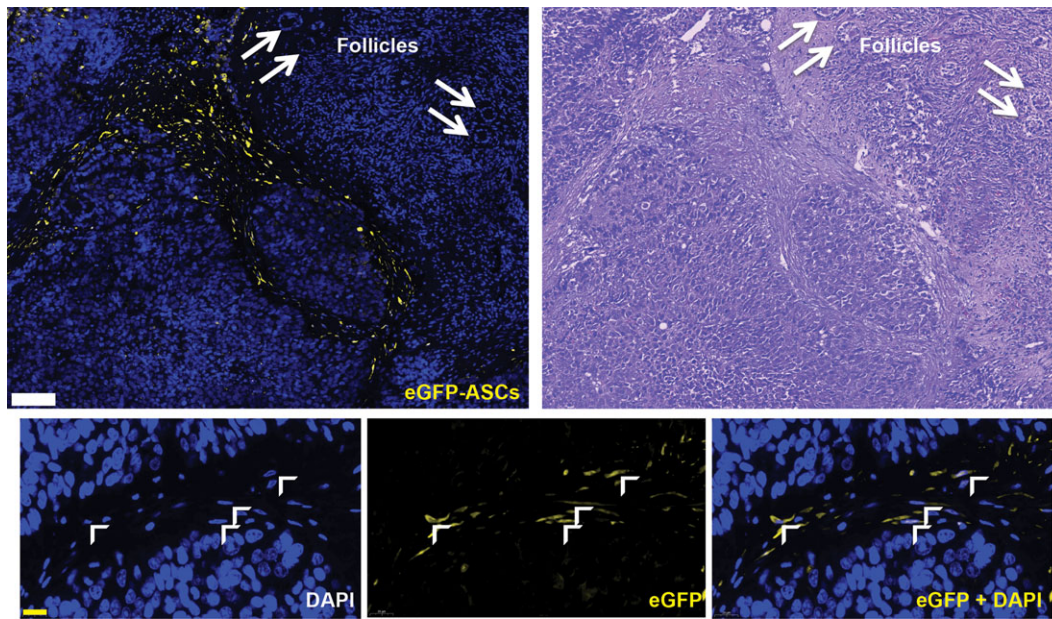
Figure 3 ASC localization and distribution in ovarian tissue grafts. Immunofluorescence targeting the eGFP antigen in ASCs revealed its localization around and infiltrating ovarian tissue grafts. The same slide stained with hematoxylin-eosin for reference of ASC localization. Inset: eGFP localization; arrowheads: eGFP+ cells. White arrows: ovarian follicles; yellow color: eGFP-positive ASCs; Blue color: DAPI-stained nuclei. White scale bar: 100 µm. Yellow scale bar: 20 µm.

observed surrounding the transplantation site in three out of five grafts from the OT group, and one out of five from the ASC group.

ASC tracking

To evaluate post-grafting localization and infiltration of ASCs in recovered ovarian tissue samples, the eGFP antigen was targeted using immunofluorescence (Fig. 3). ASCs positive for eGFP were situated surrounding and infiltrating ovarian tissue grafts. ASCs were found to be part of the extracellular matrix, exhibiting mainly a fibroblast-like shape and distribution.

Graft vascularization and ASC differentiation into endothelial cell lineages

Total vessel density, evaluated by calculating human and murine CD34-positive vessels (Fig. 4A) on Day 7, was significantly higher in the ASC group (291.5 ± 48.72) than in the OT group (135.4 ± 32.44; $P = 0.0182$) (Fig. 4D).Taking murine CD34-positive vessels into account, significantly greater vessel density was observed in the ASC group (116.5 ± 33.04) compared to the OT group (43.32 ± 15.46; $P = 0.0290$) (Fig. 4E). Similar results were evidenced when analyzing the human vessel component, which also showed higher values in the ASC group (216 ± 65.05) than in the OT group (92.1 ± 25.28; $P = 0.0349$) or non-grafted tissue (76.91 ± 8.142; $P = 0.0207$) (Fig. 4F).

ASC differentiation into CD34-positive endothelial cells was assessed by co-expression of antigens for both human CD34 and eGFP (Fig. 4B). Indeed, ASCs were found to differentiate into CD34-positive cells, corresponding to a mean co-expression percentage of $12.15\% \pm 3.61\%$ out of the total number of human vessels. CD31 and

eGFP co-expression was also detected, further corroborating endothelial cell lineage differentiation (Fig. 4). Moreover, eGFP-positive ASCs were found surrounding CD31-positive vessels.

Expression of proangiogenic factors

Relative quantification of VEGF showed significantly higher mRNA expression levels after 7 days in the ASC group (mean fold change: 3.863 ± 0.356) than in the OT group (2.302 ± 0.328; $P = 0.0182$) (Fig. 5A). FGF-2 also showed a tendency towards increased expression in the ASC group (4.391 ± 1.216) compared to the OT group (1.566 ± 0.325), but this difference was not significant ($P = 0.0660$) (Fig. 5D). Moreover, VEGF and eGFP were found to be co-expressed by the same cells, and a significantly positive correlation was also detected between VEGF gene expression and human vessel density (Fig. 6).

Secretion of VEGF and FGF-2

Immunohistochemistry targeting VEGF and FGF-2 (Fig. 5C, F), performed to complement PCR results, revealed a significantly greater VEGF-positive staining concentration in the ASC group ($20.29 \pm 3.62\%$) than in the OT group ($8.78 \pm 2.66\%$; $P = 0.0339$) (Fig. 5B). FGF-2, on the other hand, exhibited more extensive overall staining in grafted tissue, regardless of the transplantation procedure used (Fig. 5E, F). No significant difference was observed between the ASC group ($64.64 \pm 6.44\%$) and the OT group ($48.29 \pm 15.74\%$; $P = 0.3304$) (Fig. 5E) However, regarding VEGF and FGF-2 staining distribution, the most concentrated expression was localized in the same area as eGFP-positive ASCs, as demonstrated by VEGF and eGFP immunofluorescence too, mainly surrounding ovarian tissue grafts in the ASC group (Fig. 5C, F).
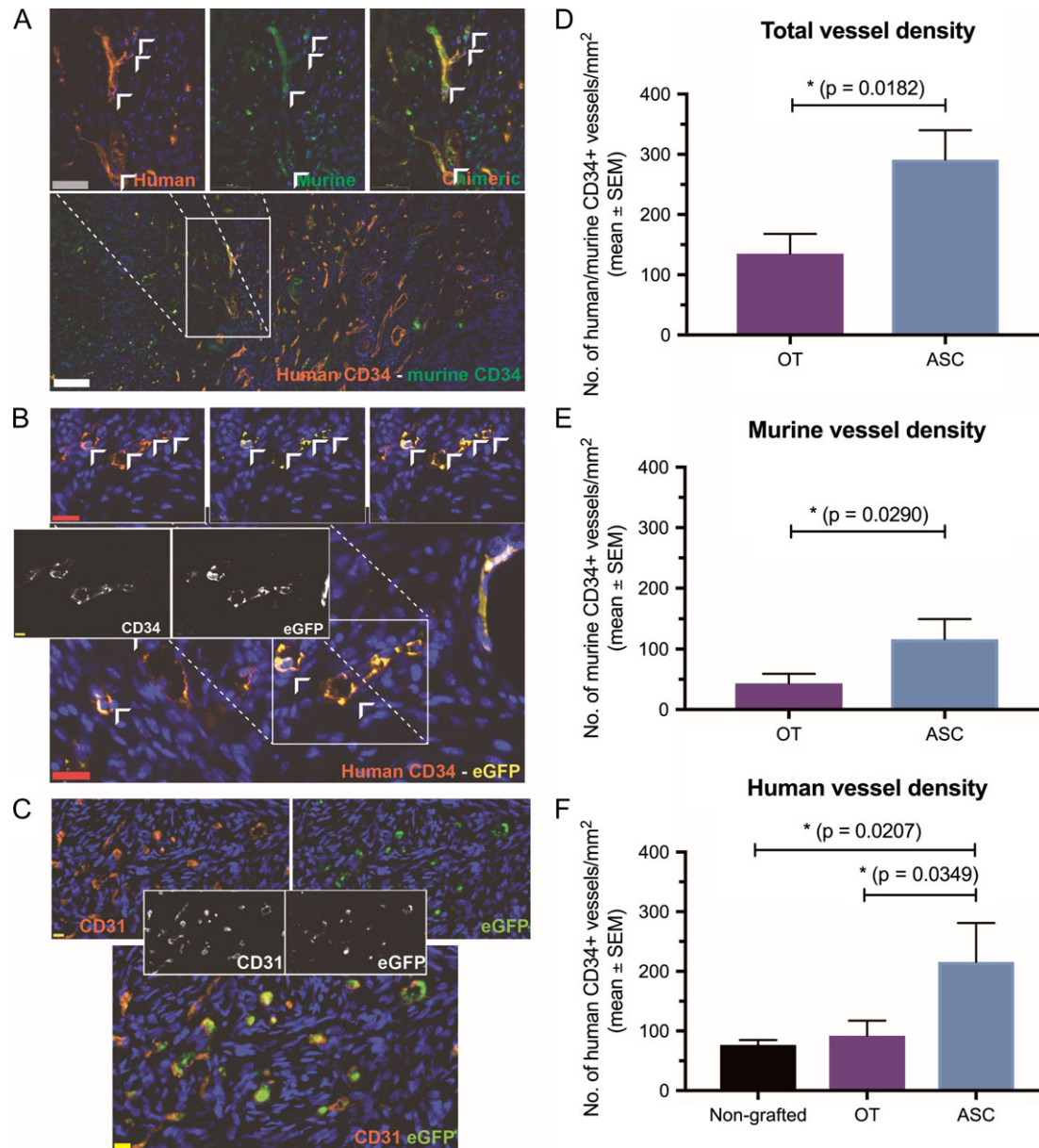
Figure 4 Graft vascularization and ASC differentiation into CD34-positive cells. (**A**) Immunofluorescence targeting human and murine CD34 antigens. Inset: chimeric vessels (merging of human and murine CD34-positive vessels). Red color: human CD34; green color: murine CD34; blue color: DAPI-stained cell nuclei; arrowheads: co-expression in chimeric vessels. Gray scale bar: 50 µm; white scale bar: 100 µm. (**B**) Human CD34-eGFP co-expression in ASCs, with previously CD34-negative cells differentiated into CD34-positive cells, accounting for 12% of human vessel density. Insert: gray-scale images for protein co-expression. Yellow color: eGFP; orange color: human CD34; blue color: DAPI-stained cell nuclei; arrowheads: co-expression in ASCs. Scale bar: 20 µm. (**C**) Human CD31-eGFP co-expression in ASCs. Inset: gray-scale images for protein co-expression. Green color: eGFP; orange color: CD31; blue color: DAPI-stained cell nuclei. Scale bar: 20 µm. (**D**) Total CD34-positive (human and murine) vessel density (one-way ANOVA and Tukey's multiple comparison post-hoc test). (**E**) Murine and (**F**) human CD34-positive vessel density (one-way ANOVA and Fisher's LSD post-hoc test). All graphs show means $\pm$ SEM and $n = 5$ per group.

Discussion

ASCs were first described by Zuk et al. (2002) and, among adult stem cells, they appear to be of most benefit for use in cell therapies and regenerative medicine. Indeed, they have advantages over other sources of MSCs, allowing harvesting from greater amounts of tissue

and a higher cell yield per gram of harvested tissue, as well as retrieval through minimally invasive procedures with significantly less donor site morbidity (Ding et al., 2011; Tobita et al., 2015). The longer time that ASCs take to undergo senescence is an additional advantage, as is their higher proliferation capacity (Barba et al., 2013; Kokai et al., 2014; Wu et al., 2018). Their use in regenerative medicine has also been
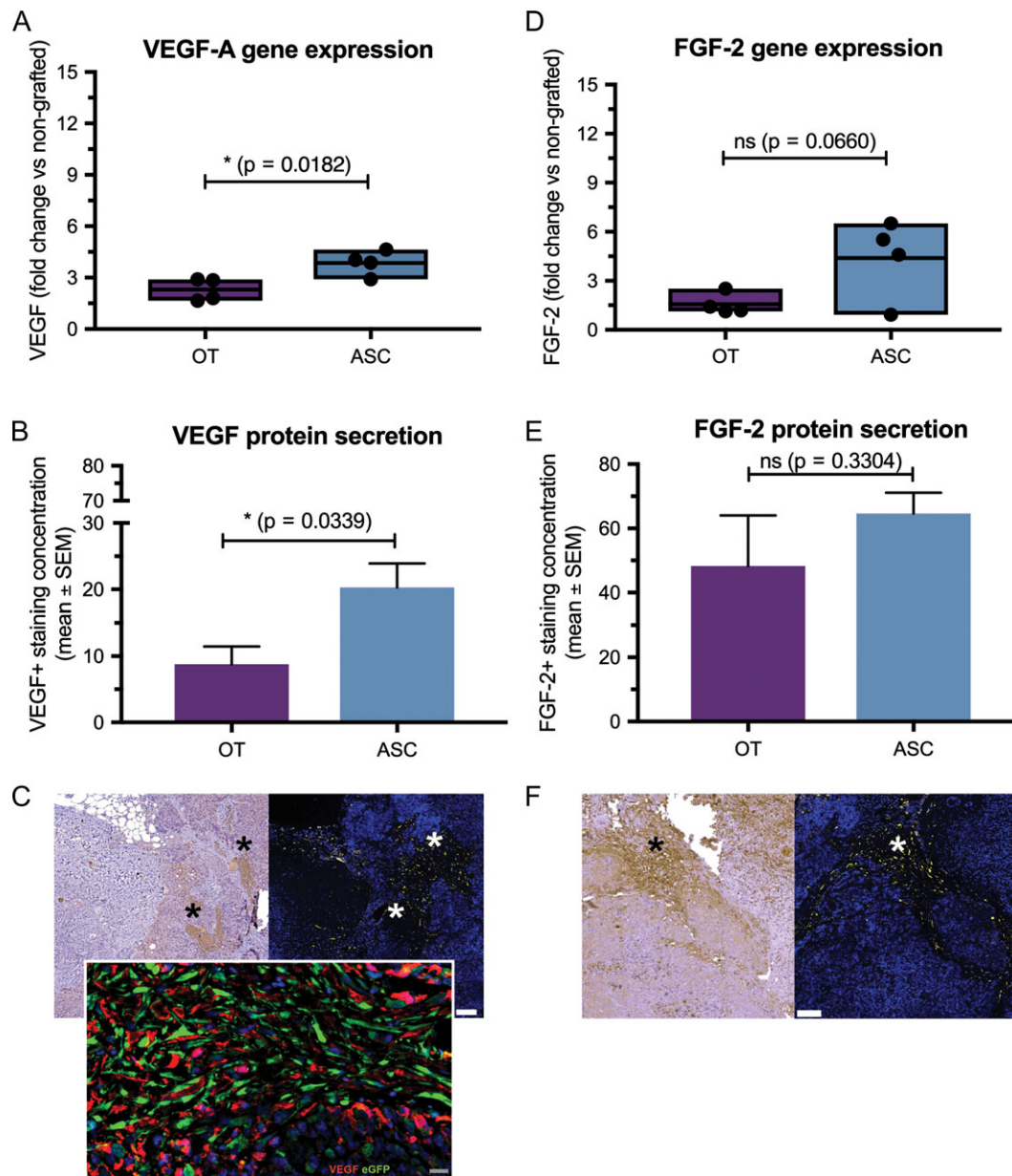
**Figure 5 Growth factor gene expression in human ovarian tissue grafts and co-localization with ASCs.** Vascular endothelial growth factor (VEGF: **A**) and fibroblast growth factor 2 (FGF-2: (**D**) gene expression profiles (quantitative RT-PCR), with fold change compared to non-grafted tissue samples (Student's *t*-test; *n* = 4 per group). A sample from one patient was excluded due to insufficient RNA yield. VEGF (**B**) and FGF-2 (**E**) growth factor quantification by staining concentration (mean ± SEM; Student's *t*-test; *n* = 5 per group). Immunohistochemistry targeting VEGF (**C**) and FGF-2 (**F**) antigens showed more intense staining surrounding ASCs (consecutive eGFP immunofluorescence slides are shown as a reference). Immunofluorescence staining for VEGF-eGPF co-expression (C). HE: hematoxylin and eosin; asterisks: areas stained positive for VEGF and FGF-2. White scale bar: 100 μm; gray scale bar: 20 μm.

spreading over recent years and ASCs have been widely studied in both animal models and humans, and numerous potential clinical applications are being evaluated, with over 100 clinical trials currently underway (https://www.clinicaltrials.gov). ASCs have been shown to have proangiogenic, antiapoptotic and immunomodulatory properties in various biological contexts, explaining the growing interest in their use for regenerative purposes, especially to treat or reduce ischemic damage in tissues (Salgado *et al.*, 2010; Frese *et al.*, 2016).

Human ASCs physiologically reside in a low-tension oxygen niche, where stemness and viability are normally maintained. Variations in oxygen levels can trigger ASC differentiation pathways, including endothelial cell-like lineages (Choi *et al.*, 2014; Cannella *et al.*, 2017) and endothelial progenitor cells (Kang *et al.*, 2014), especially in the presence of proangiogenic growth factors. Indeed, VEGF, hepatocyte growth factor (HGF) and FGF-2 promote differentiation into endothelial cells (De Francesco *et al.*, 2009; Merfeld-Clauss *et al.*, 2010;
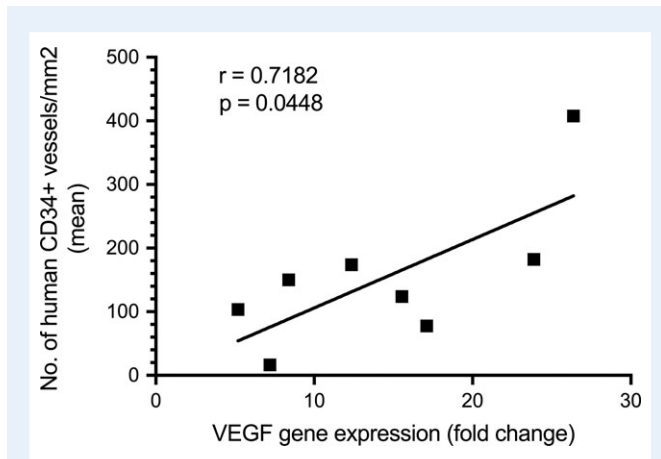
Figure 6 **Correlation between vessel density and VEGF in human ovarian graft tissue**. Correlation between vessel density (y: number human CD34+ vessels/mm^2) and VEGF gene expression (x: fold change by quantitative RT-PCR). *P*: 0.0448; *r*: 0.7182.

Mendel *et al.*, 2013), mainly in hypoxic conditions. ASCs exposed to hypoxia have been shown to increase expression of these factors (Liu *et al.*, 2013), contributing to their proangiogenic behavior probably through mechanisms that involve activation of hypoxia-inducible factor 1 and its downstream effectors (Choi *et al.*, 2017).

In this study, we investigated ASC differentiation into an endothelial cell-like lineage and the secretion of proangiogenic growth factors, mainly VEGF, as potential mechanisms involved in the proangiogenic behavior of ASCs in the context of a recently described short-term two-step ovarian tissue transplantation procedure (Manavella *et al.*, 2018a,b).

Graft vascularization

A recent study using human ovarian tissue from poor responders xenografted to immunocompromised mice was found to improve vascularization by systemic infusion of CD133-positive stem cells derived from bone marrow (Herraiz *et al.*, 2018). MSCs in human ovarian tissue subcutaneously xenografted with Matrigel have also displayed their proangiogenic effects by boosting vascularization in grafts (Xia *et al.*, 2015). Our study clearly demonstrated that two-step ovarian tissue transplantation with ASCs enhances vascularization in ovarian tissue grafts. Indeed, results obtained after analysis of the CD34 antigen by immunohistochemistry revealed significantly higher vessel density in the ASC group after 7 days, supporting previous findings with the same approach (Manavella *et al.*, 2018b).

ASC localization and differentiation into endothelial cell lineages

In order to track ASCs after grafting, a lentiviral eGFP transfection protocol was utilized, which allowed us to obtain a population of cells that expressed the protein constitutively and indefinitely in parent cells, as well as in their progeny. Post-grafting localization of ASCs was achieved by targeting the eGFP antigen by immunofluorescence, and ASCs were found surrounding and infiltrating the graft in some cases. Indeed, ASCs were part of the ovarian tissue extracellular matrix and

displayed a fibroblast-like morphology and pattern. Our findings are consistent with previous observations, where ASCs show a fibroblast-like shape (Hassan *et al.*, 2014), but they may also exhibit an activated fibroblast phenotype, which could potentially increase endothelial cell recruitment *in vivo* (Hong *et al.*, 2013).

Endothelial cell lineage differentiation of ASCs was evaluated by targeting both CD34 and CD31 of human origin and colocalizing them with the eGFP antigen using immunofluorescence, and by assessing the percentage of co-expression in human vessels. We found that an average of 12% of human vessels comprised endothelial-like cells originating from ASCs. This demonstrates that ASCs can indeed transdifferentiate into endothelial-like lineages, as evidenced by their acquisition of the CD34 and CD31 antigens, thus proving their involvement in one of the mechanisms responsible for increased vascularization in the two-step ovarian tissue transplantation procedure. These results are further substantiated by previous studies in which the proangiogenic effects of ASCs were linked to their differentiation potential both *in vitro* and *in vivo* (Bekhite *et al.*, 2013; Kang *et al.*, 2014; Cannella *et al.*, 2017; Amerion *et al.*, 2018). However, their endothelial differentiation capacity has also been attributed to their autocrine and paracrine properties (Bhang Suk *et al.*, 2009; Hsiao *et al.*, 2011).

Proangiogenic growth factor secretion of ASCs

RT-qPCR performed to quantify relative gene expression of VEGF and FGF-2 in recovered ovarian tissue samples after 7 days revealed significant upregulation of VEGF in the ASC group, which translated into a greater VEGF-positive staining concentration per area at immunohistochemistry, especially in the vicinity of ASCs. Our findings therefore demonstrate that ASCs grafted 14 days before ovarian tissue transplantation promote VEGF gene and protein expression in grafted ovarian tissue. Indeed, the positive correlation found between secretion of this growth factor and increased vascularization indicates that ASCs exert a proangiogenic effect on their environment. The aim of this study was not to determine if growth factors are directly responsible for the impact on follicle numbers, as knockout studies were not performed. However, we analyzed the mechanisms by which ASCs enhance vascularization (associated with increased follicular survival: Manavella *et al.*, 2018b) and could demonstrate that one of the mechanisms is by an increase in VEGF secretion. In our study, ASCs underwent hypoxic preconditioning over the course of 14 days of graft site preparation. Our results are corroborated by previous studies, in which ASCs were shown to increase their proangiogenic phenotype when exposed to hypoxic preconditioning (Rubina *et al.*, 2009). Indeed, investigations have shown not only a five-fold increase in VEGF (Rehman *et al.*, 2004) after hypoxic preconditioning, but also enhanced secretion of several other proangiogenic molecules, such as angiogenin, angiopoietin 1 and 2, HGF and its receptor c-Met, platelet-derived growth factor and placental growth factor (Rehman *et al.*, 2004; Nakagami *et al.*, 2005; Sadat *et al.*, 2007; Rubina *et al.*, 2009; Zhang *et al.*, 2017). In the present study, however, FGF-2 showed no significant difference in mRNA expression level and protein secretion, which is consistent with a previous study in which FGF-2 was not upregulated after hypoxic preconditioning compared to normoxia (Oses *et al.*, 2017). Nevertheless, co-localization of the FGF-2 antigen alongside

ASCs provides clear evidence that ASCs do stimulate its secretion in these conditions.

ASC-based therapies show great promise in regenerative medicine and, to our knowledge, no clinically applicable protocol has yet been documented using ASCs in the context of ovarian tissue transplantation. Our findings clearly suggest that grafted ovarian tissue could greatly benefit from the proposed two-step approach using ASCs, thanks to their proangiogenic properties.

Conclusion

In the present study, we demonstrated that ASCs exert their proangiogenic effects in our two-step ovarian tissue transplantation procedure by increasing VEGF gene and protein expression, as well as differentiating into endothelial cell-like lineages. In line with good clinical practice guidelines, future studies should focus on testing the long-term effects of this two-step approach in terms of safety, restoration of endocrine function and live birth rates, before proceeding to potential clinical application.

Supplementary data

Supplementary data are available at *Molecular Human Reproduction* online.

Acknowledgements

Authors' roles

D.D.M.: Experimental design, experimental procedures, analyses, statistical analysis, interpretation of results and article preparation. L.C.: Experimental procedures, participation in article preparation. V.P.: Experimental procedures, article revision. J.D.: Article preparation and revision. C.A.A.: Article preparation and revision. M.M.D.: Experimental design, experimental procedures, interpretation of results and article revision.

Funding

Conflict of interest

None of the authors have any conflict of interest to declare in relation to the present study.

References

Amerion M, Valojerdi MR, Abroun S, Totonchi M. Long term culture and differentiation of endothelial progenitor like cells from rat adipose derived stem cells. *Cytotechnology* 2018;**70**:397–413.

Amorim CA, Dolmans MM, David A, Jaeger J, Vanacker J, Camboni A, Donnez J, Van Langendonckt A. Vitrification and xenografting of human ovarian tissue. *Fertil Steril* 2012;**98**:1291–1298.e1291–1292.

Baird DT, Webb R, Campbell BK, Harkness LM, Gosden RG. Long-term ovarian function in sheep after ovariectomy and transplantation of autografts stored at -196 C. *Endocrinology* 1999;**140**:462–471.

Barba M, Cicione C, Bernardini C, Michetti F, Lattanzi W. Adipose-derived mesenchymal cells for bone regereneration: state of the art. *Biomed Res Int* 2013;**2013**:11.

Bekhite MM, Finkensieper A, Rebhan J, Huse S, Schultze-Mosgau S, Figulla H-R, Sauer H, Wartenberg M. Hypoxia, leptin, and vascular endothelial growth factor stimulate vascular endothelial cell differentiation of human adipose tissue-derived stem cells. *Stem Cells Dev* 2013;**23**:333–351.

Bhang SH, Cho SW, Lim JM, Kang JM, Lee TJ, Yang HS, Song YS, Park MH, Kim HS, Yoo KJ *et al.* Locally delivered growth factor enhances the angiogenic efficacy of adipose-derived stromal cells transplanted to ischemic limbs. *Stem Cells* 2009;**27**:1976–1986.

Cannella V, Piccione G, Altomare R, Marino A, Di Marco P, Russotto L, Di Bella S, Purpari G, Gucciardi F, Cassata G *et al.* Differentiation and characterization of rat adipose tissue mesenchymal stem cells into endothelial-like cells. *Anat Histol Embryol* 2017;**47**:11–20.

Choi JR, Pingguan-Murphy B, Wan Abas WAB, Noor Azmi MA, Omar SZ, Chua KH, Wan Safwani WKZ. Impact of low oxygen tension on stemness, proliferation and differentiation potential of human adipose-derived stem cells. *Biochem Biophys Res Commun* 2014;**448**:218–224.

Choi JR, Yong KW, Wan Safwani WKZ. Effect of hypoxia on human adipose-derived mesenchymal stem cells and its potential clinical applications. *Cell Mol Life Sci* 2017;**74**:2587–2600.

Courtoy GE, Henriet P, Marbaix E, de Codt M, Luyckx M, Donnez J, Dolmans M-M. Matrix metalloproteinase activity correlates with uterine myoma volume reduction after ulipristal acetate treatment. *J Clin Endocrinol Metab* 2018;**103**:1566–1573.

De Francesco F, Tirino V, Desiderio V, Ferraro G, D'Andrea F, Giuliano M, Libondi G, Pirozzi G, De Rosa A, Papaccio G. Human CD34/CD90 ASCs are capable of growing as sphere clusters, producing high levels of VEGF and forming capillaries. *PLoS One* 2009;**4**:e6537.

Ding D-C, Shyu W-C, Lin S-Z. Mesenchymal stem cells. *Cell Transplant* 2011;**20**:5–14.

Dominici M, Le Blanc K, Mueller I, Slaper-Cortenbach I, Marini F, Krause D, Deans R, Keating A, Prockop D, Horwitz E. Minimal criteria for defining multipotent mesenchymal stromal cells. The International Society for Cellular Therapy position statement. *Cytotherapy* 2006;**8**:315–317.

Donnez J, Dolmans MM. Fertility preservation in women. *Nat Rev Endocrinol* 2013;**9**:735–749.

Donnez J, Dolmans M-M. Fertility preservation in women. *N Engl J Med* 2017;**377**:1657–1665.

Donnez J, Dolmans M-M, Diaz C, Pellicer A. Ovarian cortex transplantation: time to move on from experimental studies to open clinical application. *Fertil Steril* 2015;**104**:1097–1098.

Frese L, Dijkman PE, Hoerstrup SP. Adipose tissue-derived stem cells in regenerative medicine. *Transfus Med Hemother* 2016;**43**:268–274.

Hassan WU, Greiser U, Wang W. Role of adipose-derived stem cells in wound healing. *Wound Repair Regen* 2014;**22**:313–325.

Herraiz S, Buigues A, Díaz-García C, Romeu M, Martínez S, Gómez-Seguí I, Simón C, Hsueh AJ, Pellicer A. Fertility rescue and ovarian follicle growth promotion by bone marrow stem cell infusion. *Fertil Steril* 2018;**109**:908–918.e2.

Hong SJ, Jia SX, Xie P, Xu W, Leung KP, Mustoe TA, Galiano RD. Topically delivered adipose derived stem cells show an activated-fibroblast phenotype and enhance granulation tissue formation in skin wounds. *PLoS One* 2013;**8**:e55640.

Hsiao ST-F, Asgari A, Lokmic Z, Sinclair R, Dusting GJ, Lim SY, Dilley RJ. Comparative analysis of paracrine factor expression in human adult mesenchymal stem cells derived from bone marrow, adipose, and dermal tissue. *Stem Cells Dev* 2011;**21**:2189–2203.

Kang B-J, Lee SH, Kweon O-K, Cho J-Y. Differentiation of canine adipose tissue–derived mesenchymal stem cells towards endothelial progenitor cells. *Am J Vet Res* 2014;**75**:685–691.

Kokai LE, Marra K, Rubin JP. Adipose stem cells: biology and clinical applications for tissue repair and regeneration. *Transl Res* 2014;**163**:399–408.

Liu L, Gao J, Yuan Y, Chang Q, Liao Y, Lu F. Hypoxia preconditioned human adipose derived mesenchymal stem cells enhance angiogenic potential via secretion of increased VEGF and bFGF. *Cell Biol Int* 2013;**37**:551–560.

Luyckx V, Dolmans MM, Vanacker J, Legat C, Fortuno Moya C, Donnez J, Amorim CA. A new step toward the artificial ovary: survival and proliferation of isolated murine follicles after autologous transplantation in a fibrin scaffold. *Fertil Steril* 2014;**101**:1149–1156.

Manavella DD, Cacciottola L, Desmet CM, Jordan BF, Donnez J, Amorim CA, Dolmans MM. Adipose tissue-derived stem cells in a fibrin implant enhance neovascularization in a peritoneal grafting site: a potential way to improve ovarian tissue transplantation. *Hum Rep* 2018a;**33**:270–279.

Manavella DD, Cacciottola L, Pomme S, Desmet CM, Jordan BF, Donnez J, Amorim CA, Dolmans MM. Two-step transplantation with adipose tissue-derived stem cells increases follicle survival by enhancing vascularization in xenografted frozen-thawed human ovarian tissue. *Hum Rep* 2018b;**33**:1107–1116.

Mendel TA, Clabough EB, Kao DS, Demidova-Rice TN, Durham JT, Zotter BC, Seaman SA, Cronk SM, Rakoczy EP, Katz AJ *et al*. Pericytes derived from adipose-derived stem cells protect against retinal vasculopathy. *PLoS One* 2013;**8**:e65691.

Merfeld-Clauss S, Gollahalli N, March KL, Traktuev DO. Adipose tissue progenitor cells directly interact with endothelial cells to induce vascular network formation. *Tissue Eng Part A* 2010;**16**:2953–2966.

Nakagami H, Maeda K, Morishita R, Iguchi S, Nishikawa T, Takami Y, Kikuchi Y, Saito Y, Tamai K, Ogihara T *et al*. Novel autologous cell therapy in ischemic limb disease through growth factor secretion by cultured adipose tissue–derived stromal cells. *Arterioscler Thromb Vasc Biol* 2005;**25**:2542.

Nisolle M, Casanas-Roux F, Qu J, Motta P, Donnez J. Histologic and ultra-structural evaluation of fresh and frozen-thawed human ovarian xeno-grafts in nude mice. *Fertil Steril* 2000;**74**:122–129.

Oses C, Olivares B, Ezquer M, Acosta C, Bosch P, Donoso M, Léniz P, Ezquer F. Preconditioning of adipose tissue-derived mesenchymal stem cells with deferoxamine increases the production of pro-angiogenic, neuroprotective and anti-inflammatory factors: Potential application in the treatment of diabetic neuropathy. *PLoS One* 2017;**12**:e0178011.

Rehman J, Traktuev D, Li J, Merfeld-Clauss S, Temm-Grove CJ, Bovenkerk JE, Pell CL, Johnstone BH, Considine RV, March KL. Secretion of angiogenic and antiapoptotic factors by human adipose stromal cells. *Circulation* 2004;**109**:1292–1298.

Rubina K, Kalinina N, Efimenko A, Lopatina T, Melikhova V, Tsokolaeva Z, Sysoeva V, Tkachuk V, Parfyonova Y. Adipose stromal cells stimulate angiogenesis via promoting progenitor cell differentiation, secretion of angiogenic factors, and enhancing vessel maturation. *Tissue Eng Part A* 2009;**15**:2039–2050.

Sadat S, Gehmert S, Song YH, Yen Y, Bai X, Gaiser S, Klein H, Alt E. The cardioprotective effect of mesenchymal stem cells is mediated by IGF-I and VEGF. *Biochem Biophys Res Commun* 2007;**363**:674–679.

Salgado AJ, Goncalves RI, Sousa NJC, Gimble JM. Adipose tissue derived stem cells secretome: soluble factors and their roles in regenerative medicine. *Curr Stem Cell Res Ther* 2010;**5**:103–110.

Tobita M, Tajima S, Mizuno H. Adipose tissue-derived mesenchymal stem cells and platelet-rich plasma: stem cell transplantation methods that enhance stemness. *Stem Cell Res Ther* 2015;**6**:215.

Van Eyck AS, Jordan BF, Gallez B, Heilier JF, Van Langendonckt A, Donnez J. Electron paramagnetic resonance as a tool to evaluate human ovarian tissue reoxygenation after xenografting. *Fertil Steril* 2009;**92**:374–381.

Wu H, Li J-z, Xie B-d, Tian H, Fang S-h, Jiang S-l, Kang K. Lower senescence of adipose-derived stem cells than donor-matched bone marrow stem cells for surgical ventricular restoration. *Stem Cells Dev* 2018;**27**:612–623.

Xia X, Yin T, Yan J, Yan L, Jin C, Lu C, Wang T, Zhu X, Zhi X, Wang J *et al*. Mesenchymal stem cells enhance angiogenesis and follicle survival in human cryopreserved ovarian cortex transplantation. *Cell Transplant* 2015;**24**:1999–2010.

Zhang Y, Xia X, Yan J, Yan L, Lu C, Zhu X, Wang T, Yin T, Li R, Chang HM *et al*. Mesenchymal stem cell-derived angiogenin promotes primodial follicle survival and angiogenesis in transplanted human ovarian tissue. *Reprod Biol Endocrinol* 2017;**15**:18.

Zuk PA, Zhu M, Ashjian P, De Ugarte DA, Huang JI, Mizuno H, Alfonso ZC, Fraser JK, Benhaim P, Hedrick MH. Human adipose tissue is a source of multipotent stem cells. *Mol Biol Cell* 2002;**13**:4279–4295.

molecular human reproduction

ORIGINAL ARTICLE

Generation of immortalized human endometrial stromal cell lines with different endometriosis risk genotypes

S.J. Holsdworth-Carson [1,*], **E.M. Colgrave** [1], **J.F. Donoghue** [1], **J.N. Fung** [2], **M.L. Churchill**[1], **S. Mortlock**[2], **P. Paiva** [1], **M. Healey**[1,3], **G.W. Montgomery** [2], **J.E. Girling** [1,4], and **P.A.W. Rogers** [1]

[1]Department of Obstetrics and Gynaecology and Gynaecology Research Centre, Royal Women's Hospital, University of Melbourne, Cnr Grattan Street and Flemington Road, Parkville, Victoria 3052, Australia [2]The University of Queensland, The Institute for Molecular Bioscience, 306 Carmody Rd, Brisbane, Queensland 4072, Australia [3]Royal Women's Hospital, Cnr Grattan Street and Flemington Road, Parkville, Victoria 3052, Australia [4]University of Otago, School of Biomedical Sciences, Department of Anatomy, 270 Great King Street, Dunedin 9016, New Zealand

*Correspondence address. Department of Obstetrics and Gynaecology and Gynaecology Research Centre, Royal Women's Hospital, University of Melbourne, Parkville, Victoria 3052, Australia. E-mail: scarson@unimelb.edu.au orcid.org/0000-0002-3533-0486

Endometriotic lesions are composed in part of endometrial-like stromal cells, however, there is a shortage of immortalized human endometrial stromal cultures available for research. As genetic factors play a role in endometriosis risk, it is important that genotype is also incorporated into analysis of pathological mechanisms. Human telomerase reverse transcriptase (hTERT) immortalization (using Lenti-hTERT-green fluorescent protein virus) took place following genotype selection; 13 patients homozygous for either the risk or non-risk 'other' allele for one or more important endometriosis risk single nucleotide polymorphism on chromosome 1p36.12 (rs3820282, rs56318008, rs55938609, rs12037376, rs7521902 or rs12061255). Short tandem repeat DNA profiling validated that donor tissue matched that of the immortalized cell lines and confirmed that cultures were genetically novel. Expression of morphological markers (vimentin and cytokeratin) and key genes of interest (telomerase, estrogen and progesterone receptors and LINC00339) were examined and functional assays for cell proliferation, steroid hormone and inflammatory responses were performed for 7/13 cultures. All endometrial stromal cell lines maintained their fibroblast-like morphology (vimentin-positive) and homozygous endometriosis-risk genotype following introduction of hTERT. Furthermore, the new stromal cultures demonstrated positive and diverse responses to hormones (proliferation and decidualisation changes) and inflammation (dose-dependent response), while maintaining hormone receptor expression. In conclusion, we successfully developed a range of human endometrial stromal cell lines that carry important endometriosis-risk alleles. The wider implications of this approach go beyond advancing endometriosis research; these cell lines will be valuable tools for multiple endometrial pathologies offering a level of genetic and phenotypic diversity not previously available.

Key words: endometrium / endometriosis / risk allele / stroma / cell culture / immortalization / hTERT

Introduction

Endometriosis is an estrogen-dependent gynaecological disorder that occurs in 6–10% of reproductive aged women (Giudice, 2010). Common symptoms of endometriosis include pelvic pain and sub-fertility. Endometriosis is characterized by lesions consisting of endometrial-like stroma and epithelium, found most commonly in the pelvis. The endometrial-like cells which form endometriotic lesions are thought to originate from eutopic endometrium, which is shed and expelled into the peritoneal cavity during retrograde menstruation (Sampson, 1925). Consequently, human endometrial stromal cells (hESC) are used routinely

in cell culture work for investigation of endometriosis. One limitation of cell culture with primary endometrial cells is obtaining adequate human tissue for research purposes. Furthermore, primary hESC vary in phenotype from batch to batch and are difficult to maintain in long-term culture as they gradually lose their endometrial stromal cell phenotype (Krikun et al., 2004; Barbier et al., 2005; Yuhki et al., 2011). To overcome these obstacles, primary cells can be immortalized, a process whereby cell division is prolonged through incorporation of human telomerase reverse transcriptase (hTERT) into the cells. At present there is only one reliable

immortalized hESC line transfected with hTERT that is commercially available (Krikun et al., 2004).

While the cellular mechanisms responsible for the development of endometriotic lesions are largely unknown, there is an established genetic component to the disease. Genome-wide association studies (GWAS) have identified genomic regions associated with increased endometriosis risk (Fung et al., 2015b; Sapkota et al., 2017). Expression quantitative trait loci (eQTL) are essential to understanding the functional implications of GWAS. An eQTL is a polymorphism that is associated with transcript abundance and therefore, eQTLs may provide clues as to how polymorphisms affect gene expression in a trait or disease (Gibson et al., 2015). There are several published eQTLs associated with endometriosis (Fung et al., 2015a, 2017, 2018; Holdsworth-Carson et al., 2016), and most recently we demonstrated a strong tissue-specific eQTL at 1p36.12 for decreased expression of a long intergenic non-protein coding RNA 339 (LINC00339) in the endometrium ($P = 2.4 \times 10^{-8}$) (Powell et al., 2016). Studying the genetic landscape of women with endometriosis is essential if we are to improve our understanding of the altered cellular mechanisms involved in disease development.

There is a shortage of suitable human cell culture models for endometriosis research; consequently, an understanding of the cellular mechanisms that drive this common gynaecological disease is lacking. The aim of this work is to generate and characterize a set of immortalized hESC lines derived from women with defined endometriosis-associated single nucleotide polymorphisms (SNPs) on chromosome 1p36.12. Moving forward, these immortalized cell lines will be an invaluable in vitro tool for studies of endometriosis providing researchers with variations in genetic background not previously available.

Materials and Methods

Tissue collection and consent

Endometrial tissue samples were collected by curettage from women recruited through the Royal Women's Hospital (Melbourne). Women undergoing laparoscopy provided informed written consent before surgery. Ethical approval for the study was obtained from the Human Research Ethics Committee (Projects 10-43 and 11-24) of the Royal Women's Hospital. In addition to providing a blood sample and tissues; clinical, surgical and pathology information was collected for each participant. A portion of each endometrial biopsy was evaluated by an experienced gynaecological pathologist and classified either according to menstrual cycle stage, or as inactive, influenced by exogenous progestins, or as unknown (unable to confidently classify based on available tissue). It was our priority to generate stromal cell lines from women with important endometriosis-associated SNPs (specific to chromosome 1p36.12), of which the homozygous risk allele (RA) occurred at a low frequency; therefore, we were not able to control for contraception use or menstrual cycle stage. Endometriosis or non-endometriosis status was allocated following detailed surgical investigation based on the revised American Fertility Society (rAFS) or the American Society for Reproductive Medicine definitions (Medicine, 1997) as determined by the surgeon. Samples were de-identified and designated an internal 4-digit identifying number that was used to distinguish the different cell lines. Endometrial curettes were collected in theatre into 20 ml of chilled Dulbecco's Modified Eagle Medium/ Nutrient Mixture F12, HEPES (DMEM/F12, HEPES) (with 5% (v/v) new born calf serum and 1x antibiotic–antimycotic) (Thermo Fisher Scientific, Scoresby, Australia). Samples were stored at 4°C and processed immediately or the following morning (within 24 h). A total of 39 primary hESC cultures were established and stored over a 12-month period.

SNP genotyping

DNA from whole blood, endometrial tissue and cell cultures were extracted using QIAGEN DNeasy Blood & Tissue extraction kits (Hilden, Germany). DNA samples were genotyped on HumanCoreExome chips (Illumina, Inc., San Diego, CA, United States). Standard quality control procedures were applied as outlined previously (Luong et al., 2013). Patient genotypes were examined to select appropriate primary stromal cell cultures for hTERT immortalization. Of the 39 patients, 13 were selected because they were homozygous for either the RA or the non-risk 'other' allele (OA) for at least one specific endometriosis-associated SNP on chromosome 1 (1p36.12). These SNPs included rs12037376, rs3820282, rs56318008, rs55938609 and rs7521902 (Powell et al., 2016). Although not an endometriosis risk SNP, rs12061255 was also included for selection as it showed a significant eQTL for LINC00339 expression. SNP rs12037376 at the 1p36.12 locus has the largest effect size overall on endometriosis risk (P-value 8.87×10^{-17}) (Sapkota et al., 2017). All of the SNPs on chromosome 1, except for rs12061255, are in high or moderate linkage disequilibrium (LD) (in Europeans, LD between the four SNPs rs56318008, rs55938609, rs12037376 and rs3820282 are high with $R^2 > 0.9$, and rs7521902 has an R^2 of ~0.5 with these four SNPs) (Powell et al., 2016).

The genotypes of hTERT immortalized hESC cultures for each patient were also compared with the genotypes of the matched whole blood and endometrial tissue to demonstrate genotype stability.

Primary culture of hESC

Human ESC were isolated as described previously (Dimitriadis et al., 2002), with some modifications. Briefly, endometrial tissue was rinsed with phosphate buffered saline (PBS), manually minced and enzymatically digested with 0.375 mg/ml Collagenase III (Sigma-Aldrich, Castle Hill, Australia), 25 µg/ml DNase I (Roche, Hawthorn, Australia) and 10 mg/ml glucose (Sigma-Aldrich) in PBS at 37°C in a shaking incubator. When a single cell suspension was obtained it was filtered sequentially through 45 and 10 µm filters (Allied Filter Fabrics, Hornsby, Australia) to remove epithelial cells. (Note: We were unable to produce sufficient yield (coupled with poor survival) and purity of epithelial cells to pursue immortalization of these cultures.) Red blood cells were lysed with ACK (Ammonium-Chloride-Potassium) lysing buffer as per manufacturer's instructions (Thermo Fisher Scientific). The endometrial stromal cell suspension was pelleted and resuspended in culture media (DMEM/F12 / 10% (v/v) foetal calf serum (FCS)/1x insulin-transferrin-selenium-ethanolamine (ITS-X)/1x antibiotic–antimycotic (Thermo Fisher Scientific)). Primary hESC, passage 0 (P0), were cultured in 25 cm^2 flasks and chamber slides at 10 000 cells/ cm^2 in a humidified CO_2 incubator at 37°C. Flasks of primary P0 hESC were grown to confluence, trypsinised, frozen and stored in liquid nitrogen until SNP genotypes were determined, and appropriate cultures could be selected for immortalization.

hTERT immortalization of hESC

Selected endometrial stromal cells were thawed and plated at passage 1 (P1) in three wells of a 48-well plate (0.25×10^5 cells per well) in culture media for 24 h until 50% confluent. Cells were immortalized using a Lenti-hTERT-green fluorescent protein (GFP) virus (Applied Biological Materials Inc., Richmond, Canada) with ViralPlus Transduction Enhancer (1:50 dilution) (Applied Biological Materials Inc.) and polybrene (8 µg/ml) (Merck Millipore, Bayswater, Australia). The amount of Lenti-hTERT-GFP virus for successful transfection was determined empirically; a multiplicity of

infection (MOI) of 200 was determined to be most efficient and employed in these studies. Controls were included in the second and third wells; a blank GFP virus (Lenti-CMV-GFP-2A-Puro, Applied Biological Materials Inc.) and a no-virus control. Twenty-four hours following transfection, the media was replaced. Between 2 and 7 days post-transfection, cells were monitored for lentivirus vector uptake (GFP expression) using an inverted fluorescent microscope (Olympus, Notting Hill, Australia). hTERT transfected hESC cultures were grown to near confluence before media containing puromycin (0.75 µg/ml) (Thermo Fisher Scientific) was added. Drug selection occurred over 5 days, which was sufficient time to kill nontransfected cells including the no-infection control. Puromycin resistant hTERT immortalized hESC were grown to confluence in puromycin-free DMEM/F12/20% FCS/1x ITS-X/1x antibiotic–antimycotic until the next passage. The hTERT hESC were then maintained in DMEM/F12/10% FCS/1x ITS-X/1x antibiotic–antimycotic. A specialized fibroblast media, Medium 106 (M106) plus 1x Low Serum Growth Supplement (LSGS) and 1x antibiotics–antimycotic (Thermo Fisher Scientific), was also employed on some of the new hTERT lines.

Culture of telomerase-transformed HESC line

Transformed HESCs (T HESC) were a gift to PAWR from Dr Graciela Krikun (Yale University) (Krikun *et al.*, 2004) and were maintained in DMEM/F12/10% FCS/1x ITS-X/1x antibiotic–antimycotic. Culture media was refreshed every 2–3 days and cells were passaged every 4–6 days with trypLE express (Thermo Fisher Scientific). The T HESC line was used to compare with the newly established hTERT hESC cultures against steroid receptor expression and *in vitro* assays.

Immunocytochemistry

Primary P0 endometrial stromal cultures grown in chamber slides were fixed with 4% (w/v) paraformaldehyde and stained for vimentin (mouse monoclonal antibody [clone V9]; Thermo Fisher Scientific) and cytokeratin (mouse monoclonal antibody; Agilent, Mulgrave, Australia) to confirm purity of isolations; stromal cells were positive for vimentin and negative for cytokeratin (Dimitrov *et al.*, 2008). Following several passages the GFP control and hTERT immortalized endometrial stromal cell cultures were grown in chamber slides and examined by immunocytochemistry (ICC) for vimentin, cytokeratin and steroid hormone receptors estrogen receptor alpha (ESR1) (mouse monoclonal antibody [clone 6F11]; Abcam, Melbourne, Australia), estrogen receptor beta (ESR2) (rabbit monoclonal antibody [clone EPR3778]; Abcam) and progesterone receptor (PR) (rabbit monoclonal antibody [clone D8Q2J]; Cell Signaling Technology, Arundel, Australia). The appropriate isotype controls (Agilent) were included in each ICC experiment.

Fixed cells were washed (PBS) and permeabilized with 0.1% triton X-100 in PBS for 30 min at room temperature (RT). Peroxidases were blocked with 0.3% H_2O_2 for 10 min at RT then non-specific protein were blocked using Protein Block, serum-free (Agilent) for 10 min, RT. Antibodies and isotype controls in 1% (w/v) BSA (Sigma Aldrich) were incubated overnight at 4°C. Antibody concentrations were as follows; vimentin 0.14 µg/ml, cytokeratin 0.18 µg/ml, ESR1 0.63 µg/ml, ESR2 2.2 µg/ml and PR 0.63 µg/ml. REAL EnVision Detection System with Peroxidase/DAB+ chromogen (Agilent) was used for visualization. ICCs were counterstained with Mayer's haematoxylin for 1 min and mounted with aqueous Ultramount Permanent Mounting Medium (Agilent).

The percentage of vimentin-, cytokeratin-, ESR1-, ESR2- and PR-positive cells was calculated by counting the number of brown-stained cells or brown-stained nuclei relative to the total number of haematoxylin-stained cells in five fields of view (centre, top left, top right, bottom left and bottom right).

Short tandem repeat DNA profiling

Short tandem repeat (STR) profiling was performed on the 13 new hTERT endometrial stromal cell lines, matching donor endometrial tissue and the T HESC line. STR was used to confirm integrity of the cells against the matched donor tissue and novelty of each line from other existing cell lines. Profiling was also used to ascertain a unique STR DNA profile for each new cell line for any future comparisons/authentication.

Frozen endometrial tissue (10–20 mg) and cell pellets (1 million cells) were provided to the Garvan Institute of Medical Research (Darlinghurst, NSW, Australia) for DNA extraction and subsequent STR profiling using the PowerPlex 18D System (which reports allele calls for 18 different STR loci; D5S818, D13S317, D7S820, D16S539, vWA, TH01, Amel, TPOX, CSF1PO, D8S1179, D21S11, D3S1358, D2S1338, D19S433, D18S51, FGA, Penta E and Penta D). Profiles were analysed against three databases (biorepository agencies ATCC and DSMZ, and an internal Garvan database) and samples were considered to match if their profiles were more than 80% identical. STR DNA profiling authenticated the T HESC line, demonstrating a STR profile identical to T HESCs ATCC-CRL-4003.

Proliferation assay

The T HESC line and new hTERT cultures (1399, 1405, 1429, 1433, 1455 and 1458) were examined for cell proliferation using the RealTime Glo MT Cell Viability Assay (Promega, Alexandria, New South Wales, Australia), following the manufacturer's instructions. Prior to seeding, all cell lines were cultivated in DMEM/F12 (as described above) except for 1399 and 1405, which were grown in M106. Since 1455 cells grew well in both types of media, 1455 cells originating from both DMEM/F12 and M106 medium were included in proliferation assays. Single cell suspensions were seeded into 96-well plates (1000–4000 cells/well) in phenol red-free DMEM/F12/5% (charcoal stripped) csFCS/1x ITS-X/1x antibiotics–antimycotic and incubated overnight in a humidified CO_2 incubator at 37°C. The following day, estradiol 17-β (E, estrogen), medroxyprogesterone acetate (MPA) and estrogen + MPA combined were added to the wells at a final concentration of 10^{-5} M (Sigma-Aldrich). A vehicle control was also included (0.01% DMSO) per cell line. Luminescence readings were taken using a FLUOstar Omega microplate reader (BMG Labtech, Mornington, Victoria, Australia). Fold change in luminescence was calculated every 24 h for 6 days. The growth rate was calculated as LN (fold change N_1/fold change N_2)/total N, where N = day. Cell doubling time was calculated on Day 3 using the following formula, LN (2)/growth rate. Assays were repeated twice in triplicate. Hormone-treated proliferation data is displayed as a fold-change relative to vehicle for Days 1 and 3, normalized to Day 0.

Decidualisation assay

Aliquots from a subset of new hTERT endometrial stromal cell lines (1399, 1405, 1429, 1433, 1455 and 1458) were seeded into 12-well plates and decidualized over 72 h in the presence of estrogen (10^{-8} M), MPA (10^{-7} M) and cAMP (0.01 M) (all from Sigma-Aldrich) in DMEM/F12/2% csFCS/1x ITS-X/1x antibiotic–antimycotic or M106/serum-free/1x antibiotics–antimycotic (Yuhki *et al.*, 2011; Kommagani *et al.*, 2016). Vehicle controls were also included for each experiment. Cell morphology was observed before and after decidualisation. Cells were collected and stored at −80°C for RNA extraction, specifically to examine expression levels of decidualisation markers insulin-like growth factor-binding protein 1

(IGFBP1) and prolactin (PRL). Decidualisation was performed in triplicate per cell line.

Inflammatory response assay

Aliquots from a subset of new hTERT endometrial stromal cell lines (1399, 1405, 1429, 1433, 1455 and 1458) and the T HESC line were seeded in 12-well plates (40 000 cells/well) and grown to ~80% confluence before they were serum starved overnight (DMEM/F12/1% csFCS/1× ITS-X/1× antibiotics–antimycotic or M106/serum-free/1× antibiotics–antimycotic). The following day, cells were treated with lipopolysaccharide (LPS) (10, 100 and 10 000 ng/ml) (Sigma-Aldrich) or vehicle (PBS) for 24 h (Rashidi et al., 2015), before cells were collected and stored at −80°C for RNA extraction. Assays were performed in triplicate per cell line.

RNA extraction, cDNA synthesis and real-time PCR

RNA was extracted using Direct-zol RNA MicroPrep kits (Zymo Research, California, USA) or ReliaPrep RNA Cell Miniprep kits (Promega) following the manufacturer's instructions. RNA concentrations were quantified using a NanoDrop (Thermo Fisher Scientific). RNA was converted to cDNA using Affinity Script QPCR cDNA Synthesis kits (Agilent).

Real-time PCR experiments were performed using a 7500 Real-Time PCR instrument and TaqMan assays (Thermo Fisher Scientific). The following FAM TaqMan assays were used: TERT (#Hs00972560_m1), LINC00339 (#Hs04402696_m1), ESR1 (#Hs00174860_m1), ESR2 (#Hs0023095 7_m1), PR (#Hs01556702_m1), IGFBP1 (#Hs00236877_m1), PRL (#Hs001 68730_m1), CXCL8 (#Hs00174103_m1), IL1B (#Hs01555410_m1), NFKB1 (#Hs00765730_m1), CXCL5 (#Hs01099660_g1), B2M (#Hs0018784 2_m1) and RPL13A (#Hs01926559_g1). Two microliters of diluted cDNA (dilution 1:20) was used per 10 µl reaction using Brilliant III Ultra-Fast QRT-PCR Master Mix (Agilent). Quantification of gene expression were normalized to the average C_t values of human beta-2-microglobulin (B2M) and ribosomal protein L13a (RPL13A) housekeeping genes using the comparative threshold cycle method. B2M and RPL13A were selected as they were stably expressed, non-hormone responsive and demonstrated negligible variability (data not shown).

Statistics

Statistical analysis was performed using GraphPad Prism (version 7, GraphPad software, CA, USA). Expression data (ICC) and LPS-response experiments were analysed by ANOVA with Tukey's post hoc test. Decidualisation and hormone-treated proliferation data were analysed using t tests. A P-value <0.05 was considered statistically significant for all analyses.

Results

Patient selection and SNP genotyping

We selected cells from 13 patients who were homozygous (RA or OA) for at least one of six endometriosis-associated SNPs on chromosome 1p36.12 (rs3820282, rs56318008, rs55938609, rs12037376, rs7521902 or rs12061255) to undergo hTERT immortalization. Due to the lower allele frequency of RA variants in the population, cell lines were more likely to be homozygous for an OA SNP relative to the RA genotype. A list of patient characteristics is provided in Table I. The 10 out of 13 women had surgically confirmed endometriosis, 12 out of 13 reported severe menstrual pain (or dysmenorrhoea) and 11 out of 13 reported chronic pelvic pain. Women had various other common

Table I Patient characteristics.

Characteristic		
	Median (range)	
Age (years)	32 (23–41)	
Age at menarche (years)	13 (11–17)	
Gravidity	0 (0–3)	
Parity	0 (0–2)	
BMI (kg/m^2)	25 (19.3–39.6)	
	Percentage (n*)	
Current smoker	17% (2)	
Previous smoker	46% (6)	
Cycle stage	Mid proliferative	31% (4)
	Early Secretory	15% (2)
	Late Secretory	8% (1)
	Progestin	15% (2)
	Inactive	15% (2)
	Unknown	15% (2)
Hormone therapy	None	54% (7)
	Mirena	8% (1)
	OCP	38% (5)
Endometriosis**	77% (10)	
Stage of endometriosis (n = 10 with endometriosis)	Stage I	40% (4)
	Stage II	30% (3)
	Stage III	0% (0)
	Stage IV	30% (3)
rAFS score (median, range)	10 (1–135)	
Severe menstrual pain	92% (12)	
Severe pelvic pain	85% (11)	
Dysparunia	77% (10)	
Uterine fibroids^	31% (4)	
Adenomyosis^	54% (7)	
Uterine polyp^	8% (1)	
Previous cervical cancer/precancer^	15% (2)	
PCOS^	23% (3)	

*n = 13 unless otherwise stated. **Visually confirmed by the surgeon, but not by pathology. ^Self-reported and/or clinically reported. rAFS = revised American Fertility Society; BMI = body mass index; PCOS = polycystic ovarian syndrome; OCP = oral contraceptive pill.

gynaecological co-morbidities (e.g. 31% reported uterine fibroids and 54% reported adenomyosis) and 6 out of 13 women reported that they were concurrently taking hormone medications.

Use of SNP genotyping confirmed that the genotypes of the 13 immortalized hESC lines matched those of the original donors (whole blood and endometrial tissue) (data not shown), demonstrating that the immortalization process did not alter the original SNP makeup of the cells. In addition to SNPs at the 1p36.12 risk loci, thirteen other genomic regions harbour significant risk loci for endometriosis (Sapkota et al., 2017). Therefore, the hTERT hESC lines were examined for key endometriosis risk SNPs present on chromosomes 2, 4, 6, 7, 9, 11 and 12. Table II displays the RA and OA status of all 14 key

Table II The presence of homozygous risk alleles (RA) or other risk alleles (OA) for 14 key SNPs with genome wide significance for endometriosis.

Associated gene	Cytoband	SNP	RA Percentage % (*n*)	OA	Het.
WNT4	1p36.12	rs12037376	15% (2)	77% (10)	8% (1)
GREB1	2p25.1	rs11674184	31% (4)	15% (2)	54% (7)
ETAA1	2p14	rs6546324	0% (0)	69% (9)	31% (4)
IL1A	2q13	rs10167914	8% (1)	62% (8)	31% (4)
FN1	2q35	rs1250241	8% (1)	31% (4)	62% (8)
KDR	4q12	rs1903068	31% (4)	31% (4)	38% (5)
ID4	6p22.3	rs760794	31% (4)	38% (5)	31% (4)
CCDC170	6q25.1	rs1971256	8% (1)	46% (6)	46% (6)
SYNE1	6q25.1	rs71575922	0% (0)	62% (8)	38% (5)
–	7p12.3	rs74491657	69% (9)	0% (0)	31% (4)
CDKN2B-AS1	9p21.3	rs1537377	46% (6)	15% (2)	38% (5)
FSHB	11p14.1	rs74485684	77% (10)	0% (0)	23% (3)
VEZT	12q22	rs4762326	38% (5)	8% (1)	54% (7)
–	7p15.2	rs12700667	69% (9)	0% (0)	31% (4)

RA, risk allele; OA, other risk allele; Het., heterozygous; SNP, single nucleotide polymorphism.

Table III Short tandem repeat (STR) DNA profile results for each hTERT hESC line relative to its matching donor endometrial tissue.

	1399	1399	1400	1400	1405	1405	1406	1406	1415	1415	1418	1418	1429	1429
	Cells	Tissue	Cells	Tissue	Cells	Tissue	Cells	Tissue	Cells	Tissue	Cells	Tissue	Cells	Tissue
Match *	100%		94%		100%		100%		97%		97%		100%	
	1433	1433	1440	1440	1441	1441	1448	1448	1455	1455	1458	1458		
	Cells	Tissue	Cells	Tissue	Cells	Tissue	Cells	Tissue	Cells	Tissue	Cells	Tissue		
	97%		100%		100%		100%		100%		100%			

*The degree of identity matching between the cell line and the original donor tissue. Cell lines and donor tissue are considered to be a match if their profiles are more than 80% identical.

SNPs with genome wide significance for endometriosis in our 13 cell lines (note that only SNP rs12037376 is listed for 1p36.12 as per Sapkota *et al.*, 2017).

STR DNA profiling

All 13 newly established immortalized hESC lines were found to have unique STR profiles (data not shown). The STR profile of the donor endometrial tissue was analysed against its matched hTERT hESC line, and each cell line was confirmed to match the tissue of origin (matches ranging between 94 and 100%) (Table III).

hTERT immortalized endometrial stromal cell cultures: morphology and expression of genes of interest

Figure 1 depicts GFP-positive hESC following the successful introduction of lenti-hTERT-GFP and 5 days of puromycin drug-selection. The immortalization process did not impact on stromal cell marker expression, with hTERT immortalized stromal cells maintaining their vimentin-positive and cytokeratin-negative status (Fig. 2a–d). The endometrial stromal cell cultures maintained a fibroblast-like appearance before and after immortalization (Fig. 2e–i). Cells were spindle (bipolar) or stellate (multipolar) shaped and grew in parallel arrangements when near confluence. In contrast to the T HESC line (Fig. 2j), the hTERT hESC were larger in size (Fig. 2e–i).

The uptake of the lenti-hTERT was further validated by RT-PCR. Telomerase (*TERT*) mRNA was detected in all the newly established cell lines as well as the T HESC line (Fig. 3). We then examined the cell lines (and primary cultures) for the expression of steroid hormone receptors. The range in expression levels was variable, however, *ESR1*, *ESR2* and *PR* mRNA were detected in all the hTERT immortalized endometrial stromal cell lines and median expression levels were not significantly different compared to the primary (P0) cell cultures (Fig. 3). Nuclear protein expression of the hormone receptors (ESR1,
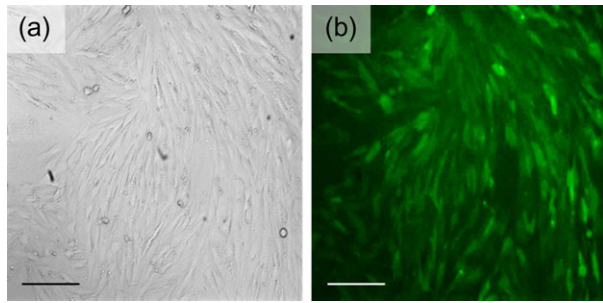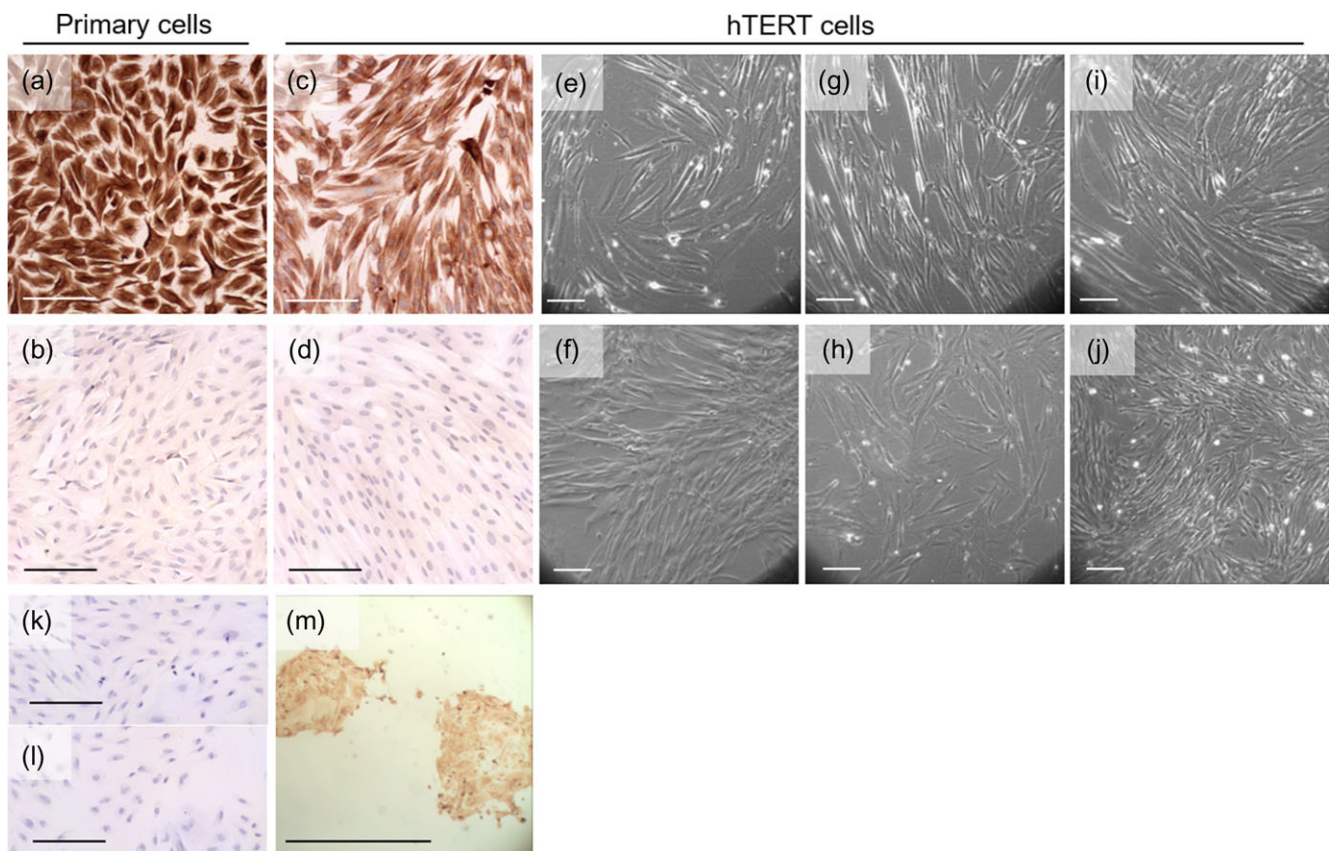
Figure 1 Representative image of human endometrial stromal cells (passage [P] 2) following immortalization with the lenti-human telomerase reverse transcriptase (hTERT)-green fluorescent protein (GFP) virus (multiplicity of infection [MOI] of 200) and subsequent puromycin treatment. The same field of view captured in (**a**) brightfield and (**b**) fluorescence demonstrating GFP positivity. Scale bar = 100 μm.

ESR2 and PR) was also confirmed by ICC (Fig. 4a–c). The median level of protein expression in immortalized cells was not different to the median levels found in primary (P0) cells (Fig. 4d–f). The strongest endometrial eQTL at 1p36.12 is for *LINC00339* (Powell *et al.*, 2016) and we report that all hESC lines express *LINC00339* mRNA at varying levels (Fig. 5).

Proliferation of hTERT immortalized endometrial stromal cell lines

The new hTERT hESC lines displayed variable growth rates. To improve growth ability, the cells were grown in specialized M106 fibroblast media. Some of the cell cultures grew better in M106 media compared to the original DMEM/F12 media (1399, 1405, 1415, 1418, 1441 and 1448), while others did not (1406, 1429, 1433, 1440 and 1458). 1400 and 1455 grew equally in both types of culture media.

Proliferation assays were performed on a subset of cell lines that were observed to have encouraging growth rates (1399, 1405, 1429, 1433, 1455 [both media types] and 1458) relative to the T HESC line.

Figure 2 Representative images of human endometrial stromal cells which were vimentin-positive (a and c) and cytokeratin-negative (b and d). Primary stromal cells (P0) are shown in (**a**) and (**b**) and hTERT immortalized stromal cells (P6) are shown in (**c**) and (**d**). Brightfield images demonstrate the fibroblast-like morphology of hTERT immortalized human endometrial stromal cell cultures (**e–i**) relative to the telomerase-transformed human endometrial stromal cell (T HESC) line (**j**). No antibody control (**k**), IgG1 isotype control (**l**) and cytokeratin positive control showing brown staining of primary (P0) epithelial cells (**m**). Scale bar = 100 μm.
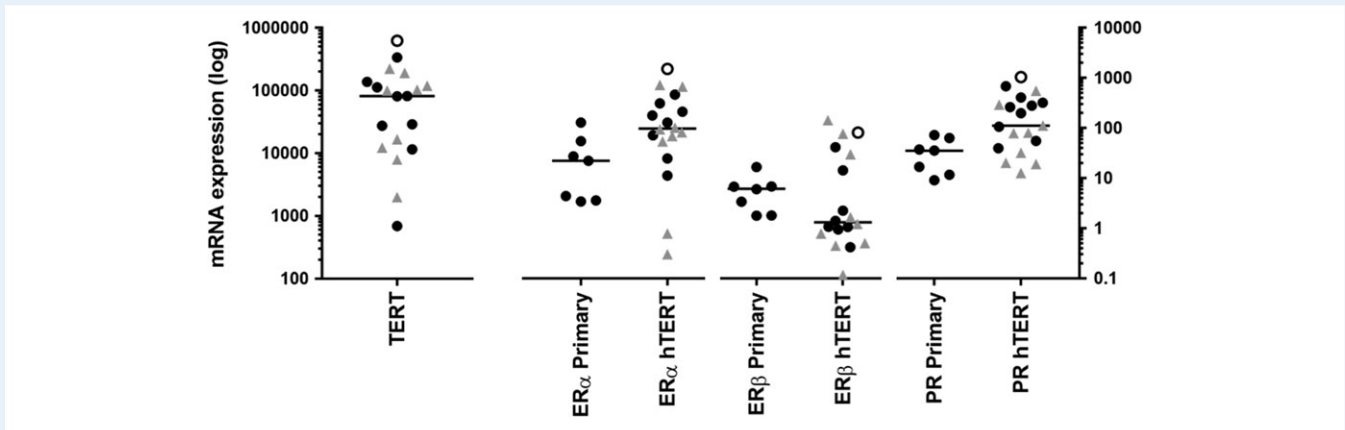
Figure 3 **mRNA expression of *TERT*, estrogen receptor alpha (*ESR1*), estrogen receptor beta (*ESR2*) and progesterone receptor (*PR*) in primary (P0) and hTERT immortalized ESC (between P3 and P7) (relative to housekeeping genes).** Median expression of each gene is indicated by the black bar. Left-hand *y*-axis is for *TERT*, right-hand *y*-axis is for *ESR1*, *ESR2* and *PR*. Closed black circles; cells grown in Dulbecco's Modified Eagle's medium (DMEM)/12 media, open circles; T HESC and grey triangles; cells grown in M106 media.
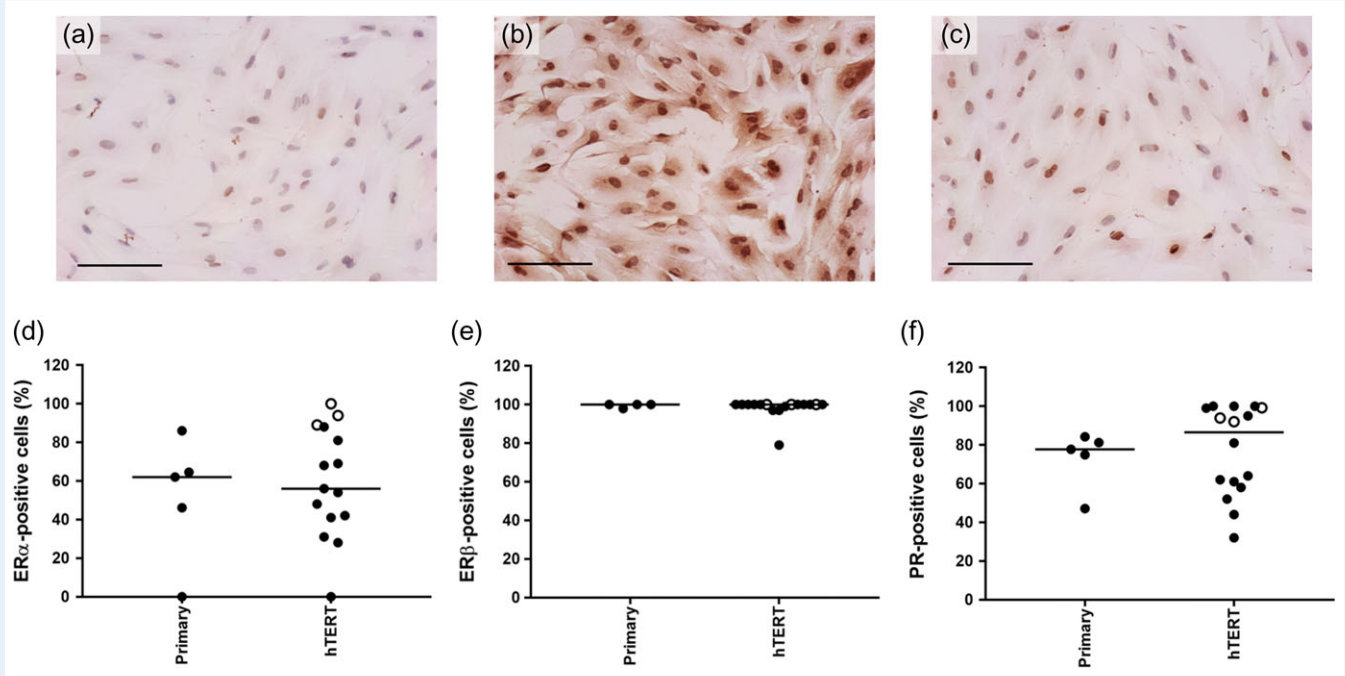

Figure 4 **Protein expression of hormone receptors in primary (P0) and human hTERT immortalized endometrial stromal cells (ESC).** Primary cultures distinct from the hTERT hESC lines (*n* = 4 or 5), were employed for immunocytohistochemistry (ICC) analysis. Representative images of hTERT cells stained for estrogen receptor alpha (ESR1) (**a**), estrogen receptor beta (ESR2) (**b**) and progesterone receptor (PR) (**c**) where brown equals positive staining. Scale bar = 100 μm. The percentage of positive cells are graphed for ESR1 (**d**), ESR2 (**e**) and PR (**f**) with median expression indicated by the black bar.

The fastest growing cells were 1455 (growing in DMEM/F12 and M106) with doubling times of 1.13 and 1.15 days, respectively, then followed by 1429 with a doubling time of 1.31 days (Fig. 6). The slowest in the group was 1433, with a doubling time of 2.47 days. The T HESC cell line had a doubling time of 1.26 days (Fig. 6a). Proliferation increased in a linear fashion over 3 days for all cell lines (Fig. 6b). Cells continued to increase linearly over time, except for 1433 and 1458 which plateaued by Day 6 (Fig. 6b). We report that several of these cell lines have been grown beyond passage 20 (including 1455, 1458 and 1433). Some of the new cell lines (and the T HESC line) demonstrated a significant increase fold-change in cell proliferation in the presence of estrogen relative to vehicle (Fig. 6c, d and h). In contrast,
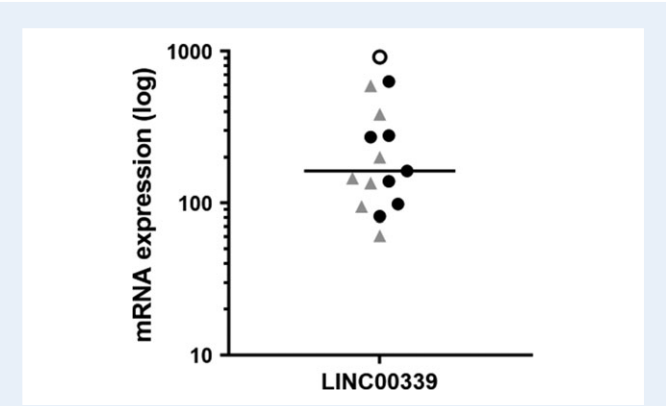
Figure 5 **mRNA expression of long intergenic non-protein coding RNA 339 (*LINC00339*) in hTERT immortalized endometrial stromal cells (between P3 and P7) (relative to housekeeping genes).** Closed black circles; cells grown in DMEM/12 media, open circle; T HESC and grey triangles; cells grown in M106 media.

MPA treatment (alone or combined with estrogen) reduced cell proliferation compared to vehicle-treatment in some cultures (Fig. 6d, e, g and h).

Decidualisation capacity of hTERT immortalized endometrial stromal cell lines

A decidual cell appearance developed in 1399 and 1405 cell lines, but not in the remaining immortalized cell lines following the 72 hr decidualisation protocol (Fig. 7a and b). Following decidualisation treatment however, all the cell lines demonstrated a significant increase in decidual cell-associated markers *IGFBP1* and/or *PRL* mRNA expression relative to vehicle (Fig. 7c and d). Two cell lines (1399 and 1433) did not demonstrate an increase in *IGFBP1* mRNA in response to decidualisation, however, both cell lines showed a significant increase in *PRL* expression following decidualization.
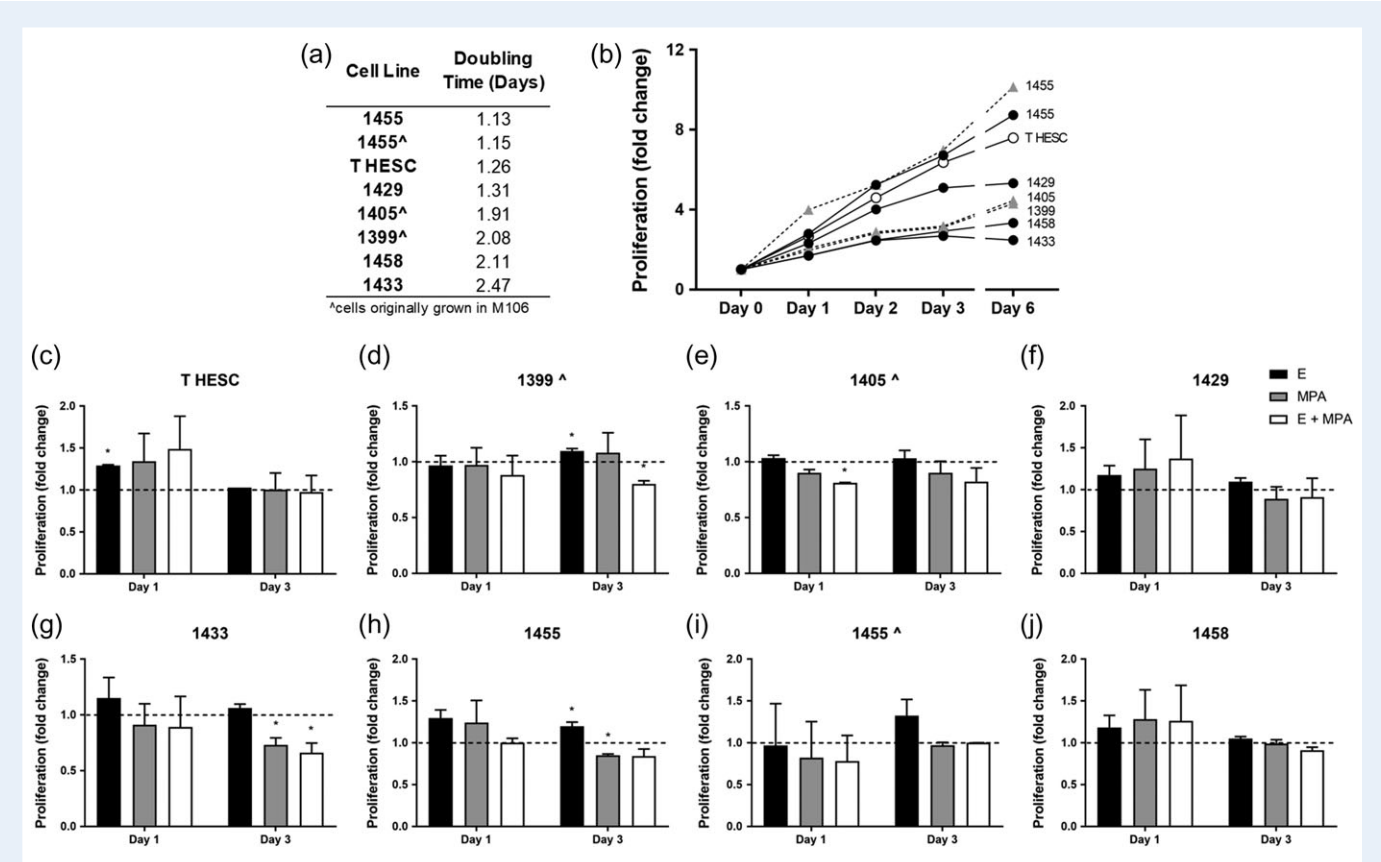
Figure 6 **Varying cell proliferation of hTERT endometrial stromal cell cultures.** (**a**) Doubling time of the T HESC cell line and 1399, 1405, 1429, 1433, 1455 and 1458. ^Cells grown in M106 medium prior to the assay. Doubling time was calculated on Day 3. (**b**) Proliferation measured over 6 days for the same cultures. Black circles; cells grown in DMEM/12 media, open circles; T HESC and grey triangles; cells grown in M106 media. (**c–j**) Proliferation fold change shown for Day 1 and Day 3 in response to hormone treatments: estradiol (E), medroxyprogesterone acetate (MPA) and E + MPA for the T HESC cell line and 1399, 1405, 1429, 1433, 1455 and 1458 hTERT ESC lines. Fold change shown relative to vehicle (dashed line = 1.0). Significant difference between vehicle and hormone treatment is denoted by * (*P*-value < 0.05).
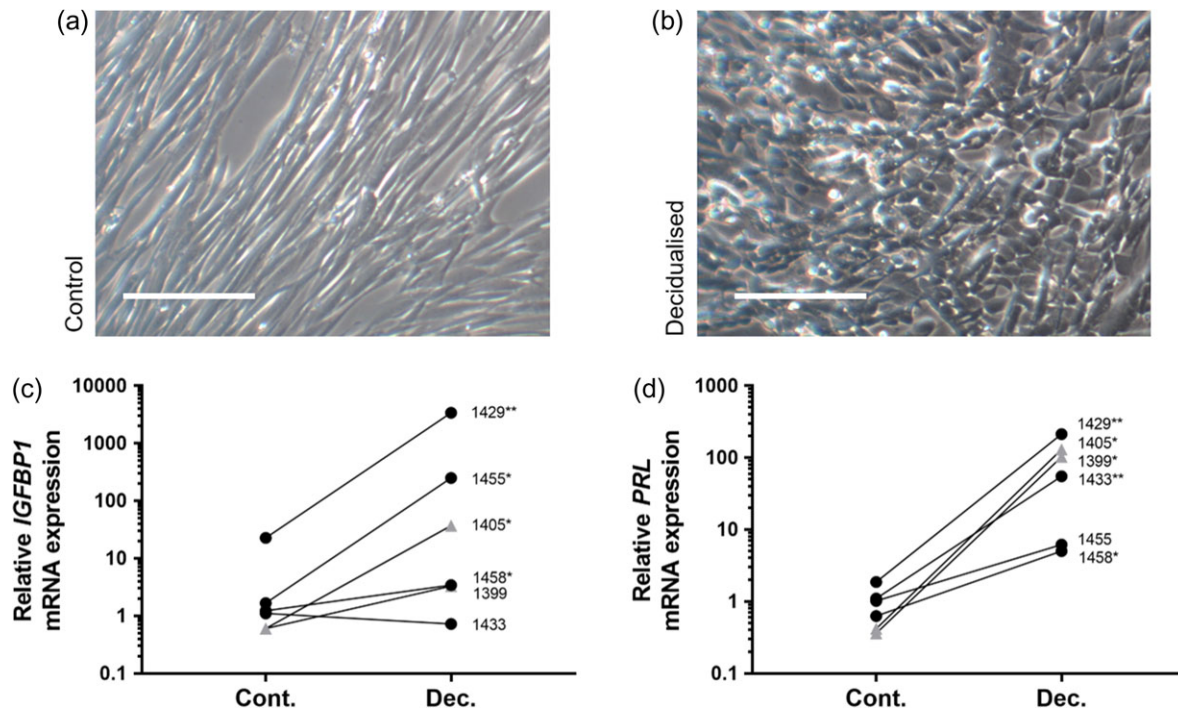
Figure 7 Decidual phenotype of immortalized endometrial stromal cells following 72 h of (a) vehicle control or (b) hormone treatment. Only 1399 and 1405 demonstrated these phenotypic cell changes. Decidualised cells appear enlarged, polygonal and epithelial-like. Scale bar = 100 μm. mRNA expression of decidualisation markers. (**c**) Insulin-like growth factor-binding protein 1 (*IGFBP1*) and (**d**) prolactin (*PRL*) in hTERT endometrial stromal cell cultures following decidualisation (estrogen, MPA + cAMP for 72 h). Each point represents the mean expression ($n = 3$) for vehicle control (Cont.) and decidualised (Dec.) cell treatments. Closed circles; cells grown in DMEM/12 media and triangles; cells grown in M106 media. A *t*-test was performed to determine significance in differential gene expression of *IGFBP1* or *PRL* for each cell line. Significant difference between Cont. and Dec. are denoted by ** (*P*-value <0.0001) and * (*P*-value <0.05).

Inflammatory response of hTERT immortalized endometrial stromal cell lines

The hTERT hESC lines were exposed to increasing doses of LPS to determine if they would respond to an inflammatory stimulus. Overall, the new hTERT lines and T HESC exhibited a dose dependent linear increase to LPS when examining pro-inflammatory *CXCL8* and *IL1B* mRNA expression (Fig. 8a and b). There was also a dose dependent increase in *CXCL5* mRNA in response to LPS in 1433, 1405, 1455 and 1399 cell lines, but not the T HESC or the remaining hTERT hESC lines (Fig. 8c). There was little change in *NFKB1* expression in response to LPS stimuli (Fig. 8d). Most of the hTERT cell lines exhibited higher levels of *CXCL8*, *IL1B*, *CXCL5* and *NFKB1* mRNA expression relative to the T HESC line in the presence of vehicle and in response to LPS (Fig. 8a–d).

Discussion

Cultures of hESC are integral tools for laboratory-based investigations into the cellular mechanisms associated with endometriosis. To overcome the limitations of reduced life span of primary cell cultures and a lack of diversity of available commercial cell lines, we have generated our own hTERT immortalized hESC lines. The immortalized hESC maintained their fibroblast-like morphology and endometriosis-risk genotype. Furthermore, the new hESC lines functioned like primary cultures showing positive but diverse responses to exogenous hormone and inflammatory stimuli, while maintaining significant hormone receptor expression levels. We have grown immortalized cultures beyond passage 20 and can report that they have retained endometrial stromal cell phenotype as described above. These immortalized cell lines have been genetically characterized and will facilitate future *in vitro* studies of endometriosis (and other reproductive traits) while recognizing the importance of genotype. Therefore, we have described and validated the use of hTERT immortalization of hESC with different endometriosis risk genotypes; this practice should be employed by other research groups to improve the quality and impact of laboratory-based cell research.

One of the primary aims of this work was to increase the genotypic diversity of hESC lines, with an emphasis on known endometriosis RAs. The SNP (rs12037376) with the largest effect size on endometriosis risk is at the *WNT4* (Wnt Family Member 4) 1p36.12 locus (*P*-value 8.87×10^{-17}) (Sapkota *et al.*, 2017). SNPs in this region demonstrate significant eQTL in whole blood and endometrium, decreasing the expression of a long intergenic non-protein coding RNA 339 (*LINC00339*), and include rs3820282, rs56318008, rs55938609, rs12037376 and rs7521902 (Powell *et al.*, 2016). In contrast, rs12061255 (minor allele) increased the expression of *LINC00339* in endometrium (Powell *et al.*, 2016). One patient was homozygous RA
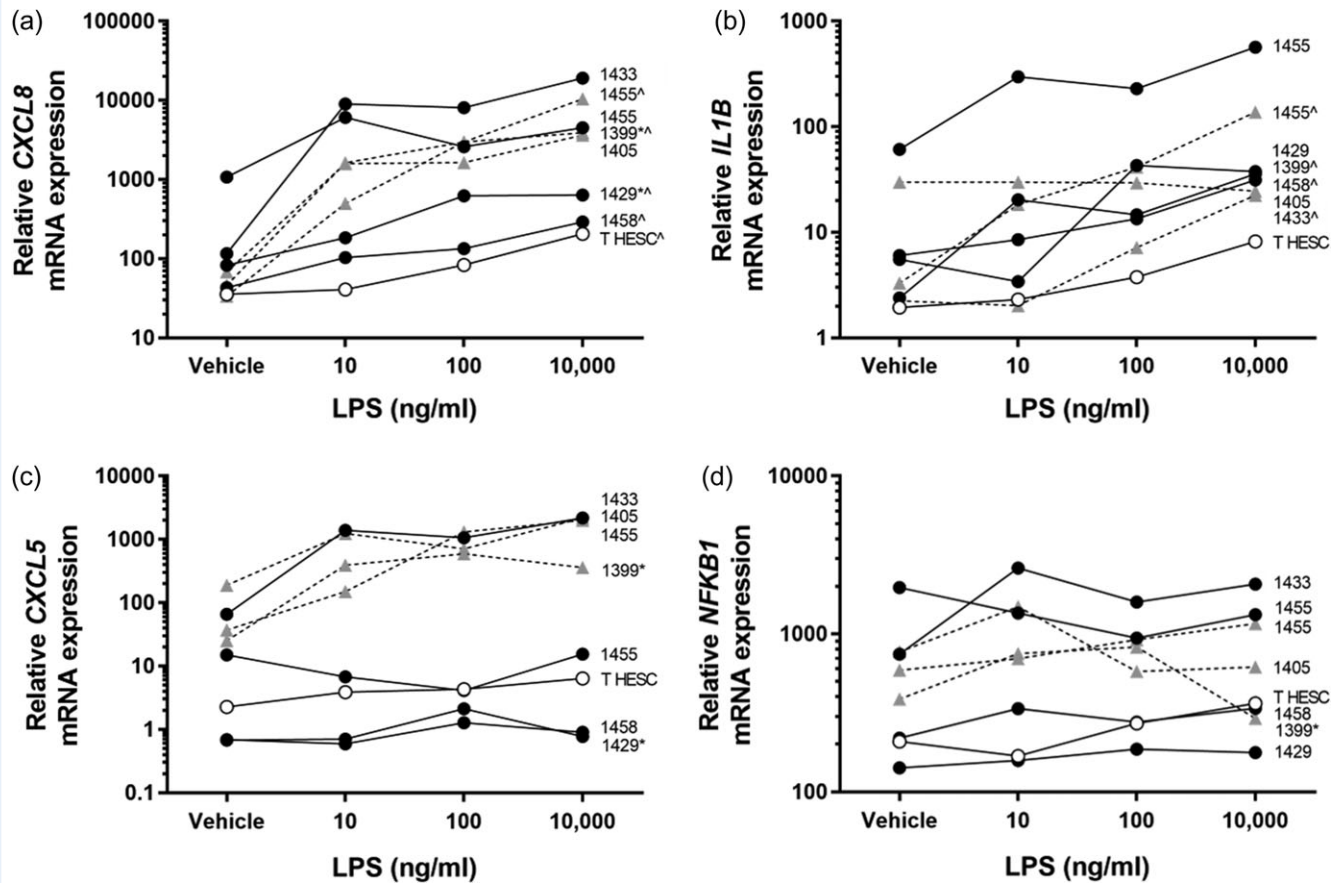
Figure 8 mRNA expression of inflammatory genes *CXCL8, IL1B, CXCL5* and *NFKB1* in hTERT endometrial stromal cultures and T HESC in response to 24 h lipopolysaccharide (LPS) treatment. Closed circles; cells grown in DMEM/12 media, open circles; T HESC and grey triangles; cells grown in M106 media. *Significantly different between vehicle and 100 ng/ml LPS (*P*-value <0.05). ^Significantly different between vehicle and 10 000 ng/ml LPS (*P*-value <0.05).

for five risk SNPs in the 1p36.12 region (including rs12037376 seen in Table II) and was also homozygous RA for 7 out of 14 key SNPs described in Table II (including the *GREB1, VEZT* and 7p15.2 loci); thus, we have generated a hTERT hESC line which is homozygous for multiple different RAs or key SNPs with genome wide significance for endometriosis (Sapkota *et al.*, 2017). While we have demonstrated that *LINC00339* is present in our cell lines, future work is necessary to perform *in vitro* assays comparing RA to OA hESC lines to determine functional cellular differences as a consequence of altered genotype. Furthermore and irrespective of endometriosis genetic risk loci, the genetic diversity displayed amongst the 13 cells lines generated in this study means that cell-based research will more closely reflect the patient to patient variability seen in women with endometriosis.

Endometriosis is an estrogen-dependent disorder and there is also evidence for a role of progesterone-resistance with the disease (Giudice, 2010). Therefore, the ability to appropriately respond to steroid hormones is a desirable feature of the new immortalized cell lines, particularly if they are to be valuable for future gynaecological research. We confirmed that introduction of hTERT had no significant effect on the median expression levels of estrogen and PRs or hormone responsiveness, with cell lines demonstrating a variable ability to

proliferate/regress and decidualise in response to hormonal stimuli. Inflammation is also an inherent response of the human endometrium and is integral to reproductive events including menstruation and implantation. Part of the endometrial stromal cell response to an inflammatory insult includes upregulated transcription of inflammatory response genes (e.g. transcription factors and cytokines). As expected, LPS-exposed hTERT hESC demonstrated a dose-dependent increase in expression of some pro-inflammatory cytokine genes, however, we did not see the expected increase in *NFKB1* (or *RelA* [unpublished data]). More detailed investigation of the NFκB transcription factor cascade (IKK complex, IκB and adaptor proteins like MyD88), and the LPS/TLR4 signal transduction pathway overall, may uncover more components involved in inflammation in our immortalized hESCs. The immortalized hESC lines developed in our laboratory display fundamental hormone- and inflammatory-response characteristics akin to endometrial stromal cells *in vivo*. It is important to highlight the diversity of these responses observed in our cell lines; which reflects normal variability and is a strength of our immortalized stromal cell model.

Others groups have overcome the limitations of primary culture by immortalizing hESC using various methods including simian virus 40 large T antigen (SV40) (Merviel *et al.*, 1995; Chapdelaine *et al.*, 2006;

Tamura *et al.*, 2007; Krishnaswamy *et al.*, 2009) and hTERT (Barbier *et al.*, 2005; Samalecos *et al.*, 2009; Yuhki *et al.*, 2011), including the only commercially available immortalized hESC line (Krikun *et al.*, 2004). We chose to utilize hTERT as our method of immortalization due to a high level of karyotype conservation following hTERT-immortalization compared to SV40 transfections in mammary cells (Toouli *et al.*, 2002). A recent advancement in gene editing, CRISPR/Cas9, has been employed in the cancer and cholesterol streams to specifically manipulate RAs (Coggins *et al.*, 2017; Davis *et al.*, 2018); this approach may provide more sensitive and higher-throughput methods for studying endometriosis risk genotypes in the future. Our cell lines demonstrated variability in the traits we examined including cell proliferation, hormone receptor expression and responsiveness to hormones and inflammation. These variations were highly reflective of normal patient-to-patient variability. With the genotype of each of our cell lines known, we can now commence functional assays and analyses of endometrial stromal cells that possess homozygous-risk or other alleles. Like *in vitro* cultures, rodent models of endometriosis have their limitations, as they do not completely recapitulate the human disease (Bruner-Tran *et al.*, 2018). Moving forward, *in vivo* rodent xenograft models using human immortalized endometrial cells carrying endometriosis risk genoytpes may be important for understanding the complex cooperative roles of genetics and the environment. Importantly, we have shown that the process of immortalization did not alter the SNP genotype of the selected hESC, therefore the endometriosis-risk genotypes were maintained. To the best of our knowledge, we are the first group to generate several hTERT immortalized hESC cell lines with endometriosis risk genotypes reflective of the varied genotypic backgrounds of individual patients.

The priority in the development of these cell lines was to generate a diverse set of hESC lines carrying important endometriosis-RAs. However, their utility goes beyond the setting of endometriosis research and the associated genetic implications, especially given the diversity of the cell lines reproducing true patient-to-patient variability. These immortalized cell lines will be valuable research tools for many different endometrial pathologies (e.g. recurrent miscarriage and implantation failure). In conclusion, our new set of well characterized immortalized hESCs allows us to undertake *in vitro* experimentation with a level of genetic and phenotypic diversity not previously available.

Authors' roles

S.J.H.-C., E.M.C., J.F.D., J.N.F., M.L.C. and P.P. performed the experiments. S.J.H.-C. wrote the article. S.J.H.-C., E.M.C., J.F.D., J.N.F., M.L.C., S.M., P.P., M.H., G.W.M., J.E.G. and P.A.W.R. contributed to the design of the study, analysis and interpretation of the data, drafting of the article and final approval of the version to be published.

Conflict of interest

All authors declare that they have no conflict of interest.

References

Barbier C, Becker K, Troester M, Kaufman D. Expression of exogenous human telomerase in cultures of endometrial stromal cells does not alter their hormone responsiveness. *Biol Reprod* 2005;**73**:106–114.

Bruner-Tran KL, Mokshagundam S, Herington JL, Ding T, Osteen KG. Rodent models of experimental endometriosis: identifying mechanisms of disease and therapeutic targets. *Curr Womens Health Rev* 2018;**14**: 173–188.

Chapdelaine P, Kang J, Boucher Kovalik S, Caron N, Tremblay J, Fortier M. Decidualization and maintenance of a functional prostaglandin system in human endometrial cell lines following transformation with SV40 large T antigen. *Mol Hum Reprod* 2006;**12**:309–319.

Coggins N, Stultz J, O'geen H, Carvajal Carmona L, Segal D. Methods for scarless, selection-free generation of human cells and allele-specific functional analysis of disease-associated SNPs and variants of uncertain significance. *Sci Rep* 2017;**7**:15044.

Davis J, Vadlamudi S, Roman T, Zeynalzadeh M, Iyengar A, Mohlke K. Enhancer deletion and allelic effects define a regulatory molecular mechanism at the VLDLR cholesterol GWAS locus. *Hum Mol Genet* 2018. doi: 10.1093/hmg/ddy385. [Epub ahead of print].

Dimitriadis E, Robb L, Salamonsen LA. Interleukin 11 advances progesterone-induced decidualization of human endometrial stromal cells. *Mol Hum Reprod* 2002;**8**:636–643.

Dimitrov R, Timeva T, Kyurkchiev D, Stamenova M, Shterev A, Kostova P, Zlatkov V, Kehayov I, Kyurkchiev S. Characterization of clonogenic stromal cells isolated from human endometrium. *Reproduction* 2008;**135**: 551–558.

Fung JN, Girling JE, Lukowski SW, Sapkota Y, Wallace L, Holdsworth-Carson SJ, Henders AK, Healey M, Rogers PAW, Powell JE *et al*. The genetic regulation of transcription in human endometrial tissue. *Hum Reprod* 2017;**32**:893–904.

Fung J, Holdsworth-Carson S, Sapkota Y, Zhao Z, Jones L, Girling J, Paiva P, Healey M, Nyholt D, Rogers P *et al*. Functional evaluation of genetic variants associated with endometriosis near GREB1. *Hum Reprod* 2015a; **30**:1263–1275.

Fung JN, Mortlock S, Girling JE, Holdsworth-Carson SJ, Teh WT, Zhu Z, Lukowski SW, Mckinnon BD, Mcrae A, Yang J *et al*. Genetic regulation of disease risk and endometrial gene expression highlights potential target genes for endometriosis and polycystic ovarian syndrome. *Sci Rep* 2018;**8**:11424.

Fung JN, Rogers PA, Montgomery GW. Identifying the biological basis of GWAS hits for endometriosis. *Biol Reprod* 2015b;**92**:87.

Gibson G, Powell JE, Marigorta UM. Expression quantitative trait locus analysis for translational medicine. *Genome Med* 2015;**7**:60.

Giudice LC. Clinical practice. Endometriosis. *N Engl J Med* 2010;**362**: 2389–2398.

Holdsworth-Carson SJ, Fung JN, Luong HT, Sapkota Y, Bowdler LM, Wallace L, Teh WT, Powell JE, Girling JE, Healey M *et al*. Endometrial vezatin and its association with endometriosis risk. *Hum Reprod* 2016; **31**:999–1013.

Kommagani R, Szwarc MM, Vasquez YM, Peavey MC, Mazur EC, Gibbons WE, Lanz RB, Demayo FJ, Lydon JP. The promyelocytic leukemia zinc finger transcription factor is critical for human endometrial stromal cell decidualization. *PLoS Genet* 2016;**12**:e1005937.

Krikun G, Mor G, Alvero A, Guller S, Schatz F, Sapi E, Rahman M, Caze R, Qumsiyeh M, Lockwood CJ. A novel immortalized human endometrial stromal cell line with normal progestational response. *Endocrinology* 2004;**145**:2291–2296.

Krishnaswamy N, Chapdelaine P, Tremblay J, Fortier M. Development and characterization of a simian virus 40 immortalized bovine endometrial stromal cell line. *Endocrinology* 2009;**150**:485–491.

Luong HT, Painter JN, Shakhbazov K, Chapman B, Henders AK, Powell JE, Nyholt DR, Montgomery GW. Fine mapping of variants associated with endometriosis in the WNT4 region on chromosome 1p36. *Int J Mol Epidemiol Genet* 2013;**4**:193–206.

Medicine ASFR. Revised American Society for Reproductive Medicine classification of endometriosis: 1996. *Fertil Steril* 1997;**67**:817–821.

Merviel P, Degeorges A, Salat Baroux J, Calvo F. Normal human endometrial cells in culture: characterization and immortalization of epithelial and stromal cells by SV 40 large T antigen. *Biol Cell* 1995;**84**:187–193.

Powell JE, Fung JN, Shakhbazov K, Sapkota Y, Cloonan N, Hemani G, Hillman KM, Kaufmann S, Luong HT, Bowdler L *et al*. Endometriosis risk alleles at 1p36.12 act through inverse regulation of CDC42 and LINC00339. *Hum Mol Genet* 2016;**25**:5046–5058.

Rashidi N, Mirahmadian M, Jeddi-Tehrani M, Rezania S, Ghasemi J, Kazemnejad S, Mirzadegan E, Vafaei S, Kashanian M, Rasoulzadeh Z *et al*. Lipopolysaccharide- and lipoteichoic acid-mediated pro-inflammatory cytokine production and modulation of TLR2, TLR4 and MyD88 expression in human endometrial cells. *J Reprod Infertil* 2015; **16**:72–81.

Samalecos A, Reimann K, Wittmann S, Schulte H, Brosens J, Bamberger A-M, Gellersen B. Characterization of a novel telomerase-immortalized human endometrial stromal cell line, St-T1b. *Reprod Biol Endocrinol* 2009;**7**:76.

Sampson JA. Heterotopic or misplaced endometrial tissue. *Am J Obstet Gynecol* 1925;**10**:649–664.

Sapkota Y, Steinthorsdottir V, Morris AP, Fassbender A, Rahmioglu N, De Vivo I, Buring JE, Zhang F, Edwards TL, Jones S *et al*. Meta-analysis identifies five novel loci associated with endometriosis highlighting key genes involved in hormone metabolism. *Nat Commun* 2017;**8**: 15539.

Tamura K, Yoshie M, Hara T, Isaka K, Kogo H. Involvement of stathmin in proliferation and differentiation of immortalized human endometrial stromal cells. *J Reprod Dev* 2007;**53**:525–533.

Toouli C, Huschtscha L, Neumann A, Noble J, Colgin L, Hukku B, Reddel R. Comparison of human mammary epithelial cells immortalized by simian virus 40 T-Antigen or by the telomerase catalytic subunit. *Oncogene* 2002;**21**:128–139.

Yuhki M, Kajitani T, Mizuno T, Aoki Y, Maruyama T. Establishment of an immortalized human endometrial stromal cell line with functional responses to ovarian stimuli. *Reprod Biol Endocrinol* 2011;**9**:104.

molecular human reproduction

ORIGINAL ARTICLE

The role of oxygen in regulating microRNAs in control of the placental renin–angiotensin system

Anya L. Arthurs[1,2], Eugenie R. Lumbers[1,2], Sarah J. Delforce [1,2], Andrea Mathe[3], Brian J. Morris[4], and Kirsty G. Pringle [1,2,*]

[1]Priority Research Centre for Reproductive Sciences, School of Biomedical Sciences and Pharmacy, Faculty of Health and Medicine, University of Newcastle, University Drive, Callaghan, New South Wales, 2308, Australia [2]Pregnancy and Reproduction, Hunter Medical Research Institute, Lot 1, Kookaburra Cct, New Lambton Heights NSW 2305, Australia [3]School of Biomedical Sciences and Pharmacy, Faculty of Health and Medicine, University of Newcastle, University Drive, Callaghan, New South Wales, 2308, Australia [4]School of Medical Sciences and Bosch Institute, Anderson Stuart Building, University of Sydney, Camperdown, New South Wales, 2006, Australia

*Correspondence address. Priority Research Centre for Reproductive Sciences, Hunter Medical Research Institute, Level 3 East, 1 Kookaburra Circuit, New Lambton Heights, New South Wales 2305, Australia. Tel: +61-24-042-0372; E-mail: kirsty.pringle@newcastle.edu.au orcid.org/0000-0002-6770-0496

Human placental renin–angiotensin system (RAS) expression is highest in early gestation, at a time when placental oxygen tension is at its lowest (1–3%), and promotes placental development. Some miRNAs predicted to target RAS mRNAs are downregulated in early gestation. We tested the hypothesis that low oxygen suppresses expression of miRNAs that target placental RAS mRNAs, thus increasing concentrations of RAS mRNAs. HTR-8/SVneo cells were cultured in 1, 5 and 20% oxygen for 48 h. Differences in miRNA expression were measured on an Affymetrix miRNA microarray ($n = 3$/group). Those predicted to target RAS mRNAs, or that were decreased in early gestation, were confirmed by qPCR ($n = 9$/group). RAS protein levels were assessed by ELISAs or immuno-blotting. Microarray analysis identified four miRNAs predicted to target RAS mRNAs that were differentially expressed between 1 and 5% oxygen. Using qPCR, 15 miRNAs that target the RAS were measured in HTR-8/SVneo cells. Five miRNAs were downregulated in 1% compared with 5% oxygen. Expression of a number of RAS mRNAs (*ATP6AP2*, *AGT*, *ACE* and *AGTR1*) were increased in either, or both, 1 and 5% oxygen compared with 20% oxygen. AGT protein levels were increased in 1% oxygen compared with 5%. Further validation is needed to confirm that these miRNAs target RAS mRNAs directly and that placental development is partly regulated by oxygen-sensitive miRNAs that target RAS mRNAs. Since placental oxygen tension changes across gestation, changes in expression of these miRNAs may contribute to the transgestational changes in placental RAS expression and the resulting effects on placental development.

Key words: placenta / renin–angiotensin system / miRNA / microarray / oxygen

Introduction

Placentation is a complex developmental process associated with changes in expression of the placental renin–angiotensin system (RAS). The placental RAS contributes to angiogenesis and tissue growth. It could therefore have important physiological effects on the developing placenta (Goyal *et al.*, 2010). In a model of placental insufficiency, the expression of placental RAS genes is significantly altered, i.e. expression of some mRNAs (e.g. AGTR1) is increased, but expression of others (e.g. AGT) is decreased (Goyal *et al.*, 2010). Furthermore, altered expression of RAS components in human placentae is associated with pregnancy complications including intrauterine growth restriction (IUGR) and pre-eclampsia (Nielsen *et al.*, 2000; Ito *et al.*, 2002; Laskowska *et al.*, 2004; Herse *et al.*, 2007, 2008; Goyal *et al.*,

2011). Expression of most of the components of the placental RAS are highest in the first trimester of pregnancy (Pringle *et al.*, 2011), when most of the placental vasculogenesis and cell proliferation is occurring (Cross *et al.*, 1994), and decreases with advancing gestational age. This is postulated to be due to a number of factors, including changes in the prevailing oxygen tension and possibly, changes in post-transcriptional regulation (Rodesch *et al.*, 1992; Gu *et al.*, 2013).

The placenta develops in a very low oxygen environment in the first trimester due to the prevention of maternal blood flow by trophoblastic plugs within the uterine spiral arteries (Coppens *et al.*, 1996). These trophoblastic plugs are dislodged from the spiral arteries, after 12–13 weeks of gestation so that blood can flow into the intervillous space (Jaffe and Woods, 1993). In unviable pregnancies, a very different haemodynamic profile has been observed in early gestation using

Doppler ultrasonography. There is an early onset and increase in the flow of blood into the intervillous space that results in premature increases in oxygen tension, that are detrimental to the growth of the embryo (Jaffe and Warsof, 1992). At the end of the first trimester, i.e. at the end of the embryonic period, continuous blood flow into the placenta is established allowing foetal access to extra oxygen and nutrients to aid further growth and development.

We have found that a low oxygen environment, such as occurs in first trimester placentae, is responsible for the upregulation of angiotensin II type 1 receptor (AT$_1$R) mRNA (*AGTR1*) and angiotensin converting enzyme (ACE) protein levels in a first trimester extravillous trophoblast cell line (Delforce *et al.*, 2016). Other researchers have also shown that maternal hypoxia alters expression of placental RAS components (Goyal *et al.*, 2011) and such changes are associated with IUGR and pre-eclampsia (Genbacev *et al.*, 1996; Regnault *et al.*, 2007; Cuffe *et al.*, 2014).

MicroRNAs (miRNAs) are short, non-coding, single-stranded RNA fragments (~22 nucleotides) that repress the expression levels of specific genes. miRNAs do so by binding to target sequences in the 3′-untranslated region of mRNA transcripts, inducing mRNA degradation when there is high complementary to the sequence or creating a stable, untranslatable miRNA:mRNA complex when binding to a sequence of poor complementarity. In this way, miRNAs can modulate expression of placental RAS genes (Wang *et al.*, 2018). For example, miR-155 causes reduced expression of the angiotensin II type 1 receptor gene (*AGTR1*) by binding to a target sequence in *AGTR1* mRNA (Hromadnikova *et al.*, 2013).

Interestingly, the expression of some miRNAs that are predicted to target placental RAS mRNAs increase with gestational age (Wang *et al.*, 2018) and their expression shows variation between each person (Betoni *et al.*, 2013). In a recent paper from our group, the expression of miR-181a-5p, miR-181a-3p, miR-181c-5p, miR-let-7, miR-34c, miR-454 and miR-625, which have RAS mRNAs as predicted targets,

were examined in placental tissue from early, mid and late gestation (Wang *et al.*, 2018). These miRNAs were shown to be significantly downregulated in early gestation, with highest expression in late gestation. This is consistent with data showing that the mRNA expression of the angiotensinogen gene (*AGT*), *AGTR1*, (pro)renin receptor ((P)RR)/ATPase H$^+$ transporting accessory protein 2 gene (*ATP6AP2*) and (pro)renin gene (*REN*) is highest in early gestation—perhaps because there is downregulation of miRNAs that target the mRNAs of these genes (Pringle *et al.*, 2011).

We postulate that oxygen tension and miRNAs interact to regulate expression of the placental RAS. We propose that a low oxygen environment, such as is present in the first trimester, reduces the expression of miRNAs that target one or more placental RAS mRNAs, causing specific placental RAS genes to be more highly expressed (Fig. 1).

Materials and Methods

Cell culture

HTR-8/SVneo cells (an immortalized first trimester trophoblast cell line provided by Professor Charles Graham, Queens University, Ontario) were cultured at 37°C with 5% CO_2 in air in RPMI-1640 (HyClone) supplemented with 10% v/v heat inactivated FCS (ISAFC Biosciences), 1% w/v L-glutamine and 1 mg/mL Antibiotic-Antimycotic (Gibco). Three separate cultures of HTR-8/SVneo cells were made and from each of these three cultures, three sets of 2×10^5 cells from passages 10–20 were plated (*n* = 9). The culture medium was then replaced and cells were incubated in either standard culture conditions (20% O_2) for proof of concept that miRNA expression is sensitive to low oxygen, or in one of two sealed oxygen chambers (5% or 1% O_2 with 5% CO_2 in N_2) to represent the oxygen tension within the intervillous space during the first and second trimesters, respectively (Rodesch *et al.*, 1992) for a further 48 h, with chambers flushed every 24 h. Cells and culture media were collected into PBS and
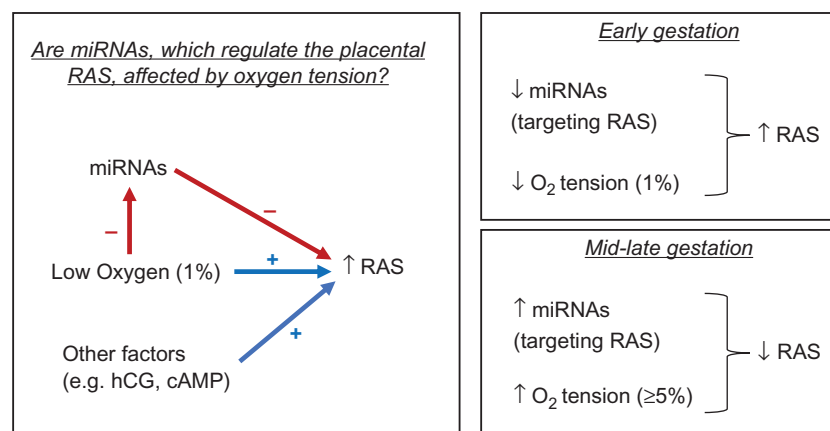
Figure 1 Hypothesis for the study. The left side of the figure shows the overall hypothesis for the study. We hypothesize that low oxygen (1%) will increase expression of the renin angiotensin system (RAS) and suppress the expression of miRNAs that could repress RAS expression. Furthermore, we believe other factors such as hCG and cAMP play a role in regulating RAS expression. Red arrows depict decreased expression, blue arrows depict increased expression. The right side of the figure shows our extended hypotheses; that is, in early gestation, when the oxygen tension is low (1%), miRNAs targeting the RAS are reduced and overall RAS expression is increased. Furthermore, in mid to late gestation, when oxygen tension in the placenta is increased (≥ 5%), there is increased expression of miRNAs targeting the RAS and overall RAS expression in reduced.

snap frozen in liquid nitrogen, then stored at −80°C before RNA analysis. These procedures were repeated to collect cells used for protein analysis.

RNA extraction and DNAse treatment

Total RNA extraction of HTR-8/SVneo cells was performed using the miRNeasy kit, according to the manufacturer's instructions (*Qiagen*). The integrity of total RNA and miRNAs was examined by gel electrophoresis and quantified using the Nanodrop 2000 (data not shown). Samples were used for further analysis if the 260:280 and 260:230 nm ratios were greater than 1.8.

Microarray analysis

Total RNA (in a final concentration of 50–100 ng/μL) was provided to the Ramaciotti Centre at the University of New South Wales, Sydney for Affymetrix miRNA microarray analysis. RNA quality was analysed using a Bioanalyser (Agilent) before microarray analysis at the Ramaciotti Centre. Labelling and hybridization to an Affymetrix Human miRNA microarray, which supports the detection of 2006 human miRNAs, was performed. miRNA microarray analysis was undertaken on $n = 3$ samples cultured in separate experiments at each of the three different oxygen tensions (1, 5 and 20%). All samples in the microarray occupied a single microarray slide. Data produced by microarray analysis were analysed using Partek Genomic Suite software.

miRNA analysis

Fifteen miRNAs predicted to target RAS mRNAs were assessed by qPCR for their expression at 1, 5 and 20% oxygen tension. RNA samples underwent reverse transcription to cDNA (TaqMan® miRNA Reverse Transcription Kit and RT-qPCR probes) and were analysed by quantitative PCR (RT-qPCR) using TaqMan® Universal PCR master mix, according to

Table I mRNA primer sequences

Official gene symbol	GenBank Accession #	Primer Sequence (5′–3′)	Concentration	Melt temperature (°C)
ACTB	NM_001101	Fw: CGCGAGAAGATGACCCAGAT	1000 nM	78
		Rv: GAGTCCATCACGATGCCAGT		
ACE	NM_000789	Fw: AAGCAGGACGGCTTCACAGA	200 nM	85
		Rv: GGGTCCCCTGAGGTTGATGTAT		
AGT	NM_000029	Fw: CAACACCTACGTCCACTTCCAA	200 nM	62
		Rv: TGTTGTCCACCCAGAACTCCT		
AGTR1	NM_000685	Fw: CCTCAGATAATGTAAGCTCATCCAC	200 nM	77
		Rv: GCTGCAGAGGAATGTTCTCTT		
ATP6AP2	NM_005765	Fw: CCTCATTAGGAAGACAAGGACTATCC	200 nM	60
		Rv: GGGTTCTTCGCTTGTTTTGC		

Fw: Forward; Rv: Reverse

Table II miRNA primer sequences

miRNA name	Mature miRNA sequence	TaqMan assay ID
Hsa-miR-181a-3p	ACCAUCGACCGUUGAUUGUACC	000516
Hsa-miR-181a-5p	AACAUUCAACGCUGUCGGUGAGU	000480
Hsa-miR-181c-5p	AACAUUCAACCUGUCGGUGAGU	000482
Hsa-miR-34c-5p	AGGCAGUGUAGUUAGCUGAUUGC	000428
Hsa-miR-7-5p	UGGAAGACUAGUGAUUUUGUUGUU	005723_mat
Hsa-miR-625-5p	AGGGGGAAAGUUCUAUAGUCC	002431
Hsa-miR-454-3p	UAGUGCAAUAUUGCUUAUAGGGU	002323
Hsa-miR-143-3p	UGAGAUGAAGCACUGUAGCUC	002249
Hsa-miR-155	UUAAUGCUAAUCGUGAUAGGGGU	002287
Hsa-miR-514b	AUUGACACCUCUGUGAGUGGA	242955_mat
Hsa-miR-330	UCUCUGGGCCUGUGUCUUAGGC	002230
Hsa-miR-892a	CACUGUGUCCUUUCUGCGUAG	002195
Hsa-miR-378g	ACUGGGCUUGGAGUCAGAAG	462874_mat
Hsa-miR-483-3p	UCACUCCUCUCCUCCCCGUCUU	002339
Hsa-miR-663	GGUGGCCCGGCCGUGCCUGAGG	002857
RNU44	CCTGGATGATGATAGCAAATGCTGACTGAA	001094
	CATGAAGGTCTTAATTAGCTCTAACTGACT	
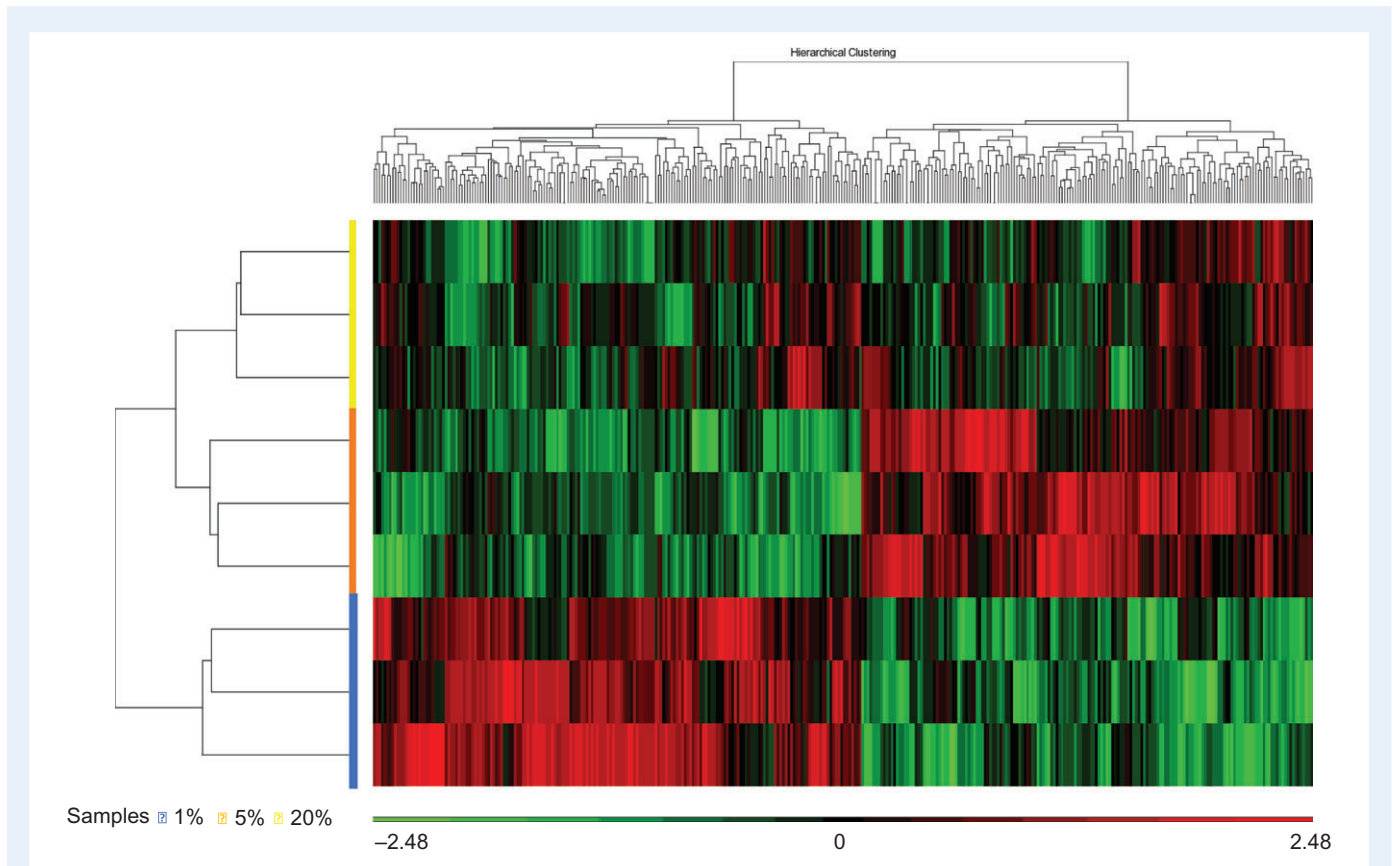
Figure 2 Unsupervised hierarchical clustering of miRNAs differentially expressed in 1, 5 and 20% oxygen tensions. This figure depicts the miRNA microarray data through unsupervised hierarchical clustering. $N = 3$ samples per oxygen tension. The coloured bar to the left of the graph indicates the group to which each sample belongs. 1% Oxygen is shown in blue, 5% oxygen is shown in orange and 20% oxygen is shown in yellow.

the manufacturer's instructions (Applied Biosystems). A list of primer sequences used can be found in Tables I and II.

Semi-quantitative reverse transcriptase polymerase chain reaction

All RNA samples ($n = 9$) underwent reverse transcription to cDNA (Superscript III First-Strand Synthesis for RT, using the manufacturer's instructions, *Thermo Fisher Scientific*). Total RNA was spiked with a known amount of Alien RNA (Stratagene), consisting of total RNA. qPCR was performed in an Applied Biosystems 7500 Real Time PCR System using SYBR Green for detection. Each reaction mixture contained 5 µL of SYBR Green PCR master mix (Applied Biosystems), RAS primers, cDNA reversed transcribed from 10 ng total RNA, and water to 10 µL. Messenger RNA abundance was calculated as described previously, using the $2^{-\Delta\Delta CT}$ method and expressed relative to *ACTB* mRNA and a calibrator (a term placental sample collected at elective Caesarean section) (Pringle *et al.*, 2011).

Protein extraction

Total protein was extracted from HTR-8/SVneo cells using a radioimmunoprecipitation assay (RIPA) lysis and extraction buffer directly from the cell culture well. RIPA buffer (500 µL of 50 mM Tris–HCl, 150 mM NaCl, 1 mM EDTA, 1% v/v NP-40, 0.5% w/v sodium deoxycholate, 100 nM sodium orthovanadate), Complete Mini Protease Inhibitor Cocktail tablets

(Roche Diagnostics Australia) and 5 µL of 100 nM PMSF were added to each sample. Samples were incubated on ice for 10 min, vortexed and then centrifuged at 16 200 g at 4°C for 10 min. Supernatants were collected. Protein was quantified using the Pierce BCA Protein assay kit (Life Technologies) according to the manufacturer's instructions.

Western blotting

Western Blotting was performed as described previously (Wang *et al.*, 2018). Briefly, samples were loaded into Bis-Tris methane 4–12% gels in duplicate before electrophoresis. Proteins were then transferred to a polyvinylidene difluoride (PVDF) membrane using the wet sandwich method immersed in a transfer buffer. The PVDF membrane was then completely dried and re-activated before immunodetection. The membrane was rocked in a blocking solution (5% w/v BSA, 5% w/v skim milk in tris buffered saline (TBS)) overnight at 4°C. The primary antibody solution was then added (1:1000 dilution for both, the antibodies being Abcam #ab40790 for (P)RR and Abcam #ab124734 for AGTR1) and samples were incubated at 22°C on a rocker ((P)RR for 2 h and AGTR1 for 4 h). The secondary anti-rabbit antibody solution was added (Millipore, Burlington, MA, USA; #12-348, 1:5000) and incubated at 22°C on a rocker for 1 h. Membranes were rinsed before signal detection using an Amersham ECL detection kit (GE Healthcare Life Science) and Amersham Imager 600. Membranes were then stripped using 0.2 M NaOH and, using a rabbit polyclonal anti-β-actin antibody (Abcam;
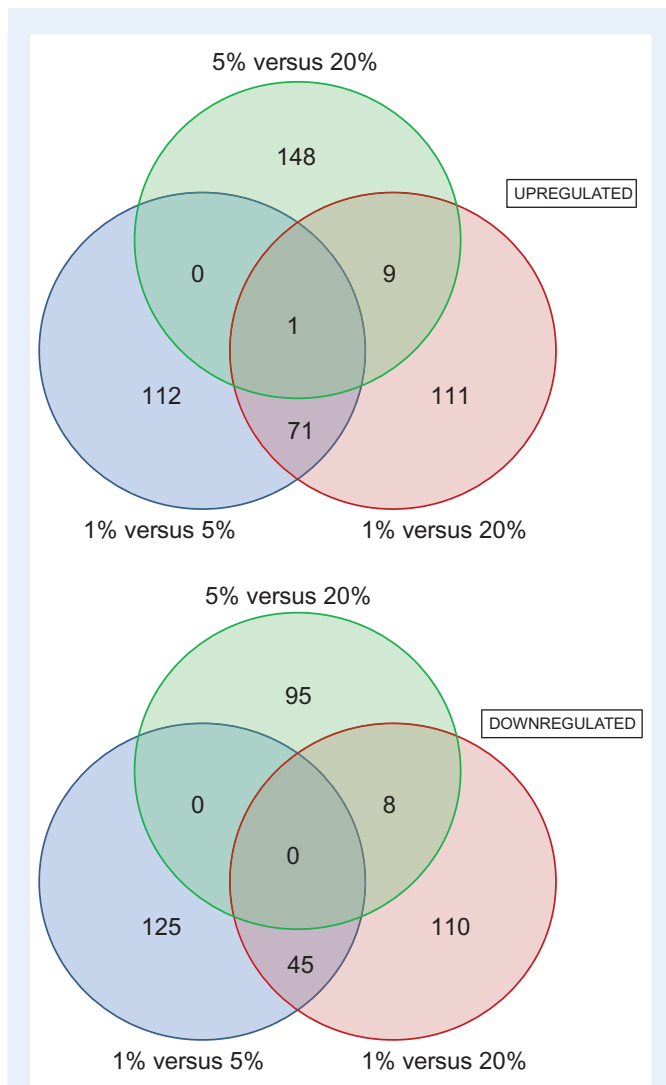
Figure 3 Venn diagram depicting miRNAs upregulated and downregulated between 5% and 20% oxygen, between 1 and 5% oxygen, and between 1 and 20% oxygen. The top diagram shows miRNAs upregulated between the oxygen tensions. The bottom diagram shows miRNAs downregulated between the oxygen tensions. The green circle (above) depicts miRNAs shown in the microarray to be altered between 5 and 20% oxygen tensions. The blue circle (left) depicts miRNAs shown in the microarray to be altered between 1 and 5% oxygen tensions. The red circle (right) depicts miRNAs shown in the microarray to be altered between 1 and 20% oxygen tensions. The intersection of the three circles indicates miRNAs that are altered in 5 versus 20% oxygen, 1 versus 20% oxygen, and in 1 versus 5% oxygen.

ab8227, 1:5000), were used to detect β-actin for normalization. The ratio of the protein of interest to β-actin was averaged for duplicate lanes and differences between blots were corrected using an internal control (a pooled placental sample).

Enzyme-linked immunosorbent assays

Commercially available enzyme-linked immunosorbent assays (ELISAs) were used to measure concentrations of prorenin (Molecular Innovations,

MI, USA), angiotensinogen (IBL International, Hamburg, Germany) and ACE (Duoset, R&D systems, MN, USA) using methods described previously (Pringle *et al.*, 2015).

Statistics

Statistical analysis was undertaken using GraphPad Prism 7. A one-way ANOVA (non-parametric) test was conducted using Tukey's multiple comparisons test. Differences between groups were considered significant for $P \leq 0.05$.

Partek Genomic Suite software was used to analyse microarray data. A robust multi-array analysis (RMA) was performed, including $\log_2$ transformation, background corrections, quantile normalization and summarization of probe features, which produced a set of expression signal intensities. To identify differences in expression of miRNAs at different oxygen tensions, unsupervised hierarchical clustering was conducted between the treatment groups. Correction for multiple testing was performed using the Benjamini–Hochberg method, with a default false discovery rate (Benjamini and Hochberg, 1995). Particular attention was paid to those miRNAs predicted to target RAS mRNAs (as described on miRNA predictors mirbase.org, mirdb.org, targetscan.org and targetexplorer.ingenuity.com) with 90% complementarity or higher.

Results

miRNA microarrays of HTR-8/SVneo cells cultured in 1, 5 and 20% O_2

Comparison of the expression of miRNAs in HTR-8/SVneo cells cultured in 1 versus 20% O_2 showed significant differences in the expression of 355 miRNAs (GEO submission GSE121593) (PCA analysis can be found in Supplementary Fig. S1, and unsupervised hierarchical clustering is shown in Fig. 2). In 1% O_2, the expression of 192 miRNAs was increased and 163 miRNAs was decreased compared with cells cultured in 20% O_2 (Fig. 3). This included miR-210-3p, known to be regulated by hypoxia (termed a hypoximiR), which was increased by 7.6-fold in 1% O_2 compared with 20% O_2 ($P = 6.5E–08$). Of those that were differentially expressed, six miRNAs were predicted to target RAS mRNAs, with two being increased and four being decreased compared with 20% O_2 (Table III).

Comparison of the expression of miRNAs in HTR-8/SVneo cells cultured in 1 versus 5% O_2 showed significant differences in the expression of 354 miRNAs (GEO submission GSE121593). Compared with cells cultured in 5% O_2, cells grown in 1% O_2 showed increased expression of 184 miRNAs and decreased expression of 170 miRNAs (Fig. 3). One of these, the hypoximiR, miR-210-3p, was increased by 2.6-fold in 1% O_2 compared with 5% O_2 ($P = 6.0E–06$). Of those that were differentially expressed between 1 and 5% oxygen, four were predicted to target RAS mRNAs (Table IV), of which three were downregulated in 1% oxygen compared with expression in 5% O_2.

Comparison of the expression of miRNAs in HTR-8/SVneo cells cultured in 5 versus 20% O_2 showed significant differences in the expression of 261 miRNAs (GEO submission GSE121593). In 5% O_2, 158 miRNAs had increased expression and 103 miRNAs had decreased expression compared with cells cultured in 20% O_2 (Fig. 3). The hypoximiR, miR-210-3p, was increased by 3-fold in 5% O_2 compared with 20% O_2 ($P = 2.7 E–06$). Furthermore, 8 of these miRNAs were predicted to target RAS mRNAs (Table V).

Table III Microarray levels of miRNAs, that are predicted to target renin–angiotensin system mRNAs, in 1% compared with 20% oxygen tension

Transcript ID (array design)	Target RAS mRNA	P-value (1% versus 20%)	Fold-change (1 versus 20%)
Hsa-miR-625-5p	ATP6AP2	3.3E–04	1.8
Hsa-miR-892b	AGT	4.9E–02	1.3
Hsa-miR-155-5p	AGTR1	4.3E–02	−1.2
Hsa-miR-34b-5p	AGTR1	3.5E–02	−1.3
Hsa-miR-181a-5p	REN, ACE	1.1E–03	−1.5
Hsa-miR-454-3p	ATP6AP2	3.1E–02	−1.7

Table IV Microarray levels of miRNAs, that are predicted to target renin–angiotensin system mRNAs, in 1% compared with 5% oxygen tension.

Transcript ID (array design)	Target RAS mRNA	P-value (1 versus 5%)	Fold-change (1 versus 5%)
hsa-miR-514a-3p	AGT, AGTR1	4.7E–02	1.16
hsa-miR-330-3p	REN	4.7E–03	−1.26
hsa-miR-625-5p	ATP6AP2	5.3E–03	−1.39
hsa-miR-181a-5p	REN, ACE	2.9E–03	−1.41

Table V Microarray levels of miRNAs, that are predicted to target renin–angiotensin system mRNAs, in 5% compared with 20% oxygen tension.

Transcript ID (array design)	Target RAS mRNA	P-value (5 versus 20%)	Fold-change (5 versus 20%)
Hsa-miR-330-3p	REN	4.2E–02	−1.27
Hsa-miR-625-5p	ATP6AP2	2.2E–02	−1.27
Hsa-miR-514a	AGT, AGTR1	1.6E–02	−1.27
Hsa-miR-378c	REN, ACE	1.5E–02	−1.38
Hsa-miR-892b	AGT	1.2E–02	−1.42
Hsa-miR-378i	REN, ACE	7.5E–03	−1.47
Hsa-miR-378a-3p	REN, ACE	1.5E–02	−1.49
Hsa-miR-454-3p	ATP6AP2	4.9E–03	−2.30

Effect of O_2 on expression of miRNAs that target the RAS in HTR-8/SVneo cells

At all oxygen tensions, the HTR-8/SVneo cells expressed miRNAs predicted to target RAS mRNAs. These miRNAs were hsa-miR-34c-5p, hsa-miR-454-3p, hsa-miR-514b, hsa-miR-330, hsa-miR-892a, hsa-miR-378g, hsa-miR-181a-5p, hsa-miR-181a-3p, hsa-miR-483-3p, hsa-miR-663b, hsa-miR-181c-5p, hsa-miR-7-5p, hsa-miR-143-3p, hsa-miR-625-5p and hsa-miR-155.

The expression of miRNAs shown to be significantly altered by oxygen tension in the microarray analysis, and predicted to target RAS mRNAs, was confirmed using qPCR. qPCR showed that the following miRNAs were significantly reduced in 1% O_2 compared with cells cultured in 20% O_2 for 48 h: hsa-miR-34c-5p (P = 0.03; Fig. 4A), hsa-miR-454-3p (P = 0.04; Fig. 4B),

hsa-miR-514b (P = 0.002; Fig. 4C), hsa-miR-330 (P = 0.034; Fig. 4D), hsa-miR-892a (P = 0.02; Fig. 4E), hsa-miR-378g (P = 0.02; Fig. 4F), and hsa-miR-181a-5p (P = 0.043; Fig. 4G). Table VI summarizes these results.

Additionally, the expression of hsa-miR-34c-5p (P = 0.03; Fig. 4A), hsa-miR-454-3p (P = 0.03; Fig. 4B), hsa-miR-514b (P = 0.02; Fig. 4C) and hsa-miR-378g (P = 0.002; Fig. 4F) was significantly reduced in cells cultured in 1% O_2 compared with cells cultured in 5% O_2 (see also Table VII). Expression of hsa-miR-892a was downregulated in cells cultured in 5% O_2 compared with cells cultured at 20% O_2 (P = 0.004; Fig. 4E).

Hsa-miR-625-5p and hsa-miR-155, which are predicted to target ATP6AP2 and AGTR1 mRNAs, respectively, were expressed in HTR-8/SVneo cells, but their expression was not affected by oxygen tension (data not shown).
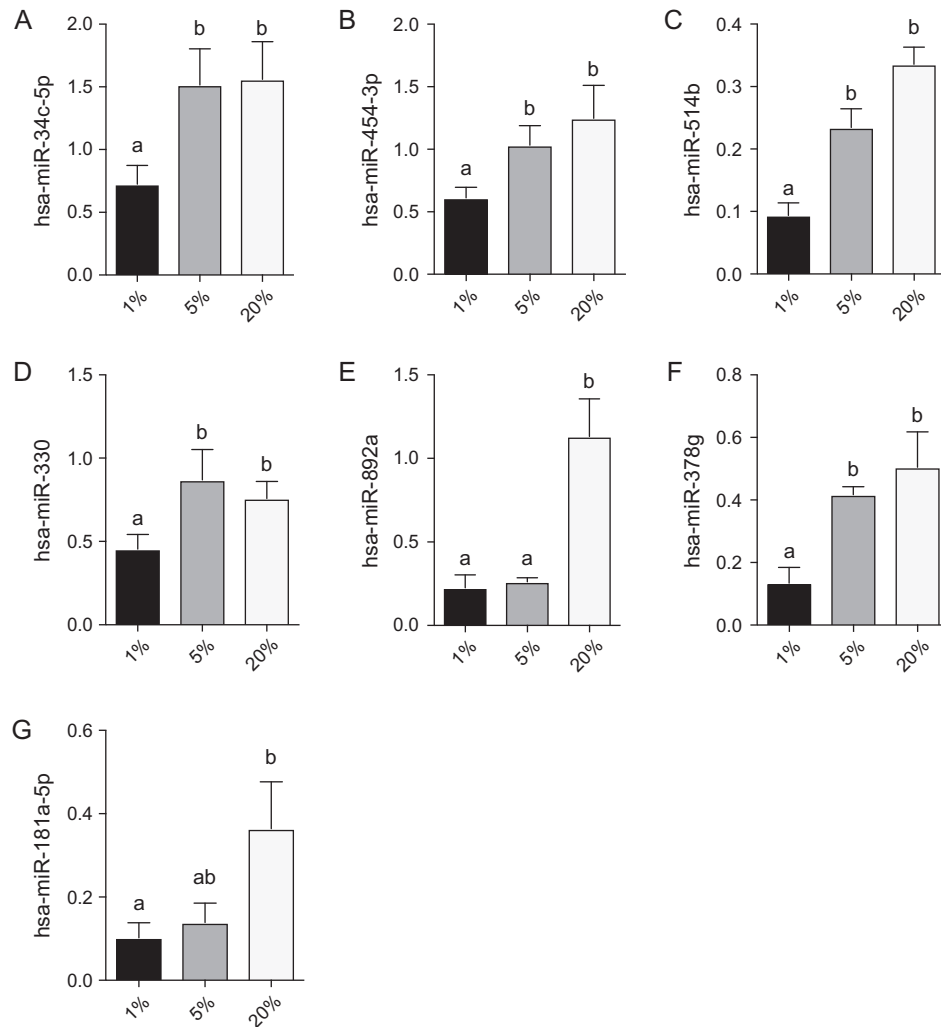
Figure 4 Oxygen regulates the expression of placental miRNAs (that were also altered in the microarrays) that are predicted to target RAS mRNAs. Levels of (**A**) miR-34c-5p, (**B**) miR-454-3p, (**C**) miR-514b, (**D**) miR-330, (**E**) miR-892a, (**F**) miR-378g and (**G**) miR-181a-5p are significantly downregulated in HTR-8/SVneo cells cultured in 1% O_2 compared with those cultured in 20% O_2. Relative abundance is presented as mean ± SEM. $N = 3$ experiments, each in triplicate. The same letter above each bar indicates that groups are not different from each other. A different letter above the bar indicates that the groups are different from each other (all $P < 0.05$).

The expression of a number of other miRNAs predicted to target RAS mRNAs, but that did not show oxygen dependent expression on the microarray, were previously shown to be decreased in first trimester compared with term placentae (Wang *et al.*, 2018). These were also examined using qPCR. This showed that hsa-miR-181a-3p ($P = 0.03$; Fig. 5A), hsa-miR-483-3p ($P = 0.01$; Fig. 5B) and hsa-miR-663b ($P = 0.01$; Fig. 5C) were in fact significantly downregulated in cells incubated in 1% O_2 compared with 20% O_2.

Expression of hsa-miR-483-3p ($P = 0.01$; Fig. 5B) was also significantly decreased in 1% O_2 when compared with cells cultured in 5% O_2, and expression of hsa-miR-663b ($P = 0.02$; Fig. 5C) was decreased in 5% O_2 samples compared with 20% O_2 samples.

Hsa-miR-181c-5p, hsa-miR-7-5p and hsa-miR-143-3p were detected in all samples but no differences in the expression of these miRNAs in cells cultured at different oxygen tensions were detected using qPCR (data not shown).

Effect of O_2 on RAS mRNA and protein expression in HTR-8/SVneo cells

At all oxygen tensions, HTR-8/SVneo cells expressed *REN*, *ACE*, *AGT*, *AGTR1* and *ATP6AP2* mRNAs.

Levels of *REN* and *AGT* mRNAs were not significantly different in cells cultured in 1 and 20% O_2 ($P > 0.05$; respectively Fig. 6A and F), although levels of *AGT* mRNA were significantly upregulated in 5% O_2 compared with 20% O_2 ($P = 0.009$).

Levels of prorenin protein were significantly increased in the cell culture supernatant, and decreased in cell lysate in 1% O_2 compared with 20% O_2 ($P = 0.009$, $P = 0.017$, respectively; Fig. 6B and C), but expression of total prorenin protein (inclusive of protein in both the cell lysate and supernatant) was increased in cells cultured in 1% O_2 compared with 20% O_2 ($P = 0.017$; Fig. 7A). Expression of AGT protein was significantly increased in supernatant and in cell lysate ($P <$

Table VI Summary of changes in the levels of selected miRNAs and predicted target mRNAs and proteins of the renin–angiotensin system in 1% oxygen tension compared with 20% oxygen tension.

miRNA name	Effects of low oxygen (measured by microarray)	Effects of low oxygen (measured by qPCR	Target RAS genes	Effects of low oxygen on target mRNA	Effects of low oxygen on target protein
hsa-miR-34 (34c-5p/34b-5p)	↓	↓	*AGTR1*	↑	–
hsa-miR-454-3p	↓	↓	*ATP6AP2*	↑	–
hsa-miR-514 (514a-3p/514b)	–	↓	*AGT*	–	↑
			AGTR1	↑	–
hsa-miR-330-3p	–	↓	*REN*	–	↑
hsa-miR-892 (892a/892b)	↑	↓	*AGT*	–	↑
hsa-miR-378 (378a/378c/378i)	–	↓	*REN*	–	↑
			ACE	↑	↑
hsa-miR-181a-5p	↓	↓	*REN*	–	↑
			ACE	↑	↑
hsa-miR-181a-3p	–	↓	*REN*	–	↑
hsa-miR-483-3p	–	↓	*ACE*	↑	↑
			ACE2	Not measured	Not measured
			AGT	–	↑
			AGTR1	↑	–
hsa-miR-663b	–	↓	*REN*	–	↑
hsa-miR-181c-5p	–	–	*AGT*	–	↑
hsa-miR-7-5p	–	–	*AGTR1*	↑	–
hsa-miR-143-3p	–	–	*ACE2*	Not measured	Not measured
hsa-miR-625-5p	↑	–	*ATP6AP2*	↑	–
hsa-miR-155-5p	↓	–	*AGTR1*	↑	–

↑ indicates upregulation, ↓ indicates downregulation, – indicates no change.

0.001, $P = 0.001$, respectively; Fig. 6G and H) in 1% compared to 20% O_2. Expression of AGT protein in supernatant and cell lysate was also significantly increased in 5% O_2 when compared with 20% oxygen ($P = 0.002$ and $P = 0.041$, respectively) and in 1% O_2 when compared with 5% O_2 in cell lysate ($P = 0.034$).

Expression of *ACE, AGTR1* and *ATP6AP2* mRNAs were significantly increased by culture in 1% O_2, ($P < 0.001$, $P = 0.03$ and $P = 0.001$; respectively, Fig. 6I, L and D) and 5% O_2 ($P = 0.002$, $P = 0.001$ and $P < 0.001$; respectively) compared with cells cultured in 20% O_2 for 48 h. Expression of *ACE* mRNA was also significantly increased in low oxygen (1%; $P = 0.008$; Fig. 6I) compared with cells cultured in 5% O_2. Expression of *ATP6AP2* mRNA was also significantly increased in 5% oxygen compared with 20% oxygen ($P = 0.03$; Fig. 6D).

ACE protein was significantly increased in both cell culture supernatant and cell lysate in 1% O_2 compared with 20% O_2 ($P < 0.001$, $P = 0.032$, respectively; Fig. 6J and K).

Concentrations of AGTR1 and (P)RR proteins were not significantly different between cells cultured in 1 and 20% O_2 ($P > 0.05$; respectively Fig. 6M and E).

For simplicity, a summary of the differences in protein levels between 1 and 20% and between 1 and 5% oxygen tensions are presented in Tables VI and VII, respectively.

Discussion

We have found that the prevailing oxygen tension affects the expression of miRNAs in a human first trimester placental trophoblast cell line (HTR-8/SVneo). Results from our microarrays showed that the expression of 374 miRNAs were significantly different in cells incubated in 1% O_2 compared with cells incubated in 20% O_2. Of these, nine miRNAs have been predicted to target the RAS and the oxygen-dependent changes in their expression was established by PCR. A further six miRNAs predicted to target the RAS, that were not significantly altered on the microarray, but that are decreased in first trimester placentae (Wang *et al.*, 2018), were examined and three were shown to have decreased expression in 1% O_2 when samples were tested by RT-qPCR.

Interestingly, we found discrepancies in the expression of miRNAs upon attempting to validate the microarray results. This may have been due to the limited number of samples per oxygen tension ($n = 3$) used for the microarray analysis, whilst a larger number of samples ($n = 9$) were used for qPCR, and so non-significant results from the microarray may in fact be false negatives. It is, moreover, well known that qPCR is a more sensitive method for detecting differences in miRNA expression than microarrays (Wang *et al.*, 2006), and we have used the microarray data as an initial indicator for miRNAs that may

Table VII Summary of changes in the levels of selected miRNAs and predicted target mRNAs and proteins of the renin–angiotensin system in 1% oxygen tension compared with 5% oxygen tension.

miRNA name	Effects of low oxygen (measured by microarray)	Effects of low oxygen (measured by qPCR)	Target RAS genes	Effects of low oxygen on target mRNA	Effects of low oxygen on target protein
hsa-miR-34 (34c-5p/34b-5p)	–	↓	AGTR1	–	–
hsa-miR-454-3p	–	↓	ATP6AP2	–	–
hsa-miR-514 (514a-3p/514b)	↑	↓	AGT	↓	↑
			AGTR1	–	–
hsa-miR-330-3p	↓	↓	REN	–	–
hsa-miR-892 (892a/892b)	–	–	AGT	↓	↑
hsa-miR-378 (378a/378c/378i)	–	↓	REN	–	–
			ACE	↑	–
hsa-miR-181a-5p	↓	–	REN	–	–
			ACE	↑	–
hsa-miR-181a-3p	–	–	REN	–	–
hsa-miR-483-3p	–	↓	ACE	↑	–
			ACE2	Not measured	Not measured
			AGT	↓	↑
			AGTR1	–	–
hsa-miR-663b	–	–	REN	–	–
hsa-miR-181c-5p	–	–	AGT	↓	↑
hsa-miR-7-5p	–	–	AGTR1	–	–
hsa-miR-143-3p	–	–	ACE2	Not measured	Not measured
hsa-miR-625-5p	↓	–	ATP6AP2	–	–
hsa-miR-155-5p	–	–	AGTR1	–	–

↑ indicates upregulation, ↓ indicates downregulation, – indicates no change.

Figure 5 **Oxygen regulates the expression of placental miRNAs (that were not shown to be differentially expression in the microarrays) that are predicted to target renin angiotensin system (RAS) mRNAs.** Levels of A miR-181a-3p, B miR-483-3p, and J miR-663b are significantly downregulated in HTR-8/SVneo cells cultured in 1% O_2 compared with those cultured in 20% O_2. Relative abundance is presented as mean ± SEM. $N = 3$ experiments, each in triplicate. The same letter above each bar indicates that groups are not different from each other. A different letter above the bar indicates that the groups are different from each other (all $P < 0.05$).

be of value for further study. For ease of interpretation of our results, Tables VI (comparing 1 and 20% oxygen tensions) and VII (comparing 1 and 5% oxygen tensions) summarize the miRNAs studied, their expressions in the microarray and qPCR data, their predicted RAS mRNA targets, and the targets' mRNA and protein expressions. We hypothesized that a lower oxygen tension would repress expression of miRNAs that target the RAS, allowing higher expression of RAS mRNA and protein (Fig. 1); this is consistent with results shown in Table VI.
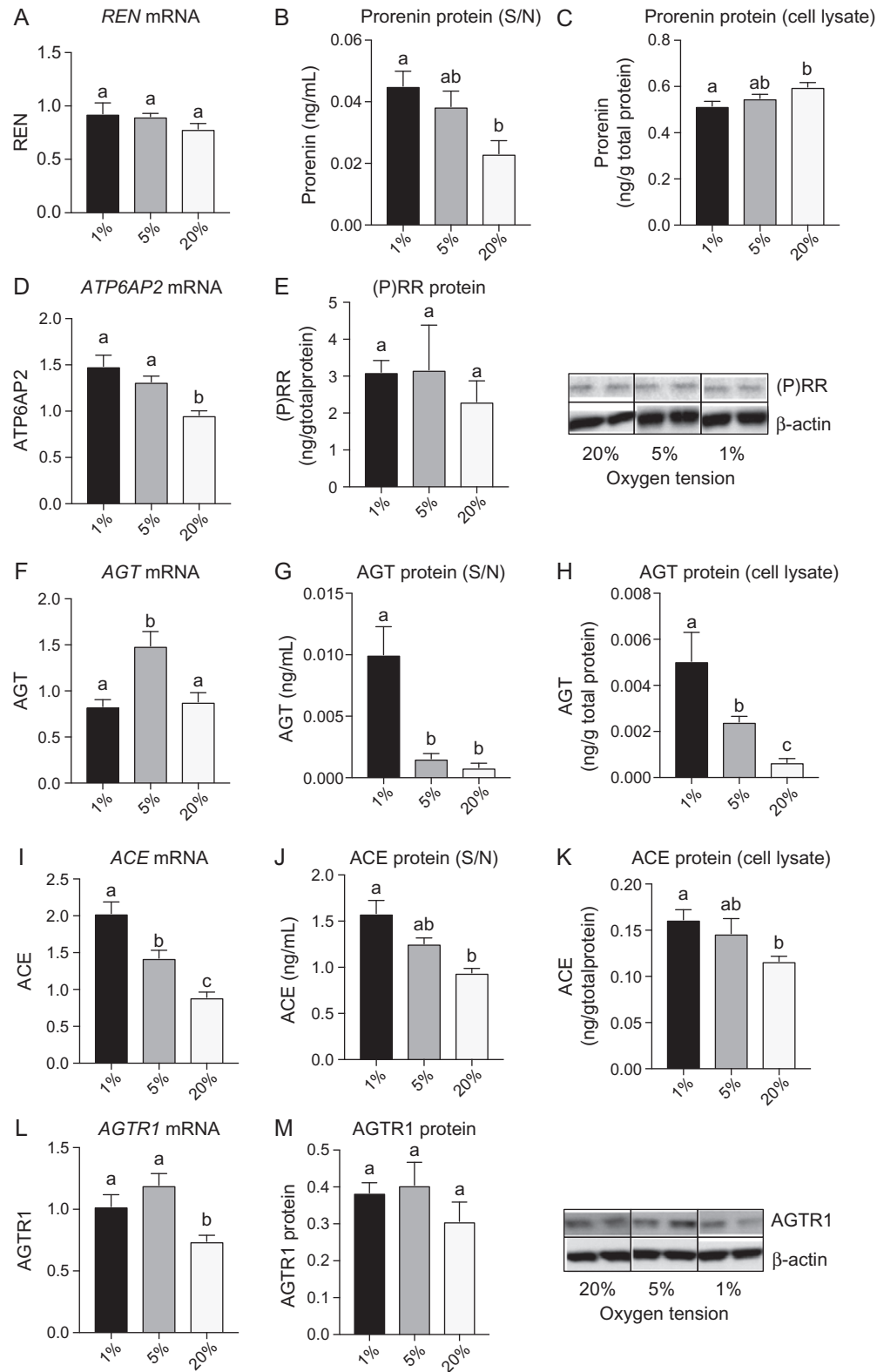
Figure 6 Oxygen regulates the expression of placental renin angiotensin system (RAS) RNAs and proteins. Levels of (**A**) REN mRNA, (**B**) prorenin protein in supernatant (S/N), (**C**) prorenin protein in cell lysate, (**D**) ATP6AP2 mRNA, (**E**) (P)RR protein, (**F**) AGT mRNA, (**G**) AGT protein in supernatant, (**H**) AGT protein in cell lysate, (**I**) ACE mRNA, (**J**) ACE protein in supernatant, (**K**) ACE protein in cell lysate, (**L**) AGTR1 mRNA, (**M**) AGTR1 protein; in HTR-8/SVneo cells cultured in 1% O_2 and 5% O_2 compared with those cultured in 20% O_2. Relative abundance is presented as mean ± SEM. $N = 3$ experiments, each in triplicate. The same letter above each bar indicates that groups are not different from each other. A different letter above the bar indicates that the groups are different from each other (all $P < 0.05$)
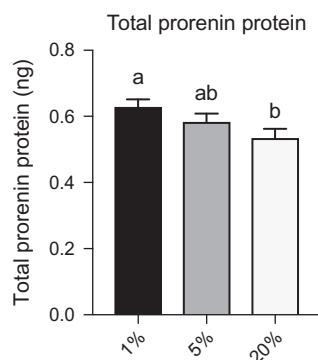
Figure 7 Oxygen regulates the expression of total prorenin protein. Expression of total prorenin protein; in HTR-8/SVneo cells cultured in 1% O_2 was significantly higher than those cultured in 20% O_2. Relative abundance is presented as mean $\pm$ SEM. $N = 3$ experiments, each in triplicate. The same letter above each bar indicates that groups are not different from each other. A different letter above the bar indicates that the groups are different from each other (all $P < 0.05$).

It should be noted that for some miRNAs (miR-34, miR-514, miR-892 and miR-378) an alternative isoform of the miRNA was used for the qPCR analysis to what was detected on the microarray, due to the availability of primers. However, all isoforms are less than two nucleotide bases different from each other. As miRNAs are able to bind with various degrees of complementarity, we do not believe the isoforms chosen differ in their mRNA target binding, nor would the expression of the alternate miRNA isoform differ from the isoform measured on the microarray.

As mentioned in the Methods section, comparing between 1 and 20% oxygen tensions allowed proof of concept that oxygen was responsible for the regulation of miRNA expression. However, with regards to placental physiology, only 1% (7.6 mmHg) and 5% (38 mmHg) oxygen tensions are physiologically relevant, as they reflect the oxygen tensions in the chorionic villi in the first and second trimesters (Rodesch *et al.*, 1992), respectively. Interestingly, as shown in Fig. 2, miRNA expression in 5% oxygen was more similar to that seen in 20% oxygen than it was to the expression of miRNAs in 1% oxygen, suggesting that the use of 20% oxygen tension is not completely irrelevant and perhaps accentuates effects that are more subtle at 5%. However, for simplicity we have focussed our discussion around physiological differences in comparison of expression of cells incubated in 1 and 5% oxygen.

It has previously been shown that some components of the placental RAS are most highly expressed in the first trimester (Pringle *et al.*, 2011) and that culture of HTR-8/SVneo cells in low oxygen increased ACE protein levels (Delforce *et al.*, 2016). Many factors can affect placental RAS gene expression; only one of these is placental miRNAs. Our data show that downregulation of miRNAs targeting most RAS mRNAs may boost RAS expression in 1% O_2 compared to 20% O_2 (Table VI), confirming our hypothesis that oxygen regulates these factors. In our physiologically relevant model of 1% compared with 5% oxygen, the level of expression of ACE and AGT and miRNAs targeting these mRNAs are significantly altered (Table VII). As well, in early

gestation, when oxygen tension is lowest, the suppression of miRNAs that target prorenin, prorenin receptor, angiotensinogen and ACE mRNAs is greatest (Wang *et al.*, 2018). We propose that a low oxygen milieu suppresses the expression of miRNAs that target RAS mRNAs, allowing increased expression of RAS mRNAs and proteins (Fig. 1). The increased AGT protein levels would result in a considerable increase in the potential of the placental RAS to modify placental cellular function and angiogenesis through increased production of angiotensin II and increased levels of AT_1R.

There are a number of reasons why miRNA and mRNA interactions are complex. MiRNAs are known to have many potential targets, because they require only partial complementarity to a target mRNA to mediate their effects. Although a specific miRNA may have high (> 85%) complementarity to a certain mRNA target sequence, this mRNA sequence is still only one of many possible targets. MiRNAs are also diverse in their functions, with the potential to bind to target mRNAs and reduce protein synthesis (Vasudevan *et al.*, 2007; Orom *et al.*, 2008) by downregulating gene translation, nuclear mRNA transcript stability or modulating alternative splicing when reimported into the nucleus (Roberts, 2014). They also possess the ability to act as messengers in cell-to-cell communication, such as when they are exported into the extracellular space and are able to act in an autocrine, paracrine (Gupta *et al.*, 2010), exocrine or endocrine (Zhu and Fan, 2011) capacity. For this reason, it is not possible to draw a direct link at this stage between miRNA expression and mRNA and expression.

In conclusion, we have shown that a number of miRNAs, that are predicted to target placental RAS mRNAs, are regulated by oxygen. Some of these miRNAs are repressed in early gestation when placental oxygen tension is lowest. This repression could result in activation of the placental RAS, so facilitating its role in normal placentation. MiRNAs downregulated in late-onset preeclamptic placentae are oxygen-sensitive, and their downregulation in these relatively hypoxic placentae, may also be responsible for activation of the placental RAS at this time. This may lead to inappropriate effects on foetal blood flow to the placenta and possibly increased vasoconstriction of maternal spiral arterioles, thus compromising foetal oxygen and nutrient supply.

Supplementary data

Supplementary data are available at *Molecular Human Reproduction* online.

Authors' roles

A.L.A. made substantial contributions to the design of the study, acquisition of data, analysis and interpretation of data, and in writing and revising the article. S.J.D. was involved in the acquisition of data, and revising the article for submission. A.M. was involved in the acquisition of data, analysis and interpretation of data, and critical revision of draft article for important intellectual content. E.R.L., B.J.M. and K.G.P. made substantial contributions to the conception and design, analysis and interpretation of data and in revising drafts of article critically for important intellectual content. All authors approved the final version of the article to be published.

Funding

Conflict of interest

The authors declare that they have no competing interests.

References

Benjamini Y, Hochberg Y. Controlling the false discovery rate: a practical and powerful approach to multiple testing. *J R Stat Soc Series B Stat Methodol* 1995;**57**:289–300.

Betoni J, Derr K, Pahl MC, Rogers L, Muller CL, Packard RE, Carey DJ, Kuivaniemi H, Tromp G. MicroRNA analysis in placentas from patients with preeclampsia: comparison of new and published results. *Hypertens Pregnancy* 2013;**32**:321–339.

Coppens M, Loquet P, Kollen F, De Neuburg F, Buytaert P. Longitudinal evaluation of uteroptacental and umbilical blood flow changes in normal early pregnancy. *Ultrasound Obstet Gynecol* 1996;**7**:114–121.

Cross J, Werb Z, Fisher SJ. Implantation and the placenta: key pieces of the development puzzle. *Science* 1994;**266**:1508–1518.

Cuffe J, Walton SL, Steane SE, Singh RR, Simmons DG, Moritz KM. The effects of gestational age and maternal hypoxia on the placental renin angiotensin system in the mouse. *Placenta* 2014;**35**:953–961.

Delforce S, Wang Y, Van-Aalst ME, Corbisier de Meaultsart C, Morris BJ, Broughton-Pipkin F, Roberts CT, Lumbers ER, Pringle KG. Effect of oxygen on the expression of renin-angiotensin system components in a human trophoblast cell line. *Placenta* 2016;**37**:1–6.

Genbacev O, Joslin R, Damsky CH, Polliotti BM, Fisher SJ. Hypoxia alters early gestation human cytotrophoblast differentiation/invasion in vitro and models the placental defects that occur in preeclampsia. *J Clin Invest* 1996;**97**:50.

Goyal R, Lister R, Leitzke A, Goyal D, Gheorghe CP, Longo LD. Antenatal maternal hypoxic stress: adaptations of the placental renin-angiotensin system in the mouse. *Placenta* 2011;**32**:134–139.

Goyal YS, Longo LD, Mata-Greenwood E. Placental gene expression in a rat 'model' of placental insufficiency. *Placenta* 2010;**31**:568–575.

Gu Y, Sun J, Groome LJ, Wang Y. Differential miRNA expression profiles between the first and third trimester human placentas. *Am J Physiol Endocrinol Metab* 2013;**304**:836–843.

Gupta S, Bang C, Thum T. Circulating microRNAs as biomarkers and potential paracrine mediators of cardiovascular disease. *Circ Cardiovasc Genet* 2010;**3**:484–488.

Herse F, Dechend R, Harsem NK, Wallukat G, Janke J, Qadri F, Hering L, Muller DN, Luft FC, Staff AC. Dysregulation of the circulating and tissue-based renin-angiotensin system in preeclampsia. *Hypertension* 2007;**49**:11.

Herse F, Staff AC, Hering L, Müller DN, Luft FC, Dechend R. AT1-receptor autoantibodies and uteroplacental RAS in pregnancy and preeclampsia. *J Mol Med* 2008;**86**:703.

Hromadnikova I, Kotlabova K, Ondrackova M, Kestlerova A, Novotna V, Hympanova L, Doucha J, Krofta L. Circulating C19MC microRNAs in preeclampsia, gestational hypertension, and fetal growth restriction. *Mediators Inflamm* 2013;**2013**:186041.

Ito M, Itakura A, Ohno Y, Nomura M, Senga T, Nagasaka T, Mizutani S. Possible activation of the renin-angiotensin system in the feto-placental unit in preeclampsia. *J Clin Endocrinol Metab* 2002;**87**:e8.

Jaffe R, Warsof SL. Color Doppler imaging in the assessment of uteroplacental blood flow in abnormal first trimester intrauterine pregnancies: an attempt to define etiologic mechanisms. *J Ultrasound Med* 1992;**11**:41–44.

Jaffe R, Woods JR. Color Doppler imaging and in vivo assessment of the anatomy and physiology of the early uteroplacental circulation. *Fertil Steril* 1993;**60**:293–297.

Laskowska M, Leszczynska-Gorzelak B, Laskowska K, Oleszczuk J. Evaluation of the renin-angiotensin-aldosterone system in pregnancy complicated by preeclampsia with and without intrauterine growth retardation. *Ann Univ Mariae Curie Sklodowska Med* 2004;**59**:e6.

Nielsen A, Schauser KH, Poulsen K. Current topic: the uteroplacental renin–angiotensin system. *Placenta* 2000;**21**:468–477.

Orom U, Nielsen FC, Lund AH. MicroRNA-10a binds the 5'UTR of ribosomal protein mRNAs and enhances their translation. *Mol Cell* 2008;**30**:460–471.

Pringle K, Tadros MA, Callister RJ, Lumbers ER. The expression and localization of the human placental prorenin/renin-angiotensin system throughout pregnancy: roles in trophoblast invasion and angiogenesis? *Placenta* 2011;**32**:956–962.

Pringle K, Wang Y, Lumbers ER. The synthesis, secretion and uptake of prorenin in human amnion. *Physiol Rep* 2015;**3**:12313.

Regnault T, de Vrijer B, Galan HL, Wilkening RB, Battaglia FC, Meschia G. Development and mechanisms of fetal hypoxia in severe fetal growth restriction. *Placenta* 2007;**28**:23.

Roberts T. The microRNA biology of the mammalian nucleus. *Mol Ther Nucleic Acids* 2014;**3**:e188.

Rodesch F, Simon P, Donner C, Jauniaux E. Oxygen measurements in endometrial and trophoblastic tissues during early pregnancy. *Obstet Gynecol* 1992;**80**:283–285.

Vasudevan S, Tong Y, Steitz JA. Switching from repression to activation: microRNAs can up-regulate translation. *Science* 2007;**318**:1931–1934.

Wang Y, Barbacioru C, Hyland F, Xiao W, Hunkapiller KL, Blake J, Chan F, Gonzalez C, Zhang L, Samaha RR. Large scale real-time PCR validation on gene expression measurements from two commercial long-oligonucleotide microarrays. *BMC Genomics* 2006;**7**:59.

Wang Y, Lumbers E, Arthurs AL, Corbisier de Meaultsart C, Mathe A, Avery-Kiejda KA, Roberts CT, Broughton Pipkin F, Marques FZ, Morris BJ *et al*. Regulation of the human placental (pro)renin receptor-prorenin-angiotensin system by microRNAs. *Mol Hum Reprod* 2018;**24**:453–464.

Zhu H, Fan GC. Extracellular/circulating microRNAs and their potential role in cardiovascular disease. *Am J Cardiovasc Dis* 2011;**1**:138–149.

**molecular
human
reproduction**

ORIGINAL ARTICLE

MicroRNA mimics that target the placental renin–angiotensin system inhibit trophoblast proliferation

Anya L. Arthurs[1,2], Eugenie R. Lumbers[1,2], and Kirsty G. Pringle [1,2,*]

[1]Priority Research Centre for Reproductive Sciences, School of Biomedical Sciences and Pharmacy, Faculty of Health and Medicine, University of Newcastle, Callaghan, New South Wales, Australia [2]Pregnancy and Reproduction Program, Hunter Medical Research Institute, Newcastle, New South Wales, Australia

*Correspondence address. Mothers and Babies Research Centre, Hunter Medical Research Institute, Level 3 East, 1 Kookaburra Circuit, New Lambton Heights, New South Wales 2305, Australia. Tel: +61-2-4042-0372; E-mail: kirsty.pringle@newcastle.edu.au orcid.org/0000-0002-6770-0496

In early gestation, the human placental renin–angiotensin system (RAS) is upregulated and plays a role in placental development. Among other functions, signalling through the angiotensin II type 1 receptor (AT$_1$R) initiates proliferation. Many microRNAs (miRNAs) targeting placental RAS mRNAs are downregulated at this time. We propose that in early gestation miRNAs that target the placental RAS are downregulated, allowing for the increased RAS expression and proliferation required for adequate placentation. HTR-8/SVneo cells (an immortalized human trophoblast cell line) were used to assess the effect of nine miRNA mimics (at 0.08, 0.16, 0.32 and 0.64 ng/µL) on trophoblast cell proliferation and predicted RAS target mRNAs. The effect of the miRNA mimics on the rate of cell proliferation was assessed using the xCELLigence real-time cell analysis system over 48 h. Levels of miRNAs and predicted RAS target mRNAs were determined by RT-PCR (qPCR, $n = 9$/group). Statistically different levels of expression were determined ($P < 0.05$). All nine miRNA mimics significantly affected the proliferation rates of HTR-8/SVneo cells. Five of the miRNA mimics (miR-181a-5p (predicted to target: renin (*REN*), angiotensin converting enzyme (*ACE*)), miR-378 (*REN, ACE*), miR-663 (*REN*), miR-483-3p (*ACE, ACE2*, angiotensinogen (*AGT*), angiotensin II type 1 receptor (*AGTR1*)) and miR-514 (*AGT*)) were associated with a dose-dependent reduction in cell proliferation. Seven of the mimics significantly decreased expression of at least one of their predicted target RAS mRNAs. Our study shows that miRNAs targeting placental RAS mRNAs play a role in controlling trophoblast proliferation. As placentation is largely a process of proliferation, changes in expression of these miRNAs may be partly responsible for the expression of the placental RAS, proliferation and placentation.

Key words: miRNA / renin–angiotensin system / placenta / proliferation / trophoblast

Introduction

During gestation, the placenta undergoes rapid trophoblast proliferation and development to cater to the needs of the growing foetus. The proliferative arm of the placental renin–angiotensin system (RAS) includes the following components: (pro)renin receptor ((P)RR), prorenin, the angiotensin converting-enzyme (ACE), angiotensinogen (AGT), angiotensin (Ang) I and II, and the Ang II type 1 receptor (AT$_1$R). This arm of the RAS is involved in cell and tissue growth (Goyal et al., 2010) and its expression in the placenta changes over gestation (Pringle et al., 2011). Importantly, irregular expression of the RAS is associated with placental complications, insufficient placental growth and intrauterine growth restriction (Laskowska et al., 2004). Expression of the majority of the placental RAS components are

highest in the first trimester of pregnancy, when the placenta is developing most rapidly. As gestation continues, expression of the placental RAS decreases (Pringle et al., 2011), which is suggested to be partly due to the actions of post-transcriptional regulators, including microRNAs (miRNAs) (Wang and Lumbers et al., 2018).

It is well established that miRNA profiles in both the placenta and the maternal circulation are significantly changed in pathological pregnancies (Pineles et al., 2007; Anton et al., 2013; Choi et al., 2013; Hromadnikova et al., 2013; 2017; Lalevee et al., 2014; Luo et al., 2014; Akehurst et al., 2015; Jairajpuri et al., 2017; Lu et al., 2017; Wang and Lumbers et al., 2018), with a number of miRNAs predicted to target the placental RAS being among those that are altered. For example, miR-378, miR-514, miR-663 and miR-892 were found to be overexpressed in placentae from women with pre-eclampsia (Wang and

Lumbers *et al.*, 2018), a disease of placental insufficiency. Importantly, dysregulation of placental RAS mRNA expression is also seen in women with pre-eclampsia (Anton *et al.*, 2009; Fatini *et al.*, 2016; Nartita *et al.*, 2016).

During pregnancy, many miRNAs predicted to target the placental RAS have a level of expression that is reciprocal to that of placental RAS genes; that is, in early pregnancy (<12 weeks) when RAS expression is highest, miRNAs predicted to target these RAS mRNAs are at their lowest (Wang and Lumbers *et al.*, 2018). We hypothesize that endogenous miRNAs assist in the post-transcriptional control of RAS gene expression to regulate normal placental growth. The direct effects of RAS-targeting miRNAs on trophoblast proliferation have not yet been determined, so that the links between RAS expression, reciprocal miRNA expression and placental growth are by association only. We propose that miRNAs interact with the placental RAS to inhibit translation, and this results in decreased trophoblast proliferation. We have tested this hypothesis using miRNA mimics, compounds that mimic endogenous miRNAs, and measured the effects of increased expression of miRNAs that target the RAS on proliferation of extravillous trophoblast cells.

Materials and Methods

Cell culture

HTR-8/SVneo cells, which are an immortalized human first trimester extravillous trophoblast cell line, were cultured at 37°C with 5% CO_2 in room air in Rosewell Park Memorial Institute (RPMI)-1640 medium (HyClone, GE Healthcare Australia Pty Ltd., Paramatta, Australia) supplemented with 10% heat inactivated fetal calf serum (FCS; SAFC Biosciences, Castle Hill, Australia) and 1% L-glutamine. The $2–5 \times 10^5$ cells from passages 10–20 were plated in each well of a 6-well plate with 2 mL of incubation medium per well and allowed to equilibrate for 24 h ($n = 3$ experiments, each in triplicate). There was no relationship between the number of cells plated and the cell index trajectory. After this 24 h equilibration period, 0.32 ng/μL of miRNA miRVana™ mimics (Life Technologies, Thermo Fisher Scientific, Waltham, USA) were added to each well, using Lipofectamine as a transfection vector. Only one dose was used for transfection of mimics for RNA and protein analysis purposes. Other cells were treated either by adding Lipofectamine (Thermo Fisher Scientific) alone (vehicle control) or by addition of a scrambled control (Life Technologies), where nucleotides are scrambled in a random order, in conjunction with Lipofectamine ($n = 3$ experiments, each in triplicate). After 48 h, cells and culture media were collected and snap frozen in liquid nitrogen at −80°C before RNA and protein analysis.

Proliferation analysis

Fifty μL of incubation medium was added to each well of an xCELLigence E-plate 16 (ACEA Biosciences Inc., San Diego, CA) and allowed to equilibrate at room temperature for 30 min. A background reading in the xCELLigence Real-Time Cell Analysis Multi Plate (RCTA MP) system was then conducted. 1×10^4 HTR-8/SVneo cells from passages 10–20 (cultured as above) were plated in each well with an additional 100 μL of incubation medium and again allowed to equilibrate for 30 min at room temperature. 24 h after cell plating, miRNA miRVana mimics, scrambled mimics or vehicle (lipofectamine) control were added to each well at 0.08, 0.16, 0.32 or 0.64 ng/μL. As the proliferation plates have gold microelectrodes on the bottom of each well, the proliferation of cells impedes electrical conductance. Cell index was generated as a measure of the electrical resistance as cells proliferated. The cell index was measured every 30 min

for 48 h in the xCELLigence RCTA MP system. After 48 h of incubation with treatment, data were collected and analysed. The rate of proliferation was determined by calculating the slope of the line (cell index) between each individual measurement, for each of the three technical replicates within each experiment, and combining for the average. The xCELLigence plots, showing the mean cell index (of $n = 3$ experiments, each in triplicate) at each time point for each miRNA mimic, are presented in Supplementary Fig. S1.

RNA extraction and DNase treatment

Total RNA extraction of HTR-8/SVneo cells was performed using the miRNeasy kit, according to the manufacturer's instructions (Qiagen, Chadstone, Australia). DNase I treatment was performed on all samples (Qiagen). The integrity of total RNA and miRNAs was examined by gel electrophoresis and quantified using the Nanodrop 2000 (data not shown). Samples were used for further analysis if the 260:280 ratios were >1.8.

miRNA analysis

Expression of miRNAs was measured by qPCR. Total RNA (5 ng) samples underwent reverse transcription to cDNA (TaqMan miRNA Reverse Transcription Kit and probes; Applied Biosystems, Thermo Fisher Scientific) according to the manufacturer's instructions. Samples then underwent quantitative PCR (RT-qPCR) using TaqMan Universal PCR master mix, according to the manufacturer's instructions (Applied Biosystems, Thermo Fisher Scientific). Results were quantified using a 7500 Real-Time PCR System (Applied Biosystems). The expression levels of nine miRNAs (miR-181a-5p, miR-181a-3p, miR-663, miR-378, miR-34c, miR-892, miR-514, miR-454 and miR-483-3p) were determined by calculating $2^{-\Delta\Delta CT}$ using RNU44 (a highly conserved small nucleolar RNA in the growth arrest specific 5 transcript) as the house-keeping gene.

qPCR

All RNA samples underwent reverse transcription to cDNA (Superscript III First-Strand Synthesis for RT, Thermo Fisher Scientific) using the manufacturer's instructions. Total RNA was spiked with a known amount of Alien RNA (10^7 copies per μg of total RNA; Stratagene, Agilent; Santa Clara, USA). qPCR was performed in an Applied Biosystems 7500 Real Time PCR System using SYBR Green for detection. Each reaction contained 5 μL of SYBR Green PCR master mix (Applied Biosystems), RAS primers as described previously (Wang and Lumbers *et al.*, 2018), cDNA reversed transcribed from 10 ng total RNA, and water to 10 μL. Messenger RNA abundance was calculated using the $2^{-\Delta\Delta CT}$ method and expressed relative to ACTB mRNA and a calibrator (a term placental sample collected at elective caesarean section).

Statistics

Statistical analysis was undertaken using GraphPad Prism 7. A one-way ANOVA (non-parametric) was conducted using a Kruskal Wallis test with Dunn's multiple comparisons test. Where only two groups were compared, a Mann–Whitney test was conducted. Differences between groups were considered significant where $P \leq 0.05$.

Results

The effect of the negative controls and scrambled controls on miRNA expression, RAS mRNA expression and the rate of cell proliferation was first tested to ensure that any effects of the mimics were specific (Supplementary Figs S2–S4). The scrambled control mimic had no

effect on miRNA expression (Supplementary Fig. S2), RAS mRNA expression (Supplementary Fig. S3) or the rate of cell proliferation (Supplementary Fig. S4) compared to vehicle control treated cells. Therefore, the vehicle control was used for all subsequent experiments as the control for the miRNA mimics.

The effect of mimics for miRNAs predicted to target renin (REN) and angiotensin converting enzyme (ACE) mRNAs on RAS gene expression and cell proliferation in HTR-8/SVneo cells

HTR-8/SVneo cells expressed all of the examined miRNAs that were predicted to target RAS mRNAs. HTR-8/SVneo cells treated with miR-181a-5p and miR-378 mimics had significantly elevated levels of

miR-181a-5p ($P < 0.001$; Fig. 1A) and miR-378 ($P = 0.040$; Fig. 1E), respectively, when compared with the vehicle (lipofectamine) control. In addition, *REN* mRNA expression was decreased in cells treated with miR-181a-5p mimic ($P = 0.032$; Fig. 1B) or miR-378 mimic ($P = 0.0009$; Fig. 1F). The abundance of *ACE* mRNA was unchanged with the addition of the miR-181a-5p mimic (Fig. 1C) but was decreased with the addition of the miR-378 mimic ($P = 0.002$; Fig. 1G).

At miR-181a-5p mimic concentrations of 0.08, 0.16, 0.32 and 0.64 ng/μL, the rate of cell proliferation was significantly decreased compared with the vehicle (lipofectamine) control ($P < 0.0001$ for all; Fig. 1D). The decrease in proliferation was greater in cells that were transfected with 0.64 ng/μL of mimic compared with cells transfected with 0.08 and 0.16 ng/μL ($P = 0.0004$, $P = 0.0008$; respectively). Treatment with the miR-378 mimic significantly decreased proliferation at 0.16, 0.32 and 0.64 ng/μL compared with the vehicle control
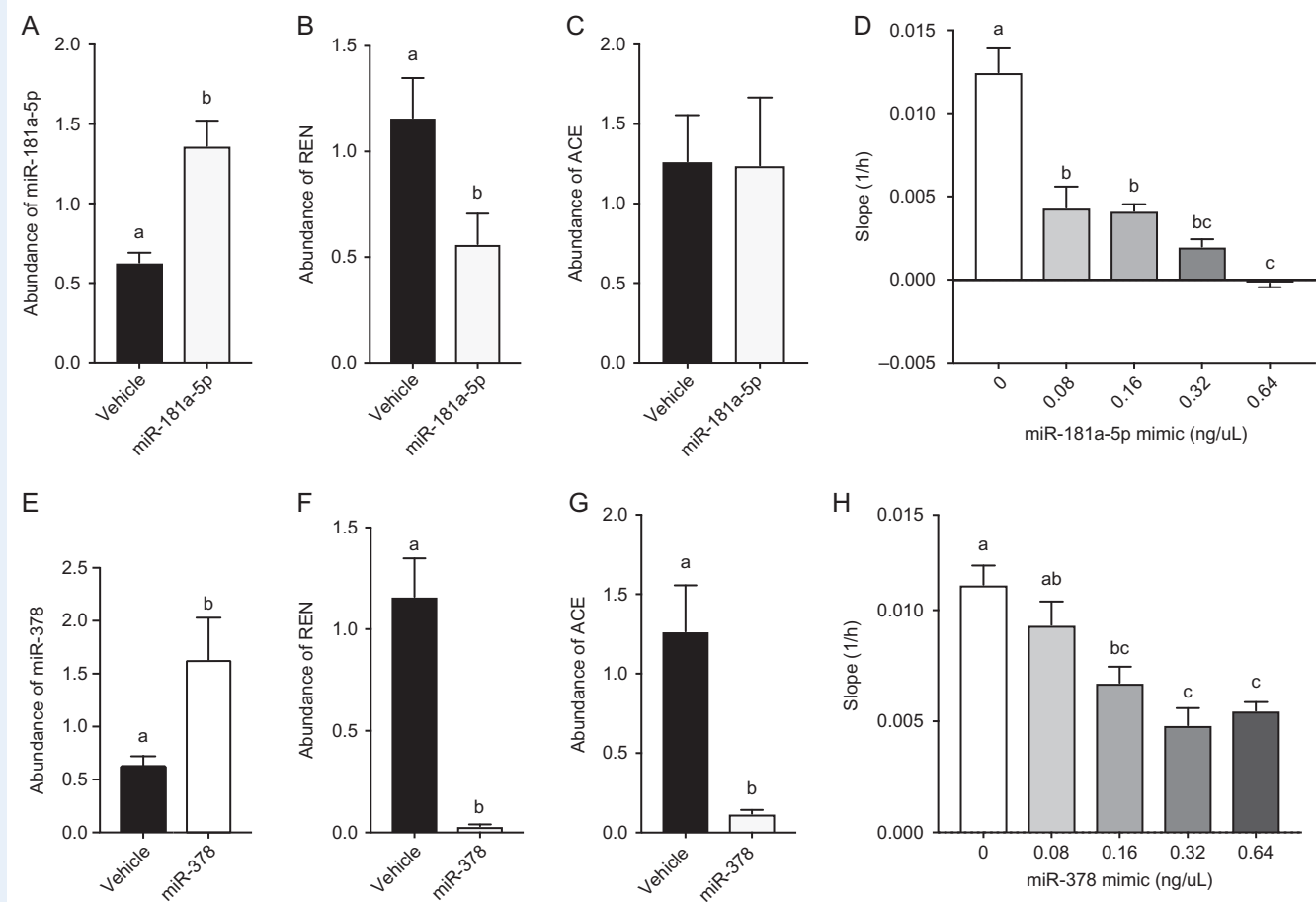
Figure 1 Effect of microRNA (miR)-181a-5p and miR-378 mimics on miR-181a-5p and miR-378 expression, respectively, as well as the effects of these mimics on renin (*REN*) and angiotensin converting enzyme (*ACE*) mRNA expression and HTR-8/SVneo (human trophoblast cell line) cell proliferation. (**A**) In HTR-8/SVneo cells treated with 0.32 ng/μL miR-181a-5p mimic, miR-181a-5p expression was significantly increased and (**B**) *REN* mRNA expression was decreased compared to the vehicle control but (**C**) *ACE* mRNA expression was unchanged. (**D**) The rates of cell proliferation in cells exposed to the miR-181a-5p mimic were significantly reduced by all concentrations of miR-181a-5p mimic compared to the vehicle control (0 ng/μL mimic). (**E**) In HTR-8/SVneo cells treated with 0.32 ng/μL miR-378 mimic, miR-378 expression was significantly increased compared with the vehicle control and (**F**) *REN* and (**G**) *ACE* expression were significantly decreased. (**H**) The rate of cell proliferation in cells exposed to the miR-378 mimic was significantly decreased at 0.16, 0.32 and 0.64 ng/μL compared to the vehicle control (0 ng/μL mimic). Data are presented as mean ± SEM. $N = 3$ experiments in triplicate. The same letter above bars indicates that groups are not different from each other. A different letter above bars indicates that groups are different (all $P < 0.05$).

($P = 0.008$, $P < 0.0001$, $P = 0.0002$, respectively; Fig. 1H). Treatment with 0.32 and 0.64 ng/µL mimic were also associated with decreased rates of proliferation compared to treatment with 0.08 ng/µL of mimic ($P = 0.0008$, $P = 0.005$; respectively).

The effect of mimics for miRNAs predicted to target REN mRNA on RAS gene expression and cell proliferation in HTR-8/SVneo cells

Cells exposed to a mimic for miR-181a-3p and miR-663 had significantly elevated levels of miR-181a-3p ($P = 0.049$; Fig. 2A) and miR-663 ($P = 0.013$; Fig. 2D), respectively, compared with the vehicle (lipofectamine) control. These cells also had decreased expression of REN

mRNA when treated with the miR-181a-3p mimic ($P = 0.033$; Fig. 2B) and the miR-663 mimic ($P = 0.039$; Fig. 2E) compared to the vehicle controls.

The rate of cell proliferation was significantly reduced following transfection of the miR-181a-3p mimic at a concentration of 0.64 ng/µL compared with vehicle control and cells transfected with 0.08 and 0.16 ng/µL of mimic ($P = 0.036$, $P = 0.002$, $P = 0.036$, respectively; Fig. 2C).

Proliferation was significantly decreased in cells treated with miR-663 mimic at concentrations of 0.08, 0.16, 0.32 and 0.64 ng/µL compared with the vehicle control ($P = 0.018$, $P = 0.003$, $P < 0.0001$, $P < 0.0001$, respectively; Fig. 2F). Proliferation was also significantly decreased at 0.64 ng/µL of miR-663 mimic compared to 0.08 ng/µL ($P = 0.047$).
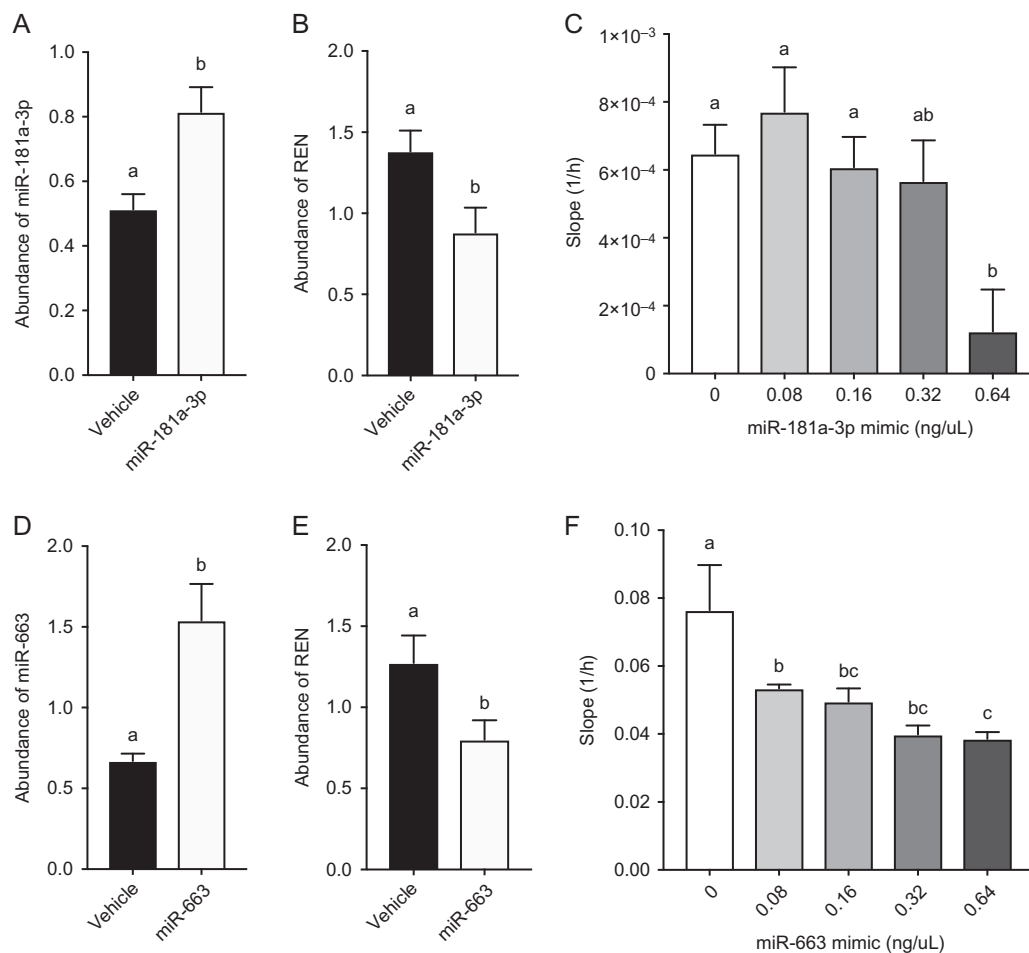
Figure 2 **Effect of microRNA (miR)-181a-3p and miR-663 mimics on miR-181a-3p and miR-663 expression respectively, as well as the effects of these mimics on renin (REN) mRNA expression and HTR-8/SVneo (human trophoblast cell line) cell proliferation.** (**A**) In HTR-8/SVneo cells treated with 0.32 ng/µL miR-181a-3p mimic, miR-181a-3p expression was significantly increased and (**B**) REN mRNA expression was significantly decreased compared with vehicle (lipofectamine) control. (**C**) The rate of cell proliferation in cells transfected with miR-181a-3p mimic was significantly decreased at 0.64 ng/µL compared to vehicle control (0 ng/µL mimic). (**D**) In HTR-8/SVneo cells treated with 0.32 ng/µL miR-663 mimic, miR-663 expression was significantly increased and (**E**) REN expression was significantly decreased compared with the vehicle control. (**F**) The rate of cell proliferation in cells exposed to miR-663 mimic was significantly decreased at 0.08, 0.16, 0.32 and 0.64 ng/µL compared to the vehicle control (0 ng/µL mimic). Data are presented as mean ± SEM. $N = 3$ experiments in triplicate. The same letter above bars indicates that groups are not different from each other. A different letter above bars indicates that groups are different (all $P < 0.05$).
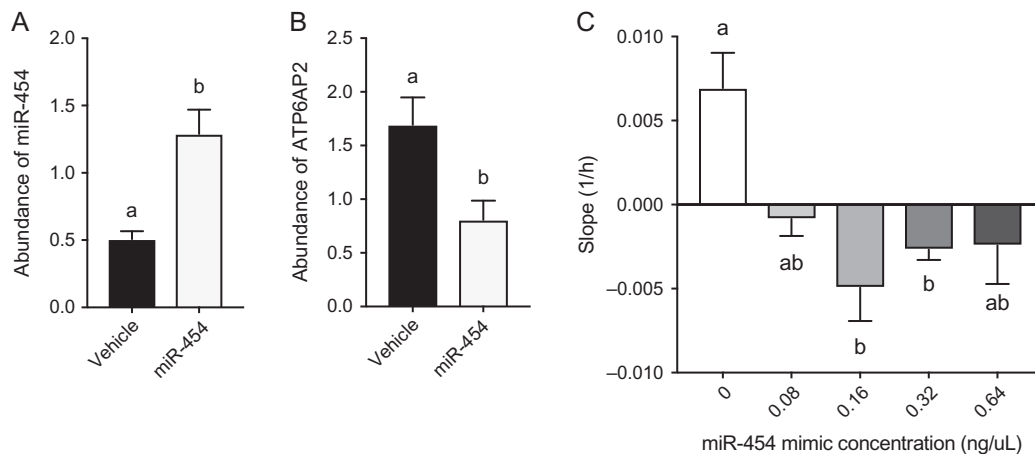
Figure 3 Effect of microRNA (miR)-454 mimic on miR-454 and (pro)renin receptor (*ATP6AP2*) mRNA expression, and on HTR-8/SVneo (human trophoblast cell line) cell proliferation. (**A**) In HTR-8/SVneo cells treated with 0.32 ng/μL miR-454 mimic, miR-454 expression was significantly increased and (**B**) *ATP6AP2* expression was significantly decreased when compared to vehicle (lipofectamine) control. (**C**) Proliferation was abolished by all doses of miR-454 mimic. Data are presented as mean ± SEM. $N = 3$ experiments in triplicate. The same letter above bars indicates that groups are not different from each other. A different letter above bars indicates that groups are different (all $P < 0.05$).

The effect of mimics for miRNAs predicted to target (pro)renin receptor (ATP6AP2) mRNA on RAS gene expression and cell proliferation in HTR-8/SVneo cells

Cells treated with a mimic for miR-454 had significantly increased expression of miR-454 compared with the vehicle control ($P = 0.049$; Fig. 3A). *ATP6AP2* mRNA expression was significantly decreased ($P = 0.036$; Fig. 3B). Cell proliferation was abolished by transfection with all concentrations of miR-454 (0.16 ng/μL compared with vehicle control; $P = 0.0048$, and 0.32 ng/μL compared with vehicle control; $P = 0.0329$) (Fig. 3C).

The effect of mimics for miRNAs predicted to target angiotensin II type 1 receptor (AGTR1) and angiotensinogen (AGT) mRNAs on RAS gene expression and cell proliferation in HTR-8/SVneo cells

Cells treated with mimics for miR-34c and miR-892 had significantly increased expression of miR-34c ($P = 0.002$; Fig. 4A) and miR-892 ($P = 0.034$; Fig. 4D), respectively, compared with the vehicle control. *AGTR1* mRNA expression was not significantly changed with addition of miR-34c mimic (Fig. 4B) nor was *AGT* mRNA expression changed with addition of the miR-892 mimic (Fig. 4E).

Proliferation was significantly decreased with the addition of 0.64 ng/μL of the miR-34c mimic compared to 0.08 and 0.32 ng/μL ($P < 0.001$, $P = 0.003$; respectively, Fig. 4C).

Proliferation was significantly decreased at 0.64 ng/μL of miR-892 mimic compared with 0.08, 0.16 and 0.32 ng/μL (all $P < 0.001$; Fig. 6C). Proliferation rates at 0.08 and 0.16 ng/μL were significantly increased compared with the vehicle control (both $P < 0.001$) and 0.32 ng/μL ($P = 0.008$, $P = 0.007$; respectively). The rate of cell

proliferation was significantly upregulated when transfected with 0.32 ng/μL of mimic compared to the vehicle control ($P = 0.002$).

Cells treated with a mimic for miR-514 demonstrated significantly increased abundance of miR-514 ($P = 0.039$; Fig. 5A) and decreased *AGTR1* and *AGT* mRNA abundance ($P = 0.031$, $P = 0.043$; Fig. 5B and C) compared with the vehicle control. Treatment with the miR-514 mimic significantly decreased proliferation at 0.08, 0.16, 0.32 and 0.64 ng/μL compared to the vehicle control ($P = 0.009$, $P = 0.004$, $P < 0.0001$, $P = 0.004$, respectively; Fig. 5D). Proliferation rates of cells transfected with 0.16, 0.32 and 0.64 ng/μL concentrations were also less than that of cells treated with 0.08 ng/μL of mimic ($P = 0.044$, $P = 0.012$, $P = 0.046$, respectively).

The effect of mimics for miRNAs predicted to target AGTR1, AGT and ACE mRNAs on RAS gene expression and cell proliferation in HTR-8/SVneo cells

Following treatment with a miR-483-3p mimic, cells exhibited increased expression of miR-483-3p ($P = 0.009$; Fig. 6A) and decreased *AGTR1* mRNA levels ($P = 0.049$; Fig. 6B) compared with the vehicle control. Expression of *AGT* and *ACE* mRNAs were not changed compared with the vehicle control (Fig. 6C and D, respectively). Proliferation rates of cells treated with 0.32 and 0.64 ng/μL miR-483-3p mimic were significantly decreased compared with the vehicle control ($P < 0.0001$ for both; Fig. 6E) and 0.16 ng/μL ($P = 0.0055$, $P < 0.0001$, respectively). Proliferation was also decreased at a miR-483-3p mimic concentration of 0.64 ng/μL compared with 0.08 ng/μL ($P = 0.0009$).

Discussion

We have previously measured the expression of miRNAs predicted to target the placental RAS throughout gestation and found a negative
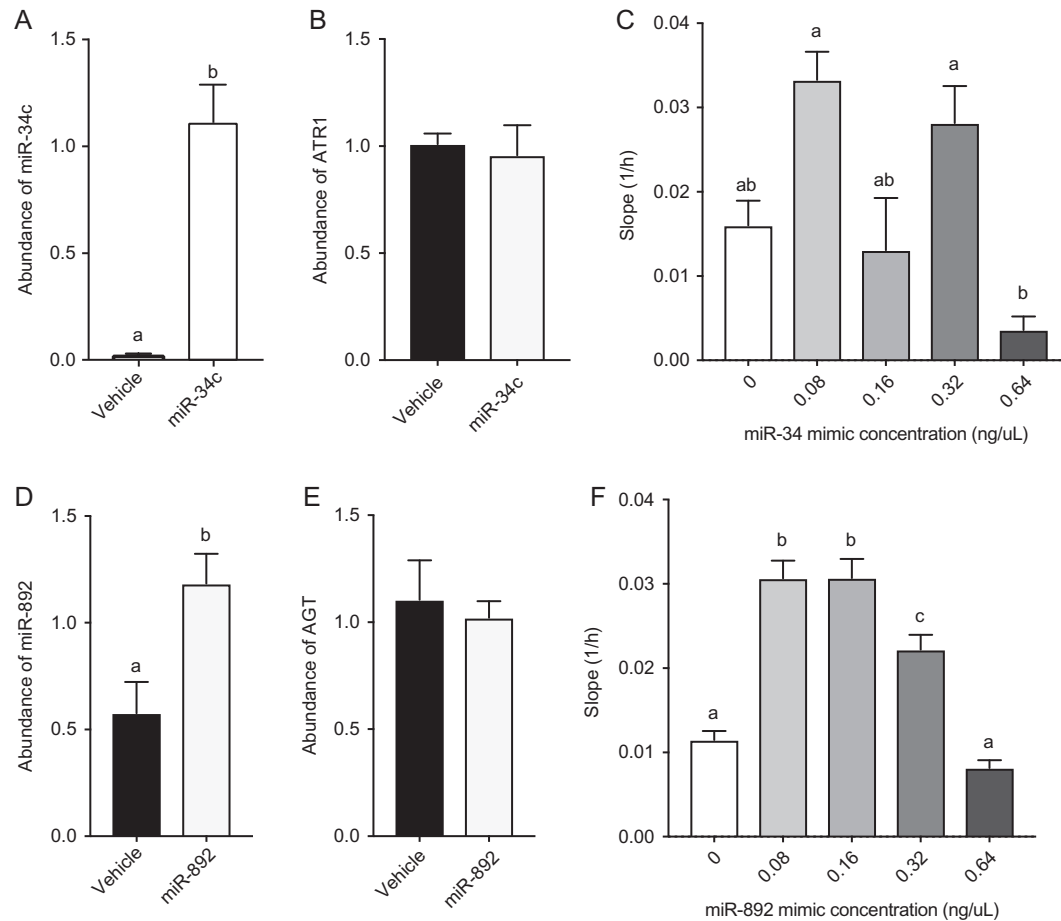
Figure 4 Effect of microRNA (miR)-34c and miR-892 mimics on miR-34c and angiotensin II type 1 receptor (*AGTR1*) expression, and on miR-892 and angiotensinogen (*AGT*) expression, respectively, as well as the effects of these mimics on HTR-8/SVneo (human trophoblast cell line) cell proliferation. (**A**) In HTR-8/SVneo cells treated with 0.32 ng/μL miR-34c mimic, miR-34c expression was significantly increased but (**B**) *AGTR1* mRNA was not altered compared to the vehicle control. (**C**) The rate of cell proliferation in cells exposed to miR-34c mimic was significantly decreased at 0.64 ng/μL when compared to 0.08 and 0.32 ng/μL. (**D**) In HTR-8/SVneo cells treated with 0.32 ng/μL miR-892 mimic, miR-892 expression was significantly increased but (**E**) *AGT* expression was not significantly altered compared to the vehicle control. (**F**) The rate of cell proliferation in cells exposed to miR-892 mimic was significantly decreased at 0.64 ng/μL compared with 0.08, 0.16 and 0.32 ng/μL, and significantly increased at 0.08, 0.16 and 0.32 ng/μL compared with vehicle (0 ng/μL mimic) control and 0.64 ng/μL. Data are presented as mean ± SEM. $N = 3$ experiments in triplicate. The same letter above bars indicates that groups are not different from each other. A different letter above bars indicates that groups are different (all $P < 0.05$).

relationship between the miRNAs and their RAS targets (Wang and Lumbers *et al.*, 2018). RAS mRNAs were significantly increased in the first trimester of gestation, when placentation is greatest, and at this time miRNAs targeting these RAS mRNAs were downregulated. Thus, we hypothesized that miRNAs targeting placental RAS mRNAs are able to inhibit or slow placental development as measured by the rate of proliferation of extravillous trophoblasts which invade the decidua and plug maternal uterine arterioles. In this study, we have shown that these miRNAs do target the placental RAS and reduce the rate of proliferation of HTR-8/SVneo cells. Treatment with their specific miRNA mimic was associated with increased cellular expression of all nine miRNA mimics studied, compared with the vehicle. Of these nine miRNA mimics, seven successfully downregulated one or more of

their predicted RAS target mRNAs; these were miR-181a-3p, miR-181a-5p, miR-378, miR-454, miR-483-3p, miR-514 and miR-663.

All nine miRNA mimics had some effect on trophoblast proliferation, although this effect varied. Five of the mimics tested (miR-181a-5p, miR-378, miR-663, miR-483-3p and miR-514) decreased trophoblast proliferation in a dose-dependent manner, with increasing mimic concentrations resulting in decreasing proliferation rates. These mimics decreased expression of *REN* (miR-181a-5p, miR-378, miR-663); *AGT* (miR-514); and *ACE* (miR-378). Another one of the mimics (miR-181a-3p; mRNA target, *REN*) tended to be associated with a dose-dependent fall in proliferation rate, but a significant decrease in cell proliferation only occurred with the highest dose. Furthermore, miR-892 (target, *AGT*) and miR-34c (target, *AGTR1*) mimics had
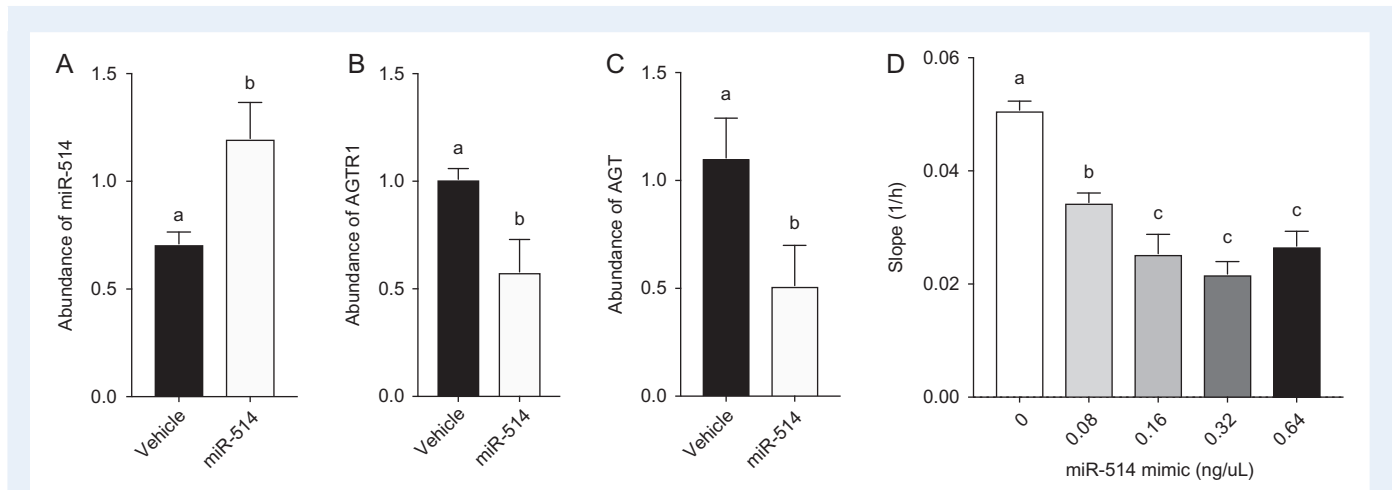
Figure 5 Effect of microRNA (miR)-514 mimic on miR-514, angiotensin II type 1 receptor (*AGTR1*) and angiotensinogen (*AGT*) expression, and on HTR-8/SVneo (human trophoblast cell line) cell proliferation. (**A**) In HTR-8/SVneo cells treated with 0.32 ng/μL miR-514 mimic, miR-514 expression was significantly increased and (**B**) *AGTR1* and (**C**) *AGT* mRNA were significantly decreased compared with vehicle control. (**D**) The rate of cell proliferation in cells exposed to miR-514 mimic was significantly decreased at 0.08, 0.16, 0.32 and 0.64 ng/μL concentrations compared with the vehicle control (0 ng/μL mimic). Data are presented as mean ± SEM. $N = 3$ experiments in triplicate. The same letter above bars indicates that groups are not different from each other. A different letter above bars indicates that groups are different (all $P < 0.05$).

biphasic effects on cell proliferation. Lastly, miR-454 (target, *ATP6AP2*) was cytotoxic, with cell death occurring particularly at the highest concentrations of the mimic.

Mimics targeting *REN* mRNA successfully downregulated *REN* mRNA expression and displayed a dose-dependent effect on cell proliferation. With the knowledge that the placental RAS pathway, initiated by prorenin, is implicated in trophoblast proliferation and placental development (Paul *et al.*, 2006), the effects of miR-181a-5p, miR-663 and miR-378 on *REN* mRNA and the associated decrease in proliferation rate of extravillous trophoblasts, explains in part why they have been associated with placental complications (Cai *et al.*, 2017). Mature miR-181a is associated with downregulation of the transforming growth factor-B (TGF-B) pathway and has been shown to inhibit proliferation in mesenchymal stem cells (Liu *et al.*, 2012). Importantly, differential expression of miR-181a-5p has been detected in placentae from women delivering preterm (Liu *et al.*, 2012). MiR-378, which also downregulated *ACE* mRNA expression, has been linked with trophoblast migration and invasion by targeting nodal, a gene encoding for a secreted ligand of the TGF-B protein superfamily. Its dysregulation contributes to pre-eclampsia (Luo *et al.*, 2012). miR-663 is also dysregulated in late-onset pre-eclampsia (Wang and Lumbers *et al.*, 2018).

The fourth miRNA mimic that targets *REN* mRNA, miR-181a-3p, tended to cause a dose-dependent decrease in proliferation as seen in the other mimics targeting *REN*, but its effects were only significant at the highest dose. The relationship between miR-181a-3p and *REN* is well defined (Marques *et al.*, 2011), as is the positive correlation between *REN* and proliferation. A causal link is suggested in the literature between miR-181a-3p, *REN* and cell proliferation in kidneys (Marques *et al.*, 2011) but this has not been investigated in trophoblasts.

Interestingly, addition of the miR-454 mimic, which successfully downregulated *ATP6AP2* mRNA expression in HTR-8/SVneo cells, induced cell death at all concentrations. This is evident from the

negative slope of the cell index lines (Fig. 3, Supplementary Fig. S1E) of cells treated with any concentration of the miR-454 mimic. As cells die, they detach from the bottom of the wells and are no longer measured by the xCELLigence machine. This differs from cell quiescence, as the cells simply do not proliferate and, as shown, there is a flat line with no gradient. Expression of (P)RR is downregulated in the placentae from preeclamptic women and furthermore, (P)RR knock-out has been shown to be embryo-lethal (Burcklé and Bader, 2006). As miR-454 moderately downregulates (P)RR expression, this could explain the cytotoxic effect we see as the cells experienced cell death.

It should also be noted, however, that a slightly lower cell index was seen for all miR-514 mimic treatment groups compared to other mimics plated with the same cell number (miR-378, miR-181a-5p, miR-892) (Supplementary Fig. S1). However, the small increase in the slope of the cell index line seen in the negative control cells is comparable to the slope seen in cells treated with the miR-181a-3p mimic. Therefore, we suggest that this is variation between batches of cells, as opposed to an error in experimental procedure. Furthermore, the initial low cell index, or small increase in the slope of the line, as seen in other mimic experiments did not lead to cell death. Thus we can conclude that cell death seen by cells treated with the miR-454 mimic was a consequence of treatment with the mimic.

Little has been published regarding the role of miR-892 in the growing placenta. In a microarray that we previously carried out, miR-892 was one of three RAS-targeting miRNAs significantly upregulated in placentae from early-onset preeclamptic women compared with women with uncomplicated pregnancies (Wang and Lumbers *et al.*, 2018). miR-892 is predicted to target the RAS gene *AGT* with <95% sequence complementarity. AGT undergoes catalytic reduction to form Ang I in the RAS cascade, and then Ang I is converted to Ang II. Ang II acts predominantly on the AT$_1$R, stimulating proliferation (MacGregor *et al.*, 1981). Downregulation of AGT by miR-892 should, predictably, downregulate proliferation. However, it is possible that miR-892 is working by
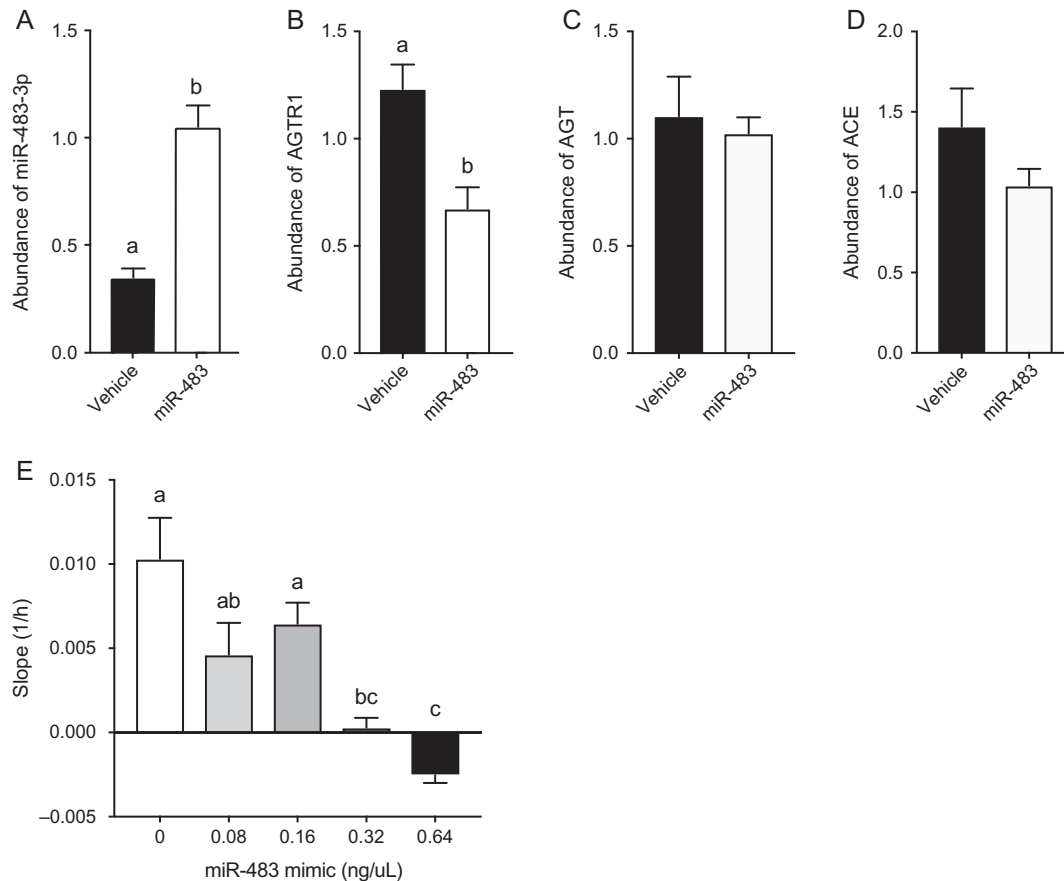
Figure 6 Effect of microRNA (miR)-483-3p mimic on miR-483-3p, angiotensin II type 1 receptor (*AGTR1*), angiotensinogen (*AGT*), and angiotensin converting enzyme (*ACE*) expression, and on HTR-8/SVneo (human trophoblast cell line) cell proliferation. (**A**) In HTR-8/SVneo cells treated with 0.32 ng/μL miR-483-3p mimic, miR-483-3p expression was significantly increased and (**B**) *AGTR1* expression was significantly decreased when compared to the vehicle control. Expression of (**C**) *AGT* and (**D**) *ACE* mRNA were not significantly altered compared to the vehicle control. (**E**) The rate of cell proliferation in cells exposed to miR-483-3p mimic was significantly decreased at 0.32 and 0.64 ng/μL compared to the vehicle control (0 ng/μL mimic). Data are presented as mean ± SEM. $N = 3$ experiments in triplicate. The same letter above bars indicates that groups are not different from each other. A different letter above bars indicates that groups are different (all $P < 0.05$).

repressing another predicted target, peroxisome proliferator-activated receptor-G (PPAR-G). PPAR-G represses vascular endothelial growth factor (VEGF) gene expression (Peeters *et al.*, 2005) and produces an anti-proliferative environment; thus, targeted inhibition by miR-892 could result in an increase in proliferation upon treatment with this mimic, which is consistent with our results. This should be confirmed by further studies.

MiR-514 is predicted to target both *AGT* and *AGTR1* mRNA, although there are no current studies that confirm this. We have shown that miR-514 does reduce both *AGT* and *AGTR1* mRNA expression and trophoblast proliferation in a dose-dependent manner. MiR-514 is a placenta-specific miRNA and is known to decrease cell proliferation by targeting Src homology region 2-containing protein tyrosine phosphatase (Shp2) (Lui and Forbes, 2012). Its expression is dysregulated in pre-eclampsia, with unusually high levels of miR-514 found in placentae from early-onset pre-eclampsia (Wang and Lumbers *et al.*, 2018). miR-483-3p is also predicted to target both *AGT* and *AGTR1* mRNA, as well as *ACE* and *ACE2* mRNA, however only *AGTR1* expression was reduced. Trophoblast proliferation

was also reduced in a dose-dependent manner, with no proliferation seen in cells treated with the highest doses of the mimic. We believe this could be due to the vast number of targets that miR-483-3p acts upon. miR-483-3p is not only predicted to target 4 RAS targets (mentioned above), but also a number of other important genes, thereby prohibiting cell proliferation. For example, miR-483-3p has been shown to negatively regulate trophoblast proliferation and IGF-1 expression (Forbes, 2012), which is known to promote proliferation and inhibit apoptosis in human trophoblast cells (Forbes *et al.*, 2008). Additionally, IGF-2-derived intronic miR-483-3p is overexpressed in placentae from women delivering infants with macrosomia (Li *et al.*, 2018).

miR-34c is also predicted to target *AGTR1* mRNA, although we did not find any significant change in its expression. Suppression of mature miR-34 has been shown to increase trophoblast invasion (Umemura *et al.*, 2013) but we are unable confirm this observation. By combining previous knowledge of the miRNA's effects on proliferation, we can only conclude that more sequences than just *AGTR1* mRNA were targeted by miR-34c.

One limitation of this study that will be investigated in the future is the effect of these miRNA mimics on RAS protein expression. Although we have shown that there are significant alterations in the RAS mRNA levels when treated with these miRNA mimics, as miRNAs are known to be post-transcriptional regulators, it would be beneficial to examine their effects on translation of their targets.

Another limitation of this study is the variation in proliferation rates of cells as measured by the xCELLigence machine. Most experiments were plated using the same protocol, there was however a large degree of variability in proliferation of the cells, despite using the same cell line. This could be due to the sensitivity of the xCELLigence machine, as even small changes in positioning, temperature and humidity can affect results. Where possible, replicate experiments were completed within a short period to minimize differences, however this could not be done for separate mimic experiments. Therefore differences seen were between mimic experiments, but not within experiments.

In summary, we have explored the varied effects of miRNAs targeting the placental RAS on HTR-8/SVneo cells, and confirmed that a number of miRNAs, miR-181a-3p, miR-181a-5p, miR-378, miR-663, miR-483-3p and miR-514, both target the predicted RAS mRNAs and decrease cell proliferation. We have shown therefore that miRNAs that have a changing pattern of expression in the human placentae throughout gestation and in pre-eclampsia, which we predicted would target the placental RAS, do in fact do so. In addition, we have shown that the expression of almost all of the placental RAS mRNAs are suppressed by at least one of the nine miRNA mimics that we studied. Bearing in mind that there is very high expression of prorenin in early gestation (Itskovitz *et al.*, 1992; Pringle *et al.*, 2011) it is impressive that four of the mimics we studied have *REN* mRNA as a target. It is also worth speculating that a combination of these miRNAs could be of greater value in treating other conditions associated with over expression of the RAS (e.g. hypertension, diabetic nephropathy and retinopathy).

Supplementary data

Supplementary data are available at *Molecular Human Reproduction* online.

Authors' roles

A.L.A. made substantial contributions to the design of the study, acquisition of data, analysis and interpretation of data, and in writing and revising the article. E.R.L. and K.G.P. made substantial contributions to the conception and design, analysis and interpretation of data and in revising drafts of article critically for important intellectual content. All authors approved the final version of the manuscript to be published.

Funding

Conflict of interest

References

Akehurst C, Small HY, Sharafetdinova L, Forrest R, Beattie W, Brown CE, Robinson SW, McClure JD, Work LM, Carty DM *et al.* Differential expression of microRNA-206 and its target genes in preeclampsia. *J Hypertens* 2015;**33**:2068–2074.

Anton L, Merrill DC, Neves LAA, Diz DI, Corthorn J, Valdes G, Stovall K, Gallagher PE, Moorefield C, Gruver C *et al.* The uterine placental bed renin-angiotensin system in normal and preeclamptic pregnancy. *Endocrinology* 2009;**150**:4316–4325.

Anton L, Olarerin-George AO, Schwartz N, Srinivas S, Bastek J, Hogenesch JB, Elovitz AB. miR-210 inhibits trophoblast invasion and is a serum biomarker for preeclampsia. *Am J Pathol* 2013;**183**:1437–1445.

Burcklé C, Bader M. Prorenin and its ancient receptor. *Hypertension* 2006;**48**:549–551.

Cai M, Kolluru GK, Ahmed A. Small molecule, big prospects: microRNA in pregnancy and its complications. *J Pregnancy* 2017;**2017**:6972732.

Choi S, Yun J, Lee OJ, Han HS, Yeo MK, Lee MA, Suh KS. MicroRNA expression profiles in placenta with severe preeclampsia using a PNA-based microarray. *Placenta* 2013;**34**:799–804.

Fatini C, Romagnuolo I, Sticchi E, Rossi L, Cellai AP, Rogolino A, Abbate R. ACE gene in pregnancy complications: Insights into future vascular risk. *Hypertens Pregnancy* 2016;**35**:62–72.

Forbes K. IGF Regulation of miR-483-3p expression in the developing human placenta. *Growth Horm IGF Res* 2012;**22**:16.

Forbes K, Westwood M, Baker PN, Aplin JD. Insulin-like growth factor I and II regulate the life cycle of trophoblast in the developing human placenta. *Am J Physiol Cell Physiol* 2008;**294**:1313–1322.

Goyal N, Yellon SM, Longo LD, Mata-Greenwood E. Placental gene expression in a rat 'model' of placental insufficiency. *Placenta* 2010;**31**:568–575.

Hromadnikova I, Kotlabova K, Ivankova K, Krofta L. First trimester screening of circulating C19MC microRNAs and the evaluation of their potential to predict the onset of preeclampsia and IUGR. *PLoS One* 2017;**12**:0171756.

Hromadnikova I, Kotlabova K, Ondrackova M, Kestlerova A, Novotna V, Hympanova L, Doucha J, Krofta L. Circulating C19MC microRNAs in preeclampsia, gestational hypertension, and fetal growth restriction. *Mediators Inflamm* 2013;**2013**:186041.

Itskovitz J, Rubattu S, Levron J, Sealey JE. Highest concentrations of prorenin and human chorionic gonadotropin in gestational sacs during early human pregnancy. *J Clin Endocrinol Metab* 1992;**75**:906–910.

Jairajpuri D, Malalla ZH, Mahmood N, Almawi WY. Circulating microRNA expression as predictor of preeclampsia and its severity. *Gene* 2017;**627**:543–548.

Lalevee S, Lapaire O, Buhler M. miR-455 is linked to hypoxia signaling and is deregulated in preeclampsia. *Cell Death Dis* 2014;**5**:1408–1416.

Laskowska M, Leszczynska-Gorzelak B, Laskowska K, Oleszczuk J. Evaluation of the renin-angiotensin-aldosterone system in pregnancy complicated by preeclampsia with and without intrauterine growth retardation. *Ann Univ Mariae Curie Sklodowska Med* 2004;**59**:e6.

Li J, Fu Z, Jiang H, Chen L, Wu X, Ding H, Xia Y, Wang X, Tang Q, Wu W. IGF2-derived miR-483-3p contributes to macrosomia through regulating trophoblast proliferation by targeting RB1CC1. *Mol Hum Reprod* 2018;**1**:444–452.

Liu L, Wang Y, Fan H, Zhao X, Liu D, Hu Y, Kidd AR 3rd, Bao J, Hou Y. MicroRNA-181a regulates local immune balance by inhibiting proliferation and immunosuppressive properties of mesenchymal stem cells. *Stem Cells* 2012;**30**:1756–1770.

Lu T, Lu W, Zhao LJ. MicroRNA-137 affects proliferation and migration of placenta trophoblast cells in preeclampsia by targeting ERRa. *Reprod Sci* 2017;**24**:85–96.

Lui S, Forbes K. miR-514: a novel regulator of growth factor signalling in the human placenta. *Placenta* 2012;**33**:117.

Luo R, Shao X, Xu P, Liu Y, Wang Y, Zhao Y, Liu M, Ji L, Li Y, Chang C et al. MicroRNA-210 contributes to preeclampsia by downregulating potassium channel modulatory factor 1. *Hypertension* 2014;**64**:839–845.

Luo L, Ye G, Nadeem L, Fu G, Yang BB, Honarparvar E, Dunk C, Lye S, Peng C. MicroRNA-378a-5p promotes trophoblast cell survival, migration and invasion by targeting Nodal. *J Cell Sci* 2012;**125**:3124–3132.

MacGregor G, Markandu ND, Roulston JE, Jones JC, Morton JJ. Maintenance of blood pressure by the renin-angiotensin system in normal man. *Nature* 1981;**291**:329–331.

Marques F, Campain AE, Tomaszewski M, Zukowska-Szczechowska E, Yang YH, Charchar FJ, Morris BJ. Gene expression profiling reveals renin mRNA overexpression in human hypertensive kidneys and a role for microRNAs. *Hypertension* 2011;**58**:1093–1098.

Nartita T, Ichihara A, Matsuoka K, Takai Y, Bokuda K, Morimoto S, Itoh H, Seki H. Placental (pro)renin receptor expression and plasma soluble (pro)renin receptor levels in preeclampsia. *Placenta* 2016;**37**:72–78.

Paul M, Poyan Mehr A, Kreutz R. Physiology of local renin-angiotensin systems. *Physiol Rev* 2006;**86**:747–803.

Peeters L, Vigne JL, Tee MK, Zhao D, Waite LL, Taylor RN. PPAR gamma represses VEGF expression in human endometrial cells: implications for uterine angiogenesis. *Angiogenesis* 2005;**8**:373–379.

Pineles B, Romero R, Montenegro D, Tarca AL, Han YM, Kim YM, Draghici S, Espinoza J, Kusanovic JP, Mittal P et al. Distinct subsets of microRNAs are expressed differentially in the human placentas of patients with preeclampsia. *Am J Obstet Gynecol* 2007; **196**:261–266.

Pringle K, Tadros MA, Callister RJ, Lumbers ER. The expression and localization of the human placental prorenin/renin-angiotensin system throughout pregnancy: roles in trophoblast invasion and angiogenesis? *Placenta* 2011;**32**:956–962.

Umemura K, Ishioka S, Endo T, Ezaka Y, Takahashi M, Saito T. Roles of microRNA-34a in the pathogenesis of placenta accreta. *J Obstet Gynaecol Res* 2013;**39**:67–74.

Wang Y, Lumbers E, Arthurs AL, Corbisier de Meaultsart C, Mathe A, Avery-Kiejda KA, Roberts CT, Broughton Pipkin F, Marques FZ, Morris BJ et al. Regulation of the human placental (pro)renin receptor-prorenin-angiotensin system by microRNAs. *Mol Hum Reprod* 2018; **24**:453–464.

molecular human reproduction

ORIGINAL ARTICLE

Genes upregulated in the amnion at labour are bivalently marked by activating and repressive histone modifications

Carolyn M. Mitchell[1,4], Jonathan J. Hirst[1,4], Murray D. Mitchell (iD) [3], Henry G. Murray[2,4], and Tamas Zakar (iD) [1,2,4,*]

[1]Mothers and Babies Research Centre, Hunter Medical Research Institute, New Lambton Heights, New South Wales 2305, Australia
[2]Department of Obstetrics and Gynaecology, John Hunter Hospital, New Lambton Heights, New South Wales 2305, Australia [3]Centre for Clinical Research, University of Queensland, Brisbane, Queensland 4029, Australia [4]Faculty of Medicine and Public Health, The University of Newcastle, Callaghan 2308, Australia

*Correspondence address. Mothers and Babies Research Centre, Hunter Medical Research Institute, New Lambton Heights, New South Wales 2305, Australia. E-mail: tamas.zakar@newcastle.edu.au (iD) orcid.org/0000-0002-1690-1159

Inflammatory genes are expressed increasingly in the foetal membranes at late gestation triggering birth. Here we have examined whether epigenetic histone modifications contribute to the upregulation of proinflammatory genes in the amnion in late pregnancy and at labour. Amnion samples were collected from early pregnancy, at term in the absence of labour and after spontaneous birth. The expression of the labour-associated proinflammatory genes PTGS2, BMP2 and NAMPT was determined by reverse transcription-coupled quantitative real-time PCR (qRT-PCR). Chromatin immunoprecipitation (ChIP) and sequential double ChIP were performed to determine the levels and co-occurrence of activating histone-3, lysine-4 trimethylation (H3K4me3) and repressive histone-3, lysine-27 trimethylation (H3K27me3) at the gene promoters. H3K4 methyltransferase, H3K27me3 demethylase and H3K27 methyltransferase expression was determined by qRT-PCR and immunofluorescence confocal microscopy. PTGS2, BMP2 and NAMPT expression was upregulated robustly between early pregnancy and term ($P < 0.05$). The promoters were marked bivalently by both the H3K4me3 and H3K27me3 modifications. Bivalence was reduced at term by the decrease of the H3K27me3-modified fraction of promoter copies marked by H3K4me3 indicating epigenetic activation. Messenger RNAs encoding the H3K4-specific methyl transferases MLL1,-2,-3,-4, SETD1A,-B and the H3K27me3-specific demethylases KDM6A,-B were expressed increasingly while the H3K27 methyl transferase EZH2 was expressed decreasingly at term. Histone modifying enzyme proteins were detected in amnion epithelial and mesenchymal cells. These results with prototypical proinflammatory genes suggest that nucleosomes at labour-promoting genes are marked bivalently in the amnion, which is shifted towards monovalent H3K4me3 modification at term when the genes are upregulated. Bivalent epigenetic regulation by histone modifying enzymes may control the timing of labour.

Key words: parturition / amnion / histone modifications / gene expression / epigenetic bivalency / histone-modifying enzymes

Introduction

Human parturition involves inflammatory processes that develop in the gestational tissues at the end of pregnancy (Osman, et al., 2003; Romero, et al., 2006). The inflammation is timed for term, controlled in intensity and coordinated in the foetal membranes, decidua, cervix, myometrium and the placenta. The strict regulation ensures that myometrial activation, cervical softening and membrane rupture happen at a time and in a sequence that are optimal for the mother and safely deliver a mature foetus. Many important details of the complex

inflammatory processes have been explored and documented (Challis, et al., 2009); however, critical issues such as the molecular mechanisms of timing, control of strength and interactions among the intrauterine tissues remain unclear.

High-throughput multidimensional data and single gene-focused studies have demonstrated that a distinct group of inflammatory genes is activated in the foetal membranes at term labour even in the absence of histological chorioamnionitis or microbial infection. This characteristic gene expression pattern has been described as an 'acute inflammation gene expression signature', which appears at term

leading to membrane remodelling and eventually membrane rupture coupled to the release of uterine muscle stimulants (Haddad, *et al.*, 2006). The mechanisms that suppress these genes during pregnancy and allow expression at term are undefined and may hold clues as to the control of the timing of labour.

Gene expression patterns in the developing foetus are controlled by epigenetic chromatin modifications. Cell lineage commitment and downstream cellular differentiation are accompanied by changing genome wide chromatin modification landscapes defining gene expression potential characteristic of cell identity (Roadmap Epigenomics, *et al.*, 2015). Two of the best-characterized epigenetic histone modifications are histone-3, lysine-4 trimethylation (H3K4me3), which marks transcriptionally active promoters, and histone-3, lysine-27 trimethylation (H3K27me3), which is associated with gene repression. The simultaneous presence of both modifications on a subset of promoters, called 'bivalent', was proposed to mark genes poised for activation or silencing when bivalency is resolved at subsequent stages of development (Vastenhouw and Schier, 2012). Recent work also suggests that epigenetic bivalency can occur in a variety of tissues and cells and its role is to fine-tune gene expression profiles by ensuring properly scheduled, coordinate and robust responses to regulatory cues (Voigt *et al.*, 2013).

Based on this information we reasoned that gene expression patterns in the extra-embryonic foetal tissues might be regulated by chromatin modifications similarly to the epigenetic mechanisms in the developing embryo. Specifically, we hypothesized that the H3K4me3 and H3K27me3 modifications participate in the control of proinflammatory genes suppressing expression during pregnancy and permitting expression at the time of labour. To test this hypothesis, we have selected three prototypical inflammatory genes implicated in the 'acute inflammatory gene expression signature'. *PTGS2* (Prostaglandin-Endoperoxide Synthase 2) is the gene encoding the rate limiting enzyme of prostaglandin biosynthesis, and prostaglandins produced in the amnion induce birth at any time of gestation (Olson, 2003). The protein encoded by *NAMPT* (Nicotinamide Phosphoribosyl Transferase) also called PBEF (Pre-B cell-enhancing factor or visfatin) in its secreted form, is a proinflammatory cytokine involved in the innate immune response (Sun, *et al.*, 2013). BMP2 (Bone Morphogenetic Protein 2), a TGFB (Transforming Growth Factor Beta) superfamily member, exhibits *in vivo* and *in vitro* proinflammatory actions and has a pivotal role in chorioamnionic development (Zhang and Bradley, 1996; Csiszar, *et al.*, 2006). All three genes are expressed in the amnion membrane at term (Teixeira, *et al.*, 1994; Ognjanovic and Bryant-Greenwood, 2002; Kim, *et al.*, 2005; Lappas, 2012). We have isolated amnion tissue from early gestations (12–16 weeks), at term (37–41 weeks) and following term spontaneous delivery and determined the levels and gestational changes of H3K4me3 and H3K27me3 modifications at the promoters of *PTGS2, BMP2* and *NAMPT/BPEF/*visfatin. We have correlated gene expression with H3K4me3 and H3K27me3 levels at the promoters. We have also performed sequential chromatin immunoprecipitations to detect co-localization of the two histone modifications at the same promoter copies and demonstrate genuine bivalency. Finally, we have determined whether enzymes capable of modifying H3K4me3 and H3K27me3 levels are expressed in the amnion. The presence of histone modifying enzymes raises the possibility that modification patterns are dynamic, may be influenced by the intrauterine environment and could be targeted by interventions.

Methods

Ethical approval

Informed written consent was provided by all women participating in the study. Approval for the project was granted by the Hunter New England Health Human Research Ethics Committee and the University of Newcastle Human Research Ethics Committee (Approval Number: 03/02/12/3.15).

Patients and tissue collection

Placentae with attached foetal membranes were collected at the John Hunter Hospital Maternity and Gynaecology Department, Newcastle, New South Wales, Australia, from women delivering at term (37–41 weeks) either by Caesarean section in the absence of labour or following spontaneous labour and delivery. Indications for Caesarean section were previous Caesarean delivery, breech presentation and placenta praevia. All pregnancies were singleton and uncomplicated otherwise. Women with induced labour, a history of genital tract infection, or treated with nonsteroidal anti-inflammatory drugs were excluded. Participants were free of clinical or histological chorioamnionitis. Amnion was isolated from the reflected membranes within 30 min of delivery as described (Mitchell and Powell, 1984; Johnson, *et al.*, 2002) and processed immediately for chromatin immunoprecipitation or frozen in liquid nitrogen for RNA extraction. Amnion tissues were also collected from women undergoing early elective termination between 10 and 18 weeks of pregnancy at a day-surgery.

RNA extraction and reverse transcription

These procedures have been described previously (Mitchell, *et al.*, 2008). In brief, total RNA was extracted from amnion tissue using TRIzol reagent (Life Technologies, Australia) according to the manufacturer's protocol. The RNA was purified using RNeasy Mini and RNAse-free DNAse kits (Qiagen, Australia). The quality of the purified RNA was assessed by agarose gel electrophoresis and the RNA was quantified using a NanoDrop 1000 UV spectrophotometer. The RNA was spiked with 10^7 copies/μg Alien RNA (Integrated Sciences, Australia) before reverse transcription using the Superscript III First-Strand Synthesis System with random hexamers (Life Technologies, Australia). Alien RNA is nonhomologous to any known RNA sequence and can serve as spiked-in reference RNA (Smith, *et al.*, 2003) eliminating the problem of the variable expression of endogenous reference RNAs when relative mRNA abundance is determined.

Chromatin immunoprecipitation and sequential ChIP

Chromatin immunoprecipitation (ChIP) was performed as described previously in detail (Mitchell, *et al.*, 2008). In brief, the reflected portion of amnion membranes were cut to $2 \times 2 \, cm^2$ pieces, blotted on filter paper, weighed and 1 g of tissue was fixed with 1% formaldehyde in 25 ml of Dulbecco's phosphate-buffered saline (DPBS) at room temperature for 20 min. Chromatin extracts (400 μl), were prepared from the nuclear fraction and 50 μl aliquots were processed for immunoprecipitation with validated rabbit polyclonal antibodies to histone H3, trimethyl-lysine-4, histone H3, trimethyl-lysine-27 or rabbit IgG (isotype-matched negative control) listed in Table S1 (online only). The immune complexes were absorbed to protein A-agarose, washed, eluted and the crosslinks were reversed. The immunoprecipitated DNA was purified using the Wizard SV gel and PCR clean-up kit (Promega, Alexandria, New South Wales, Australia) and target sequences were detected by quantitative real time PCR (qPCR). An aliquot of the chromatin extract was processed for crosslink reversal without immunoprecipitation to determine input.

For sequential ChIP, the antibody complexes were eluted from protein A-agarose after the first immunoprecipitation and washings (Mitchell, et al., 2008) by incubation at 37°C for 30 min with 25 ul of 10 mM Dithiothreitol (DTT) in re-ChIP buffer (1% Triton-X 100, 2 mM EDTA, 150 mM NaCl, 20 mM Tris–HCl pH 8.9). The elution was repeated with 25 μl re-ChIP buffer (without DTT). To the H3K4me3 eluates (50 μl), 5 μl histone H3, K4me3 Trimethyl Peptide (0.27 mg/ml, Sapphire Bioscience Pty Ltd, Redfern, New South Wales, Australia) was added followed by incubation at 37°C for 60 min. The mixtures were diluted to 500 μl with re-ChIP buffer (without DTT) and processed for the second immunoprecipitation, washes, elution and crosslink reversal as per the normal ChIP protocol (Mitchell et al. 2008). Separate first ChIP reactions served as the negative control of the second ChIP using rabbit IgG for the second immunoprecipitation. Further separate H3K4me3 and H3K27me3 first ChIP reactions were used to determine the input for the second ChIP, respectively, where crosslinks were reversed after the first ChIP by combining the protein A-agarose eluate (50 μl) with 1% sodium dodecyl sulphate (SDS), 0.1 M sodium hydrogen carbonate, 175 μg Proteinase K to 350 μl volume and incubating the mixture at 56°C for 1 h, then overnight at 65°C. DNA purification was performed subsequently using the Wizard SV gel and PCR clean-up kit (Promega, Alexandria, New South Wales, Australia) as described (Mitchell, et al., 2008).

Real-time PCR

Real-time PCR with SYBR® green detection was used to determine mRNA relative abundance in cDNA (qRT-PCR) and the levels of promoter sequences in ChIP-isolated DNA (qPCR) as described previously (Mitchell, et al., 2008; 2011). Primers were designed using ABI Primer Express 3.0. Primers to measure *PTGS2, BMP2, NAMPT, UTX/KDM6A* (Ubiquitously Transcribed Tetratricopeptide Repeat, X Chromosome/ Lysine Demethylase 6A), *JMJD3/KDM6B* (Jumonji Domain-Containing Protein 3/Lysine Demethylase 6B), *EZH2/KMT6A* (Enhancer Of Zeste 2 Polycomb Repressive Complex 2 Subunit/Lysine *N*-Methyltransferase 6), *MLL1/KMT2A* (Mixed Lineage Leukemia 1/Lysine methyltransferase 2A), *MLL2/KMT2D* (Myeloid/Lymphoid Or Mixed-Lineage Leukemia 2/Lysine Methyltransferase 2D), *MLL3/KMT2C* (Myeloid/Lymphoid Or Mixed-Lineage Leukemia 3/Lysine Methyltransferase 2C), *MLL4/KMT2B* (Myeloid/ Lymphoid Or Mixed-Lineage Leukemia Protein 4/Lysine Methyltransferase 2B), *SETD1A/KMT2F* (SET Domain-Containing Protein 1A/Lysine *N*-methyltransferase 2F), and *SETD1B/KMT2G* (SET Domain-Containing Protein 1B/ Lysine N-Methyltransferase 2G) mRNA abundance are listed in Table S2 (online only). Primers amplifying sequences within the *PTGS2, BMP2* and *NAMPT* gene promoters are also listed in Table S2. Primer concentrations and efficiencies were optimized according to Livak and Schmittgen (Livak and Schmittgen, 2001) and the efficiency of the primer pairs was validated using the LinReg PCR program (Ruijter, et al., 2009).

Isolation and culture of human amnion epithelial and mesenchymal cells

Amnion tissue was collected from term placentae following elective Caesarean section. The amnion epithelial cells were isolated as described previously (Bennett, et al., 1987) with minor modifications. Accordingly, amnion tissue strips were incubated in Ca^{2+}–Mg^{2+} free Hanks Balanced Salt Solution supplemented with 20 mM HEPES, pH 7.4 (HBSS) and 0.5 mM EDTA for 15 min at room temperature, rinsed and digested with 2.5 mg/ml dispase (Sigma-Aldrich, Castle Hill, Australia) in DMEM/F12 medium at 37°C for 45 min. The epithelial cells were released by vigorous shaking in growth medium (DMEM/F12 supplemented with 20 mM HEPES, pH 7.4, 10% foetal bovine serum and 40μg/ml gentamycin), isolated by centrifugation, resuspended and counted. To isolate amnion

mesenchymal cells, amnion tissue pieces were digested with 0.25% trypsin (Worthington TRL3704, 'ScimaR', Austraslia) in HBSS, 0.5 mM EDTA at 37°C for 30 min. The supernatant was discarded, and two further trypsin digestions were carried out in HBSS with and subsequently without EDTA. The tissue pieces were placed in growth medium to inactivate trypsin, then rinsed in serum-free medium and examined using phase contrast microscopy to confirm the removal of epithelial cells. Next, the tissue was incubated in 0.8 mg/ml Collagenase Type 4 and 0.4 mg/ml hyaluronidase (Worthington Biochemical, Lakewood, USA) in serum free growth medium at 37°C until full disintegration (2–3 h). The digest was filtered through a 100 μm cell strainer, cells were pelleted, resuspended in growth medium and counted. Viability of both cell types was over 95% by Trypan blue staining. Cells were distributed into 24-well plates containing plastic tissue culture slips (Thermanox, ProSciTech, Australia) at 2×10^5 cells/ well and incubated in growth medium for 40 h at 37°C in an atmosphere of 5% CO_2 in air.

Immunofluorescent confocal microscopy

Cell monolayers were washed twice with DPBS and fixed with 4% paraformaldehyde in phosphate buffered saline (PBS) for 20 min. After two washes with DPBS, 70% ethanol was added for short term storage (2–3 weeks) at 4°C. Subsequently, the cultures were rehydrated, rinsed with DPBS followed by antigen retrieval in 10 mM sodium citrate, pH 6.0, 0.05% Tween 20 at 90°C for 10 min. Cells were permeabilized with 0.1% Triton X-100 for 15 min, washed twice with DPBS, blocked with 1% bovine serum albumin (BSA) in PBS, 0.1% Triton X-100 for 1 h. The cells were incubated overnight at 4°C with histone modifying enzyme antibodies. Isoype-matched rabbit IgG and no-antibody (vehicle only) treatments were also included as negative controls. Antibody specifications and concentrations are listed in Table S1. Following overnight incubation at 4°C, the cells were washed with PBS five times and incubated for 2 h with the secondary antibody, Alexa Fluor® 488 goat anti-rabbit IgG (table S1). After seven washes with PBS, the culture slips were removed from the wells and mounted on glass slides using ProLong Diamond antifade with DAPI nuclear stain (Life Technologies Australia, Mulgrave) and coverslips. Fluorescent images were captured using a Nikon Eclipse 90i microscope equipped with confocal laser scanning accessories (C2si) controlled by the Confocal NIS Elements imaging software AR4.13.00. Z-stack imaging was performed to obtain optical sections. IgG isotype negative controls were imaged at the same settings (high voltage, pinhole, Look Up Table or LUT) as the primary antibody-treated slides to ensure specificity of detection.

Statistical analysis

Messenger RNA relative abundance values were calculated by the delta-Ct method (Livak and Schmittgen, 2001), distribution-tested and transformed, if necessary, to approach normal distribution. Data were subjected to one-way ANOVA followed by multiple comparisons with significance levels adjusted according to Bonferroni. Correlations between *PTGS2, BMP2* and *NAMPT* mRNA relative abundance in individual tissue samples were tested by Spearman's rank correlation analysis with Bonferroni correction of significance levels for multiple testing.

Chromatin immunoprecipitation data, expressed as recovery relative to input, were logarithmically transformed to achieve normal distribution. To identify promoter regions with peak histone methylation signal, repeated measures ANOVA was employed with promoter sites as the repeated measures variable. Post-estimation contrasts between adjacent promoter sites were subsequently performed with Sidak-adjusted significance levels for multiple testing. Gestational age- and labour-associated differences of histone methylation and methylation ratios were examined at the proximal promoter sites where the H3K4me3 peak was detected. We performed factorial ANOVA where input variables were promoter site and individual

samples nested into the gestational groups. H3K4me3:H3K27me3 ratios were calculated for each sample and processed for statistical analysis by factorial ANOVA. Sequential chromatin immunoprecipitation results were expressed as recovery after the second ChIP relative to the first ChIP input. Two to four sites within the proximal promoter marked by H3K4me3 were included in the sequential ChIP analysis by factorial ANOVA where gestational age- and labour-associated differences were tested as described. Immunoreactive histone modifying enzyme protein levels were assessed by counting immunostained cells on the confocal images presented in Fig. 6A–D and Figs S1–S6 (online only) and calculating the proportion of Alexa Fluor® 488-immunostained cells to DAPI-stained nuclei representing the total cell counts (×100 to obtain % values in Table I). Staining intensity was not assessed, only the presence or absence of staining as a binary variable. The proportion (frequency) of stained cells were compared between the epithelial and mesenchymal cells by Fisher's exact test. In all statistical evaluations $P < 0.05$ was considered significant after appropriate adjustments for multiple testing.

Results

PTGS2, BMP2 and *NAMPT* gene expression in the amnion in early pregnancy, at term and after spontaneous term labour

PTGS2, BMP2 and *NAMPT* gene expression was determined by measuring mRNA abundance in the amnion tissue samples using real-time qRT-PCR. Early pregnancy samples were obtained at 15.1 ± 2.5 weeks ($N = 7$), while term not in labour and after term labour tissues were collected at 38.8 ± 0.4 ($N = 16$) and 40.2 ± 0.9 ($N = 9$) weeks of gestation (mean $\pm$ SD), respectively. The small difference between the mean gestational ages of the term not in labour and after term labour groups was significant ($P = 0.0009$, *t*-test). Box plots in Fig. 1A–C

show that the levels of all three mRNAs increased markedly in the term not in labour samples compared to tissues from early gestation (130-, 8.3- and 9.4-fold increase of mean *PTGS2, BMP2* and *NAMPT* mRNA levels, respectively). In addition, there was a further significant 2-fold rise of *PTGS2* mRNA abundance after term labour, while the labour-associated increases did not reach statistical significance in the case of the *BMP2* and *NAMPT* mRNAs. Furthermore, *PTGS2, BMP2* and *NAMPT* mRNA abundance was highly correlated in individual tissues (Fig. 1D). These results demonstrated that *PTGS2, BMP2* and *NAMPT* gene expression increased robustly in the amnion with advancing gestation and the upregulation was coordinated in individuals as shown by the correlated mRNA levels.

Histone modifications at the *PTGS2, BMP2* and *NAMPT* promoter regions

Genome-wide studies have established that the promoters of most transcriptionally active genes are marked by H3K4 trimethylation of the associated nucleosomes (Guenther, *et al.*, 2007). Chromatin immunoprecipitation results in Fig. 2A–C show that nucleosomes at the promoter regions of the *PTGS2, BMP2* and *NAMPT* genes were trimethylated on H3K4 ($P < 0.0001$ vs IgG isotype control, Wilcoxon's signed-rank test; $N = 13$ for *PTGS2* with early pregnancy = 5, term not in labour = 5, after term labour = 3; $N = 12$ for *BMP2* with early pregnancy = 4, term not in labour = 5, after term labour = 3; $N = 16$ for NAMPT with early pregnancy = 5, term not in labour = 6, after term labour = 5). Furthermore, significantly higher H3K4me3 levels were detected at the proximal promoters (within 1000 base pairs in 5′ direction relative to the transcriptional start site, denoted by boxes in Fig. 2A–C) than in the further upstream 5′ regions. The levels of the repressive histone modification, H3K27me3, were also determined by

Table I Immunofluorescent detection of histone modifying enzymes in primary amnion epithelial and mesenchymal cells.

Enzyme	Immunostained/Total cells (%)		P^a	Localization
	Epithelial	**Mesenchymal**		
EZH2/KMT6A	2/142 (1.4)	0/278 (0)	NS	Nuclear in two epithelial cells (boxed)
UTX/KDM6A	49/484 (10.1)	16/117 (13.7)	NS	Faint extranuclear staining in both cell types
JMJD3/KDM6B	20/155 (12.9)	20/166 (12.1)	NS	Faint extranuclear staining in epithelial and speckled nuclear staining (arrows) in mesenchymal cells
MLL1/KMT2A	126/155 (81.3)	19/74 (25.7)	<0.01	Extranuclear in both cell types
MLL2/KMT2D	56/104 (53.9)	0/163 (0)	<0.01	Extra- and intra-nuclear (arrows) in epithelial cells
MLL3/KMT2C	143/218 (65.6)	109/144 (75.7)	NS	Extranuclear in both cell types and nuclear in a few mesenchymal cells (arrows)
MLL4/KMT2B	122/176 (69.3)	57/91 (62.6)	NS	Extranuclear in both cell types
SETD1A/KMT2F	67/150 (44.7)	23/116(19.8)	<0.01	Extranuclear in both cell types
SETD1B/KMT2G	64/205 (31.2)	2/74 (2.7)	<0.01	Extranuclear in epithelial and mesenchymal (boxed) cells
IgG	0/296 (0)	0/120 (0)	NS	

[a]Significance was tested by Fisher's exact test for comparing the frequency of immunostained epithelial and mesenchymal cells. Total cell numbers represent DAPI-stained nuclei. Data were derived from the confocal images presented in Fig. 6A–D and 8–12 (online only). Antibodies are listed in Table I (online only). The experiment was replicated twice with consistent results. NS, not significant difference. EZH2/KMT6A, Enhancer of Zeste 2 Polycomb Repressive Complex 2 Subunit/Lysine *N*-Methyltransferase 6; UTX/KDM6A, Ubiquitously Transcribed Tetratricopeptide Repeat, X Chromosome/Lysine Demethylase 6A; JMJD3/KDM6B, Jumonji Domain-Containing Protein 3/Lysine Demethylase 6B; MLL1/KMT2A, Mixed Lineage Leukemia 1/Lysine Methyltransferase 2A; MLL2/KMT2D, Myeloid/Lymphoid Or Mixed-Lineage Leukemia 2/Lysine Methyltransferase 2D; MLL3/KMT2C, Myeloid/Lymphoid Or Mixed-Lineage Leukemia 3/Lysine Methyltransferase 2C; MLL4/KMT2B, Myeloid/Lymphoid Or Mixed-Lineage Leukemia Protein 4/Lysine Methyltransferase 2B; SETD1A/KMT2F, SET Domain-Containing Protein 1A/Lysine *N*-methyltransferase 2F); SETD1B/KMT2G, SET Domain-Containing Protein 1B/Lysine *N*-Methyltransferase 2G,
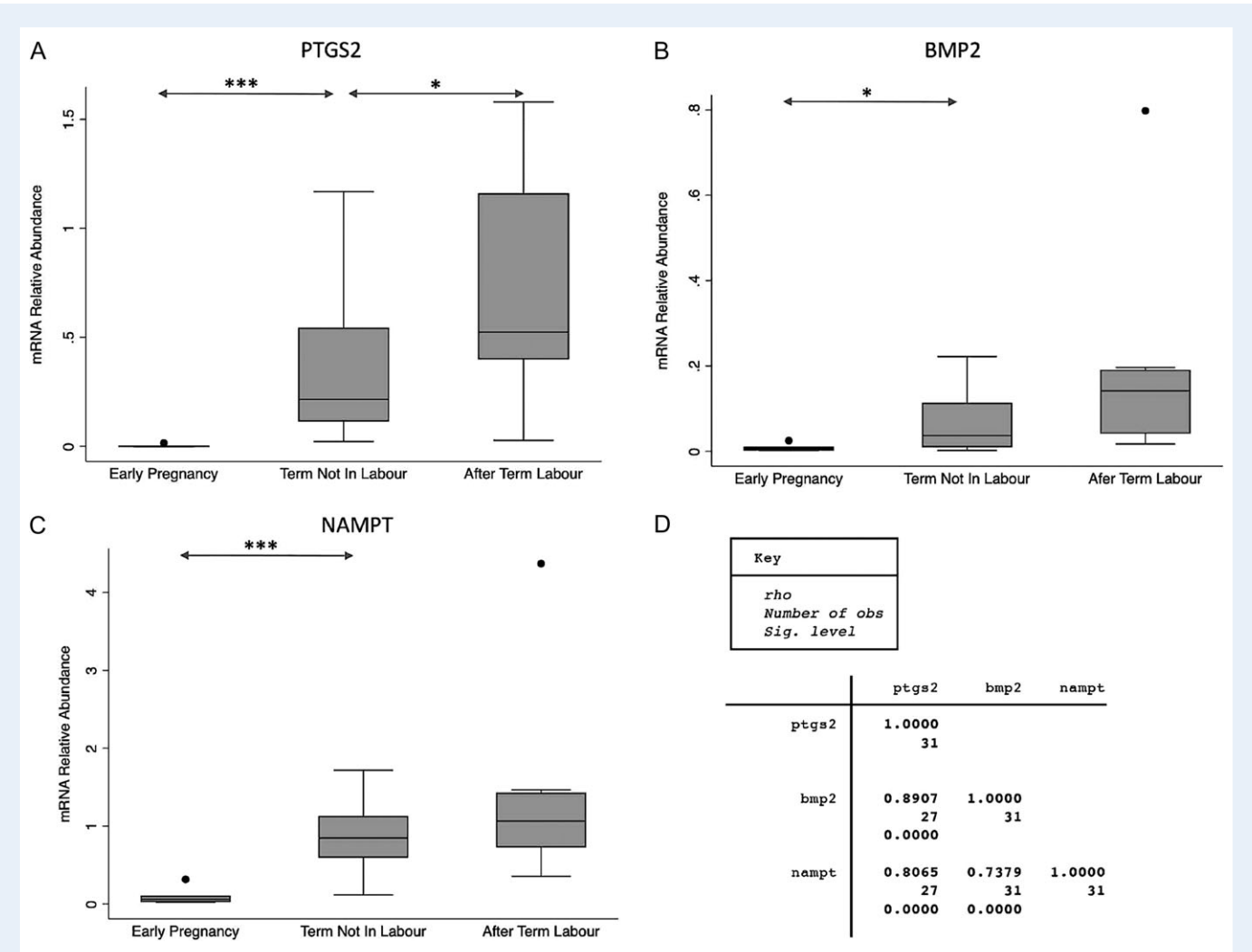
Figure 1 Box plots showing *PTGS2* (A), *BMP2* (B) and *NAMPT* (C) mRNA relative abundance in amnion tissue collected at early pregnancy (mean ± SD: 15.1 ± 2.7 weeks, *N* = 7), at term not in labour (38.8 ± 0.4 weeks, *N* = 16) and after term labour (40.2 ± 0.9 weeks *N* = 9). (**D**) Spearman correlations (rho) of *PTGS2*, *BMP2* and *NAMPT* mRNA abundance in the indicated number of individual tissues where matched observations were available. Group differences were determined by one-way ANOVA of transformed, normally distributed data. Significance was adjusted for multiple comparisons according to Bonferroni. *$P < 0.05$; ***$P < 0.001$. *PTGS2*, Prostaglandin-Endoperoxide Synthase 2; *BMP2*, Bone Morphogenetic Protein 2; *NAMPT*, Nicotinamide Phosphoribosyl Transferase.

a specific ChIP assay (Margueron and Reinberg, 2011). Marking by H3K27me3 was significant throughout the scanned regions compared to IgG isotype controls ($P < 0.0001$, Wilcoxon's signed rank test) including the proximal promoters marked by high levels of H3K4me3 (Fig. 2A–C).

The occurrence of the activating, H3K4me3, and the repressive, H3K27me3, modifications at the proximal promoters suggested that their relative levels might control gene activity. We have addressed this possibility by comparing H3K4me3 and H3K27me3 levels and their ratios in the early pregnancy, term not in labour and after term labour groups. Figure 3A–F illustrates the gestational differences detected. Trimethylation at H3K4 and H3K27 increased significantly at the *PTGS2* promoter between early pregnancy and term and H3K27, but not H3K4, trimethylation decreased with term labour (Fig. 3A). The only significant change at the *BMP2* promoter was an increase of H3K4 trimethylation with labour (Fig. 3C). At the *NAMPT* promoter,

H3K4 and H3K27 trimethylation decreased between early pregnancy and term, while H3K4 trimethylation increased with labour (Fig. 3E). These differences were reflected by the ratios of H3K4me3 to H3K27me3 levels at the three promoters showing no significant change at late vs early gestation and increasing with labour (Fig. 3B, D and F). Overall, the results indicated that histone methylations were dynamic, but the differences in the methylation levels were not in agreement with the gene expression changes, particularly with the strong increases at term (not in labour) compared to early pregnancy (Fig. 1A–C).

Bivalent histone modifications at the *PTGS2*, *BMP2* and *NAMPT* promoters

Bivalent promoters are characterized by the coexistence of the activating, H3K4me3, and the repressive, H3K27me3, modifications at the
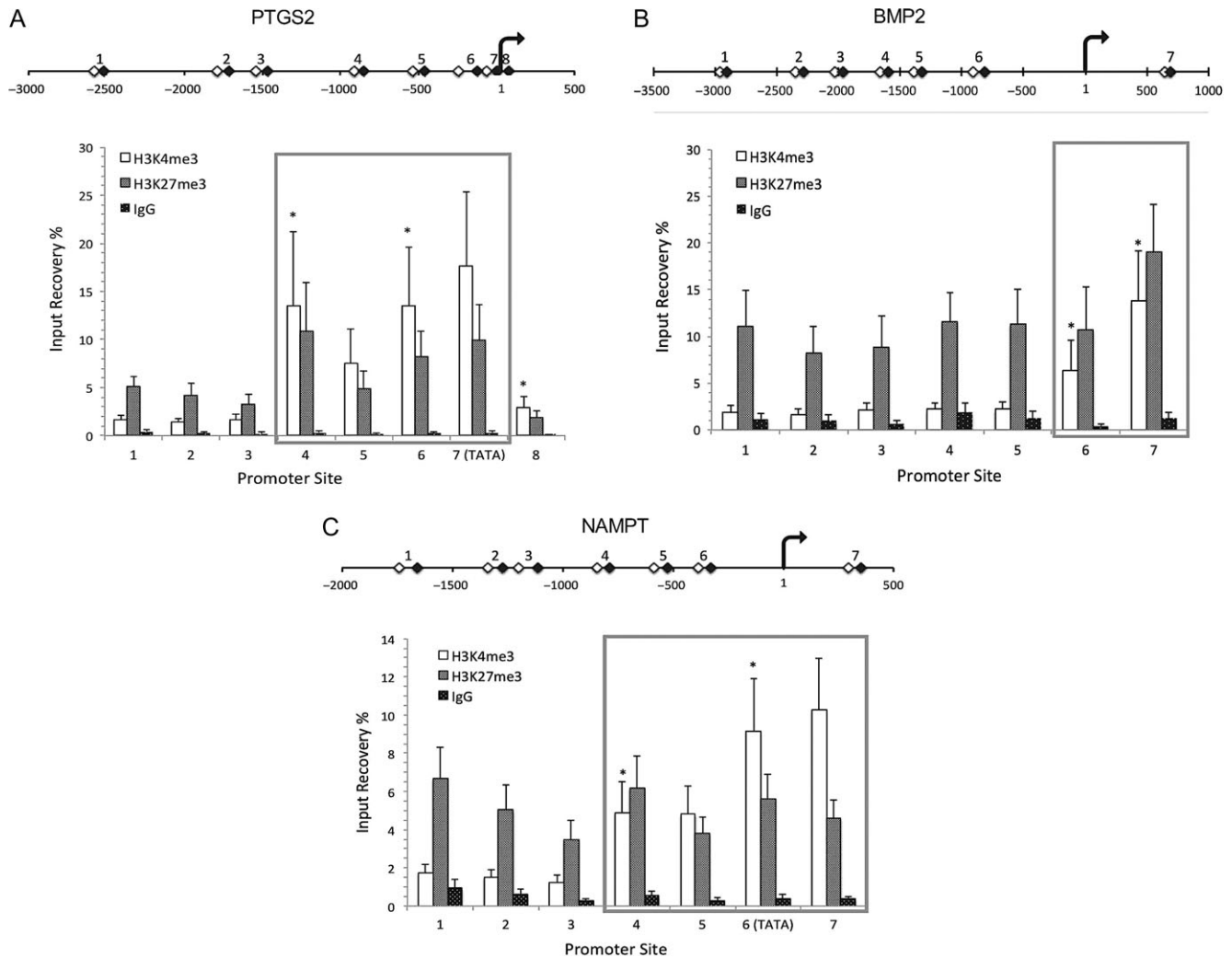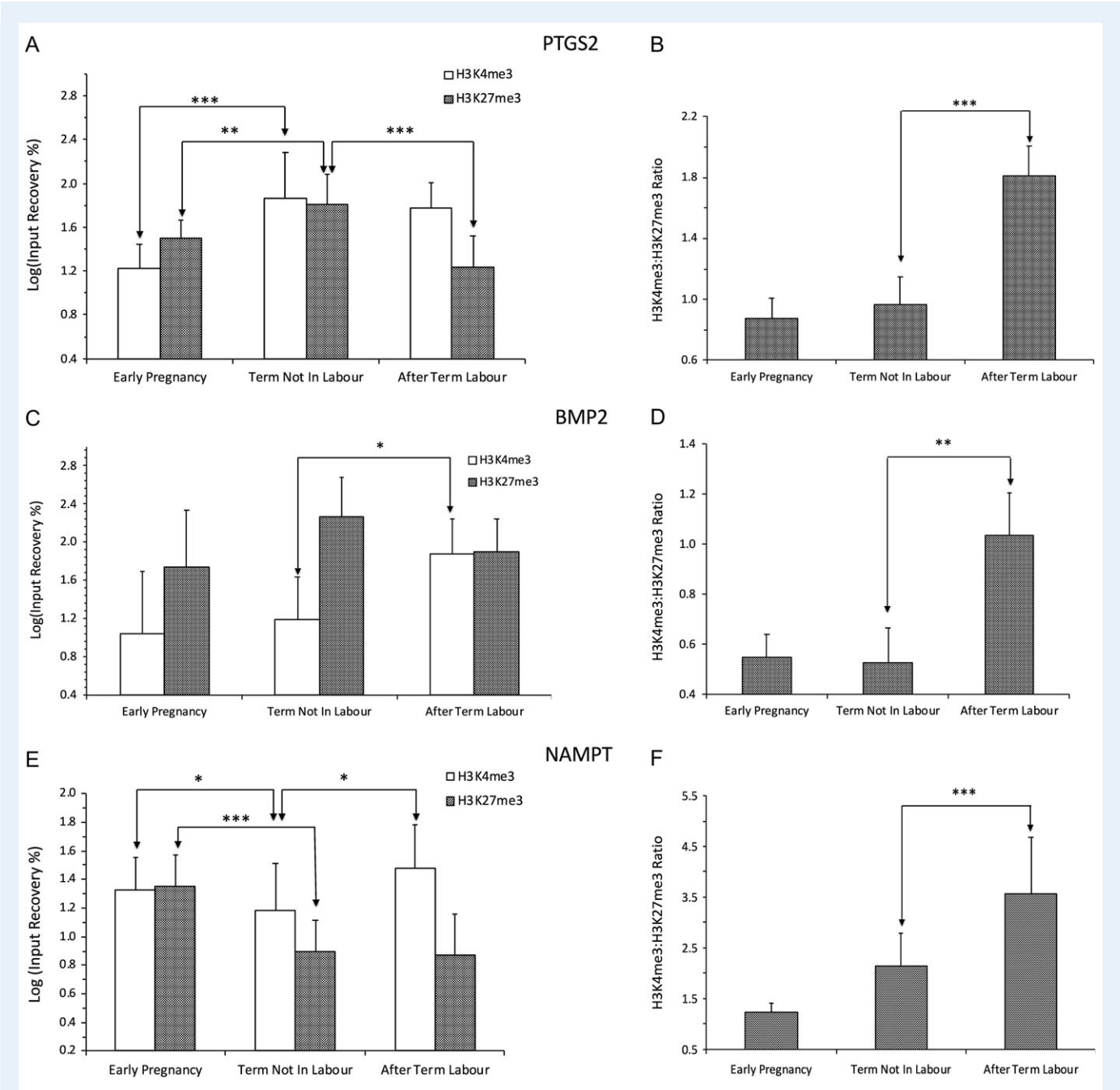
Figure 2 Histone 3, lysine 4 trimethylation (H3K4me3) and histone 3, lysine 27 trimethylation (H3K27me3) at the *PTGS2* (A), *BMP2* (B) and *NAMPT* (C) gene promoters, determined by chromatin immunoprecipitation and real-time quantitative polymerase chain reaction (ChIP-qPCR). The outlines above the diagrams show the numbers and positions of the promoter sites detected by qPCR in ChIP-isolated DNA. Nucleotide numbers are indicated relative to the transcription initiation sites (+1), which are marked by arrows. The open and closed diamonds denote the positions of the forward and reverse primers, respectively. PCR amplicons that include TATA sites are also indicated. Proximal promoter regions identified by increased H3K4me3 modification levels are boxed. Asterisks denote significant differences of H3K4me3 levels compared to the neighbouring 5′-positioned amplicon ($P < 0.05$, repeated measures ANOVA with Sidak-adjustment for multiple testing. $N = 13$ (early pregnancy: 5; term not in labour: 5; after term labour: 3), 12 (early pregnancy: 4; term not in labour: 5; after term labour: 3), and 16 (early pregnancy: 5; term not in labour: 6; after term labour: 5) patients for *PTGS2*, *BMP2* and *NAMPT*, respectively.

same promoter copies. Bivalent promoters exhibit low baseline transcriptional activity and robust, coordinated responses to developmental cues accompanied by the loss of either the repressive or the activating modification (Vastenhouw and Schier, 2012; Voigt, et al., 2013). We have explored promoter bivalency at the *PTGS2, BMP2* and *NAMPT* genes by sequential ChIP, which consists of a first immunoprecipitation with a H3K4me3- or H3K27me3-specific antibody and processes the immunoprecipitated chromatin as the input for a second ChIP with a H3K27me3- or H3K4me3-specific antibody, respectively. Recovery after the second chromatin immunoprecipitation represents the bivalently modified fraction of the H3K4me3- or H3K27me3-marked input. Figure 4A, C and E show the results of sequential ChIP

with H3K4me3 as the first and H3K27me3 as the second immunoprecipitation performed at the *PTGS2*, *BMP2* and *NAMPT* proximal promoters, respectively. Results of the reverse design, with H3K27me3 as the first and H3K4me3 as the second immunoprecipitation, are presented in Fig. 4B, D and F. Bivalency was significant at the three promoters in both sequential ChIP directions ($P < 0.001$ relative to the IgG isotype control, Wilcoxon's signed-rank test). The level of H3K27me3 marking in the H3K4-trimethylated fraction decreased significantly at term compared to early pregnancy at all three promoters, while labour was associated with a significant rise of H3K27me3 levels in the H3K4me3-modified fractions (Fig. 4A, C and E). H3K4-trimethylation in the H3K27-trimethylated promoter fractions showed

Figure 3 **Histone 3, lysine 4 trimethylation (H3K4me3) and histone 3, lysine 27 trimethylation (H3K27me3) at the *PTGS2*, *BMP2* and *NAMPT* promoters in early pregnancy, at term and after term labour.** (**A**, **C**, **E**) Levels of histone 3, lysine 4 trimethylation (H3K4me3) and histone 3, lysine 27 trimethylation (H3K27me3) at the *PTGS2* (A), *BMP2* (C) and *NAMPT* (E) proximal promoter regions in early pregnancy, at term not in labour and after term labour. (**B**, **D**, **F**) Ratios of histone 3, lysine 4 trimethylation (H3K4me3) levels to histone 3, lysine 27 trimethylation (H3K27me3) levels at the *PTGS2* (B), *BMP2* (D) and *NAMPT* (F) proximal promoter regions in early pregnancy, at term not in labour and after term labour. Data obtained with PCR amplicons within the proximal promoter regions of each gene (shown by boxes in Fig. 2) were pooled and analysed by factorial ANOVA. Columns show means ± SE; $N = 4$–5 in early pregnancy, $N = 5$–6 at term not in labour, $N = 3$–5 after term labour). *$P = 0.05$; **$P < 0.01$; ***$P < 0.001$.

no significant gestational change (Fig. 4B, D and F). Collectively, these results indicate significantly reduced bivalency at term toward single marking with the activating H3K4me3 modification compared to early pregnancy. Term labour, on the other hand, was associated with an increase of bivalency as indicated by the higher level of H3K27me3 among the H3K4me3-marked promoters.
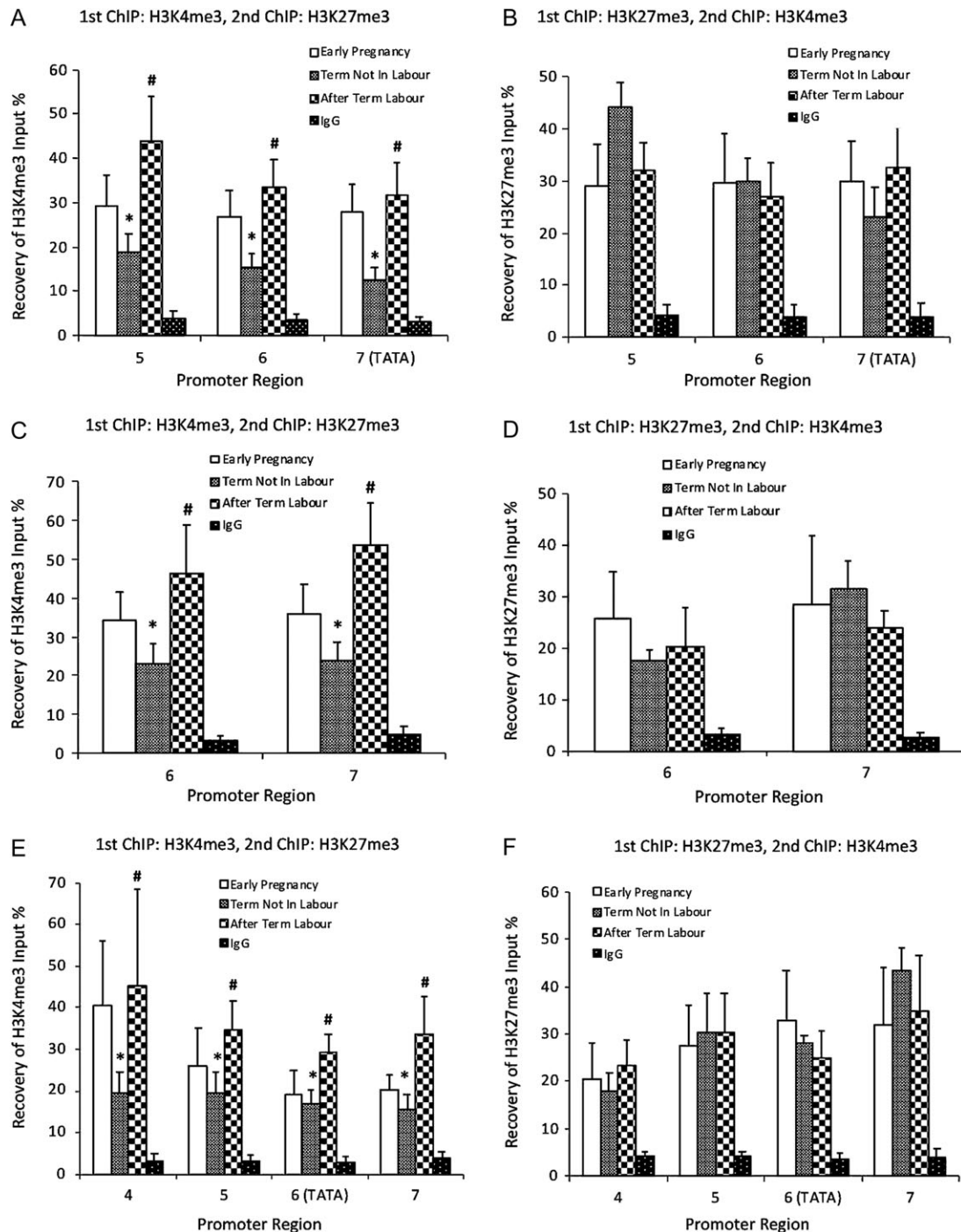
Figure 4 Sequential double ChIP showing co-occurrence of the H3K4me3 and H3K27me3 modifications at the *PTGS2* **(A, B)**, *BMP2* **(C, D)** and *NAMPT* **(E, F)** promoters in early pregnancy, at term not in labour and after term labour. (**A**, **C**, **E**) first ChIP was performed with H3K4me3 antibody followed by second ChIP with H3K27me3 antibody using the H3K4me3 ChIP-isolated chromatin fraction as input. (**B**, **D**, **F**) First ChIP was performed with H3K27me3 antibody followed by second ChIP with H3K4me3 antibody using the H3K27me3 ChIP-isolated chromatin fraction as input. Data obtained with PCR amplicons within the proximal promoter regions (numbered as in Fig. 2), were pooled for analysis by factorial ANOVA. Columns show means ± SE; ($N = 4$ in early pregnancy, $N = 5$ at term not in labour, $N = 3$ after term labour). *$P < 0.05$ between early pregnancy and term not in labour; [#]$P < 0.05$ between term not in labour and after term labour. IgG, isotype-matched IgG negative control.

Expression of histone modifying enzymes

Histone modifying enzyme expression was assessed at the mRNA level by real-time qRT-PCR. As shown in Fig. 5A, six lysine methyl-transferases capable of methylating H3K4 (*SETD1A/KMT2F, SETD1B/KMT2G, MLL1/KMT2A, MLL2/KMT2D, MLL3/KMT2C, MLL4/KMT2B*) (Schuettengruber, *et al.*, 2011; Bogershausen, *et al.*, 2013) were detected in the amnion tissue. The expression of all six methyl transferase-encoding mRNAs were higher at term than in early pregnancy. Term labour was associated with significant decrease of H3K4 methyltransferase expression except for *MLL2* mRNA. The level of the mRNA encoding the H3K27-specific methyltransferase *EZH2/KMT6A* (Gall Troselj, *et al.*, 2016) was relatively low and decreasing with advancing pregnancy and labour (Fig. 5B). The expression of mRNAs of the two H3K27me3-specific histone demethylases, *UTX/KDM6A* and *JMJD3/KDM6B*, (Agger, *et al.*, 2007; De Santa, *et al.*,

2007) was also detected in the amnion tissue samples (Fig. 5C). The abundance of *UTX/KDM6A* and *JMJD3/KDM6B* mRNAs increased at term compared to early pregnancy without significant change with term labour. Histone modifying enzyme proteins were detected by immunofluorescence in primary cultures of amnion epithelial and mesenchymal cells. Intracellular localization of the enzyme proteins was assessed by confocal z-stack imaging. Table I summarizes the immuno-detection results, and representative optical sections are presented in Fig. 6A–D and Figs S1–S6. EZH2/KMT6A protein was undetectable in mesenchymal cells and was detected at low (1.4%) frequency in epithelial cells in agreement with the low abundance of the corresponding mRNA (Table I, Figs 6A and 5B). UTX/KDM6A and JMJD3/KDM6B protein occurred in 10.1–13.7% of both cell types with speckled nuclear localization of JMJD3/KDM6B in some mesenchymal cells (Table I and Figs S4 and S5). The six H3K4 methyltransferases were
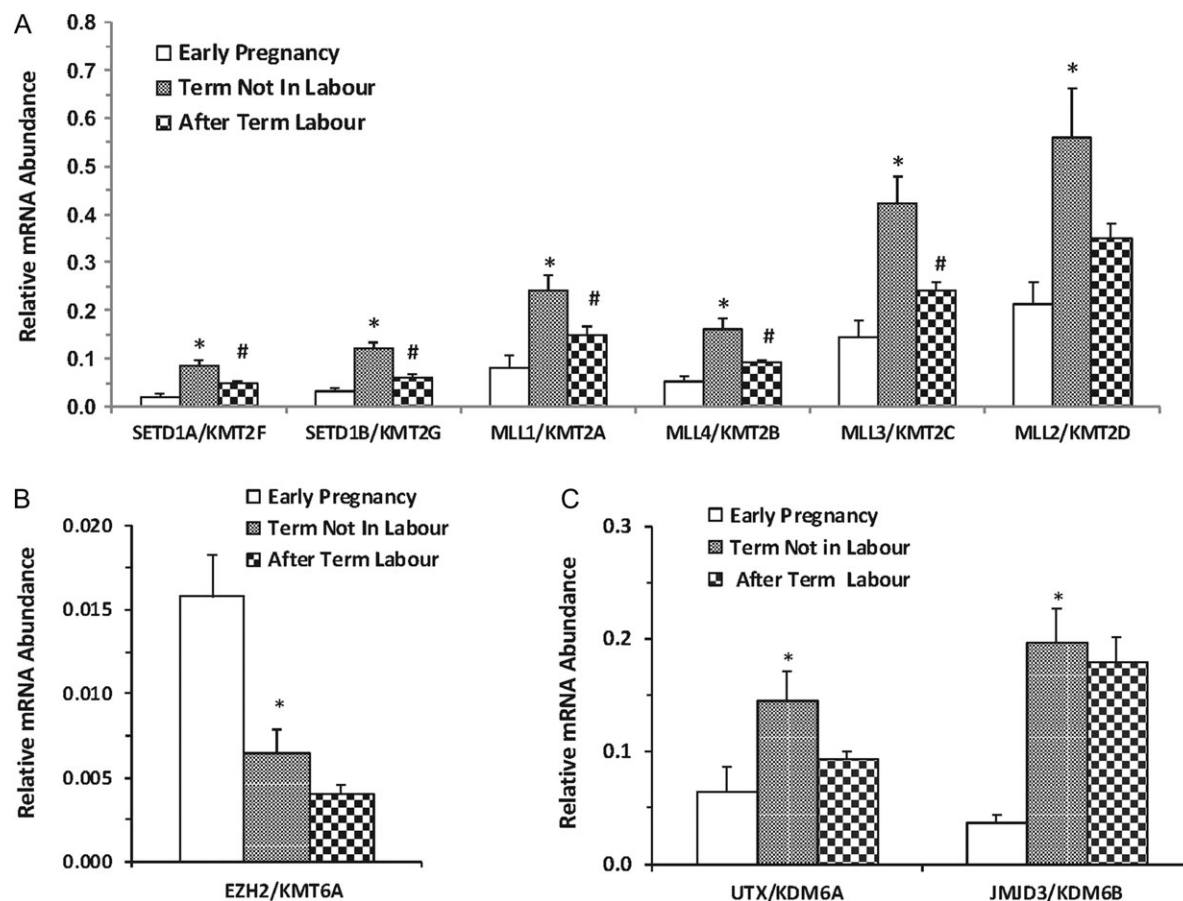
Figure 5 Expression of H3K4 methyl transferases (A), H3K27 methyltransferase (B) and H3K27me3 demethylases (C) in early pregnancy, at term not in labour and after term labour. Columns show means ± SE of mRNA relative abundance; ($N = 6$ in early pregnancy, $N = 9$ at term not in labour, $N = 8$ after term labour). *$P < 0.05$ between early pregnancy and term not in labour; #$P < 0.05$ between term not in labour and after term labour by ANOVA. SETD1A/KMT2F, SET Domain-Containing Protein 1A/Lysine N-Methyltransferase 2F); SETD1B/KMT2G, SET Domain-Containing Protein 1B/Lysine *N*-Methyltransferase 2G; MLL1/KMT2A, Mixed Lineage Leukemia 1/Lysine Methyltransferase 2A; MLL4/KMT2B, Myeloid/Lymphoid Or Mixed-Lineage Leukemia Protein 4/Lysine Methyltransferase 2B; MLL3/KMT2C, Myeloid/Lymphoid Or Mixed-Lineage Leukemia 3/Lysine Methyltransferase 2C; MLL2/KMT2D, Myeloid/Lymphoid Or Mixed-Lineage Leukemia 2/Lysine Methyltransferase 2D; EZH2/KMT6A, Enhancer Of Zeste 2 Polycomb Repressive Complex 2 Subunit/Lysine *N*-Methyltransferase 6; UTX/KDM6A, Ubiquitously Transcribed Tetratricopeptide Repeat, X Chromosome/Lysine Demethylase 6A; JMJD3/KDM6B, Jumonji Domain-Containing Protein 3/Lysine Demethylase 6B.

detected in the epithelial cells at frequencies between 31.2 and 81.3% (Table I). Localization was extranuclear except for MLL2/KMT2D, which showed nuclear staining in a few cells (Fig. 6B–D and Figs S1–S3). In mesenchymal cells, H3K4 methyltransferase immunoreactivity occurred at 2.7–75.7% frequency, except for MLL2/KMT2D, which was undetectable (Table I). MLL1/KMT2A, MLL2/KMT2D, SETD1A/KMT2F and SETD1B/KMT2G proteins were found in epithelial cells at significantly higher frequency than in mesenchymal cells (Table I) suggesting that the mRNAs in the amnion tissue samples were mostly of epithelial origin) (Fig. 5A). Localization in mesenchymal cells was extranuclear except for MLL3/KMT2C, which co-localized with nuclei in some cells (Fig. 6B—D and Figs S1–S3).

Discussion

In this study we report for the first time that trimethylation of histones at H3K4 and H3K27 occurs at the proximal promoter of labour-associated inflammatory genes in the foetal membranes. We also report that histones at these gene promoters are bivalently modified by H3K4me3 and H3K27me3 and that resolution of bivalency favoring activation occurs before term labour. Although our experiments involved just three labour-associated genes in the amnion membrane, the results suggest that characterization of histone modifications genome wide may reveal epigenetic mechanisms that control gene expression in the gestational tissues during pregnancy to ensure the correct timing of labour. Disruption of this regulatory mechanism may contribute to pregnancy disorders such as preterm birth.

Our data show that the expression of the labour-associated inflammatory genes *PTGS2, BMP2 and NAMPT* increases robustly in the amnion between early gestation (12–16 weeks) and term (37–41 weeks) before labour (Fig. 1). *PTGS2* expression increased further with term labour as reported before (Hirst, *et al.*, 1995), while the labour-associated change of *NAMPT* mRNA levels was not significant confirming previous results with full thickness membranes (Ognjanovic and Bryant-Greenwood, 2002). We found no labour-associated difference in *BMP* mRNA levels in the amnion (Fig. 1) despite a significant
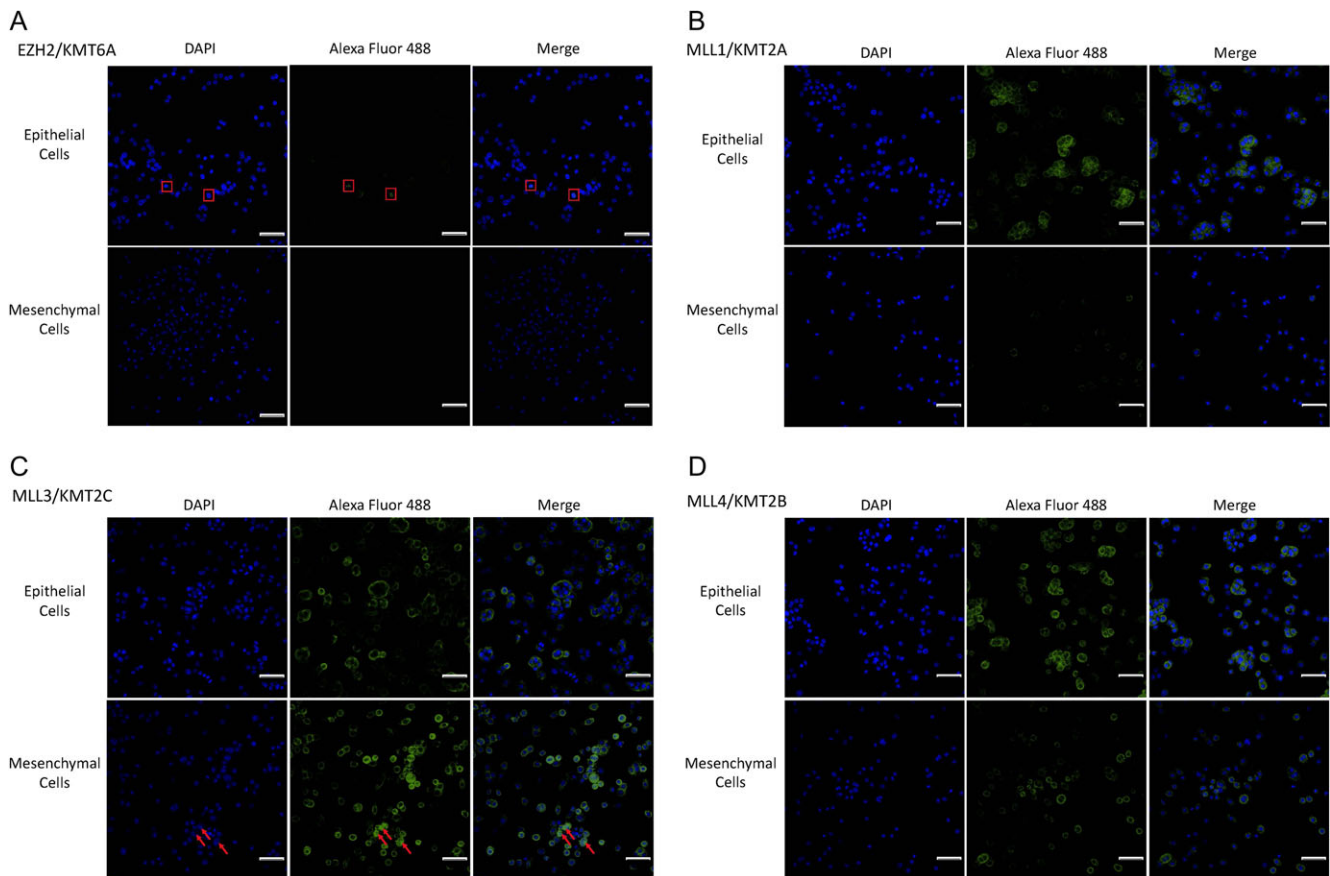
Figure 6 **Immunofluorescent confocal image of EZH2/KMT6A (A), MLL1/KMT2A (B), MLL3/KMT2C (C) and MLL4/KMT2B (D) expression in an optical section of amnion epithelial and mesenchymal cells in primary culture.** Nuclei were visualized using DAPI (blue) and EZH2 protein was detected using a primary antibody and Alexa Fluor 488-conjugated secondary antibody (green) (Table S1, online only). Co-localization is shown in the merged image. The red boxes in (A) and the red arrows in (C) highlight epithelial cell nuclei with EZH2 and mesenchymal cell nuclei with MLL3 present, respectively. Size bars are 50 μm. EZH2/KMT6A, Enhancer of Zeste 2 Polycomb Repressive Complex 2 Subunit/Lysine N-Methyltransferase 6; MLL1/KMT2A, Mixed Lineage Leukemia 1/Lysine Methyltransferase 2A; MLL3/KMT2C, Myeloid/Lymphoid Or Mixed-Lineage Leukemia 3/Lysine Methyltransferase 2C; MLL4/KMT2B, Myeloid/Lymphoid Or Mixed-Lineage Leukemia Protein 4/Lysine Methyltransferase 2B.

increase in unseparated full thickness membranes (Kim, *et al.*, 2005), which might reflect differential regulation in foetal membrane components. We have demonstrated previously that the increase of *PTGS2* mRNA level in the amnion during pregnancy is due to increasing gene transcription and that the transcriptional activity of the *PTGS2* gene does not change with term labour (Johnson, *et al.*, 2006). The upregulation of *PTGS2* mRNA abundance at labour was predominantly post-transcriptional in agreement with the involvement of microRNAs in the control of amnion *PTGS2* expression at term (Kim, *et al.*, 2011). Similar analyses of *NAMPT* and *BMP2* gene activities in the amnion have not been reported yet; however, it is reasonable to conjecture that the transcription of these labour-associated genes is induced mainly before labour.

Epigenetic chromatin modifications establish cell specific gene expression patterns during development (Xie, *et al.*, 2013) and may control gene activity during gestation (Lins and Mitchell, 2008). Methylation of CpG dinucleotides of DNA is an extensively characterized chromatin modification that represses gene activity (Attwood, *et al.*, 2002). The *PTGS2, BMP2* and *NAMPT* promoters overlap with high CpG-frequency genomic elements called 'CpG islands', which are generally unmethylated in promoters (Weber, *et al.*, 2007). In agreement with this, we have shown that the majority of *PTGS2, BMP2 and NAMPT* promoter copies in amnion tissue is methylated at low density (Mitchell, *et al.*, 2013), which did not change between early gestation and term labour. This suggests that promoter DNA methylation is not a pivotal mechanism controlling *PTGS2, BMP2* and *NAMPT* expression in this tissue (Mitchell, *et al.*, 2013). In the present study we focused on two histone methylation marks that have key importance in epigenetic gene expression control. High levels of the H3K4me3 modification mark transcriptionally active promoters (Guenther, *et al.*, 2007), and this mark was present at the proximal promoters of the three labour-associated genes during pregnancy and with labour. The H3K27me3 modification is associated with gene repression (Margueron and Reinberg, 2011), and this mark was also detected at the gene promoters during gestation. The H3K4me3 to H3K27me3 ratios remained unaltered between early and late gestation and increased with labour at all three promoters, which was at odds with the observed changes in gene expression, particularly the strong increase of the mRNA abundances in late vs early pregnancy. The results, therefore, did not support the possibility that the H3K4me3 and H3K27me3 modifications controlled *PTGS2, BMP2* or *NAMPT* gene activity independently or by their relative levels in the amnion cells.

An alternative possibility was that the two histone marks co-localized and interacted at the same promoter copies as described for bivalent genes in embryonic stem cells and some differentiated cells (Roh, *et al.*, 2006; Vastenhouw and Schier, 2012). Gene activity is low if a promoter is bivalent, but if bivalency is resolved by the removal of either the activating or the repressive mark, gene expression diminishes or increases, respectively (Roh, *et al.*, 2006; Pan, *et al.*, 2007). Sequential ChIP first with a H3K4me3 antibody followed by a second immunoprecipitation with a H3K27me3 antibody using material from the first immunoprecipitation as input, or vice versa, is a powerful method to detect both modifications at the same gene copies (Voigt, *et al.*, 2013). Here we have shown by this approach that the *PTGS2, BMP2* and *NAMPT* promoters are marked bivalently in the amnion. Moreover, the proportion of H3K27me3-marked copies among the H3K4me3-marked promoters decreased at term compared to early gestation and increased with labour in the case of all three labour-associated genes. At the same time, the proportion of H3K4me3-marked copies among the H3K27me3-marked *PTGS2, BMP2* and *NAMPT* promoters did not change significantly. These results indicate that bivalence is significantly reduced with preference toward activation as gestation advances, and it is re-established during labour. The changes are in good agreement with the marked increase of mRNA abundance during pregnancy and the further modest gene expression changes at labour. Cellular and allelic heterogeneity of histone marks may result in subgroups of promoter copies that are either unmarked or marked monovalently with either the H3K4me3 or the H3K27me3 modification, which, combined with the bivalent group, may produce the variable overall modification levels and gestational differences that correspond poorly to gene expression changes. Collectively, our results suggest that resolution of promoter bivalency toward activation by H3K4me3 is an epigenetic mechanism that may be critically involved in the upregulation of the labour-associated genes at term.

H3K4me3 and H3K27me3 levels are altered by enzymes that establish or erase these histone modifications (Butler, *et al.*, 2012). We have shown that mRNAs encoding six H3K4 methyltransferases (Bogershausen, *et al.*, 2013) and two H3K27me3 demethylases are expressed increasingly in the amnion as gestation advances. At the same time, the principal H3K27 methyltransferase EZH2 showed decreasing abundance at term. Enzyme proteins were detected in the nucleus and the cytoplasm of the epithelial and the mesenchymal cells of the tissue consistently with mRNA expression. The results suggest that expression levels, intracellular localization and target gene selectivity are critical factors that determine the roles of histone modifying enzymes in the epigenetic control of labour-associated genes in the amnion cells. There is evidence in other cell types that SETD1A/KMT2F participates in the regulation of PTGS2 expression and MLL-group H3K4 methyl transferases and the H3K27me3 demethylase JMJD3/KDM6B are involved in the control of BMP2, an established bivalently regulated gene (De Santa, *et al.*, 2007; El Mansouri, *et al.*, 2011). Moreover, JMJD3/KDM6B is induced in inflammation (Kruidenier, *et al.*, 2012), representing a valuable candidate to explore the mechanism of bivalence resolution in the gestational tissues prior to labour. Further work to delineate the involvement of particular histone modifying enzymes in establishing, maintaining or resolving promoter bivalence at critical labour-associated genes may clarify the molecular mechanisms that underlie the epigenetic control of labour onset in women.

Supplementary data

Supplementary data are available at *Molecular Human Reproduction* online.

Acknowledgements

Authors' roles

C.M.M. performed the experiments, the primary data analysis and drafted the Methods section. J.J.H. and M.D.M. contributed to conceptual design and participated in article preparation. H.G.M. supervised patient recruitment, clinical design and data acquisition and contributed to article preparation. T.Z. designed the project, performed the statistical analysis and wrote the article.

Funding

Conflict of interest

The authors have no conflicts of interest to declare.

References

Agger K, Cloos PA, Christensen J, Pasini D, Rose S, Rappsilber J, Issaeva I, Canaani E, Salcini AE, Helin K. UTX and JMJD3 are histone H3K27 demethylases involved in HOX gene regulation and development. *Nature* 2007;**449**:731–734.

Attwood JT, Yung RL, Richardson BC. DNA methylation and the regulation of gene transcription. *Cell Mol Life Sci* 2002;**59**:241–257.

Bennett PR, Rose MP, Myatt L, Elder MG. Preterm labor: stimulation of arachidonic acid metabolism in human amnion cells by bacterial products. *Am J Obstet Gynecol* 1987;**156**:649–655.

Bogershausen N, Bruford E, Wollnik B. Skirting the pitfalls: a clear-cut nomenclature for H3K4 methyltransferases. *Clin Genet* 2013;**83**:212–214.

Butler JS, Koutelou E, Schibler AC, Dent SY. Histone-modifying enzymes: regulators of developmental decisions and drivers of human disease. *Epigenomics* 2012;**4**:163–177.

Challis JR, Lockwood CJ, Myatt L, Norman JE, Strauss JF 3rd, Petraglia F. Inflammation and pregnancy. *Reprod Sci* 2009;**16**:206–215.

Csiszar A, Ahmad M, Smith KE, Labinskyy N, Gao Q, Kaley G, Edwards JG, Wolin MS, Ungvari Z. Bone morphogenetic protein-2 induces proinflammatory endothelial phenotype. *Am J Pathol* 2006;**168**:629–638.

De Santa F, Totaro MG, Prosperini E, Notarbartolo S, Testa G, Natoli G. The histone H3 lysine-27 demethylase Jmjd3 links inflammation to inhibition of polycomb-mediated gene silencing. *Cell* 2007;**130**:1083–1094.

El Mansouri FE, Chabane N, Zayed N, Kapoor M, Benderdour M, Martel-Pelletier J, Pelletier JP, Duval N, Fahmi H. Contribution of H3K4 methylation by SET-1A to interleukin-1-induced cyclooxygenase 2 and inducible nitric oxide synthase expression in human osteoarthritis chondrocytes. *Arthritis Rheum* 2011;**63**:168–179.

Gall Troselj K, Novak Kujundzic R, Ugarkovic D. Polycomb repressive complex's evolutionary conserved function: the role of EZH2 status and cellular background. *Clin Epigenetics* 2016;**8**:55.

Guenther MG, Levine SS, Boyer LA, Jaenisch R, Young RA. A chromatin landmark and transcription initiation at most promoters in human cells. *Cell* 2007;**130**:77–88.

Haddad R, Tromp G, Kuivaniemi H, Chaiworapongsa T, Kim YM, Mazor M, Romero R. Human spontaneous labor without histologic chorioamnionitis is characterized by an acute inflammation gene expression signature. *Am J Obstet Gynecol* 2006;**195**:394.e391–324.

Hirst JJ, Teixeira FJ, Zakar T, Olson DM. Prostaglandin endoperoxide-H synthase-1 and -2 messenger ribonucleic acid levels in human amnion with spontaneous labor onset. *J Clin Endocrinol Metab* 1995;**80**:517–523.

Johnson RF, Mitchell CM, Giles WB, Bisits A, Zakar T. Mechanisms regulating prostaglandin H2 synthase-2 mRNA level in the amnion and chorion during pregnancy. *J Endocrinol* 2006;**188**:603–610.

Johnson RF, Mitchell CM, Giles WB, Walters WA, Zakar T. The in vivo control of prostaglandin H synthase-2 messenger ribonucleic acid expression in the human amnion at parturition. *J Clin Endocrinol Metab* 2002;**87**:2816–2823.

Kim GJ, Romero R, Kuivaniemi H, Tromp G, Haddad R, Kim YM, Kim MR, Nien JK, Hong JS, Espinoza J *et al*. Expression of bone morphogenetic protein 2 in normal spontaneous labor at term, preterm labor, and preterm premature rupture of membranes. *Am J Obstet Gynecol* 2005;**193**:1137–1143.

Kim SY, Romero R, Tarca AL, Bhatti G, Lee J, Chaiworapongsa T, Hassan SS, Kim CJ. miR-143 regulation of prostaglandin-endoperoxidase synthase 2 in the amnion: implications for human parturition at term. *PLoS One* 2011;**6**:e24131.

Kruidenier L, Chung CW, Cheng Z, Liddle J, Che K, Joberty G, Bantscheff M, Bountra C, Bridges A, Diallo H *et al*. A selective jumonji H3K27 demethylase inhibitor modulates the proinflammatory macrophage response. *Nature* 2012;**488**:404–408.

Lappas M. Visfatin regulates the terminal processes of human labour and delivery via activation of the nuclear factor-kappaB pathway. *Mol Cell Endocrinol* 2012;**348**:128–134.

Lins RJ, Mitchell MD. Novel insights into the control of human pregnancy: potential role(s) for epigenetic regulation. *Reproductive Biology Insights* 2008;**1**:3–8.

Livak KJ, Schmittgen TD. Analysis of relative gene expression data using real-time quantitative PCR and the 2(-Delta Delta C(T)) Method. *Methods* 2001;**25**:402–408.

Margueron R, Reinberg D. The Polycomb complex PRC2 and its mark in life. *Nature* 2011;**469**:343–349.

Mitchell C, Johnson R, Bisits A, Hirst J, Zakar T. PTGS2 (Prostaglandin Endoperoxide Synthase-2) expression in term human amnion in vivo involves rapid mRNA turnover, polymerase-II 5'-pausing, and glucocorticoid transrepression. *Endocrinology* 2011;**152**:2113–2122.

Mitchell CM, Johnson RF, Giles WB, Zakar T. Prostaglandin H synthase-2 gene regulation in the amnion at labour: histone acetylation and nuclear factor kappa B binding to the promoter in vivo. *Mol Hum Reprod* 2008;**14**:53–59.

Mitchell BF, Powell WA. Progesterone production by human fetal membranes: an in vitro incubation system for studying hormone production and metabolism. *Am J Obstet Gynecol* 1984;**148**:303–309.

Mitchell CM, Sykes SD, Pan X, Pringle KG, Lumbers ER, Hirst JJ, Zakar T. Inflammatory and steroid receptor gene methylation in the human amnion and decidua. *J Mol Endocrinol* 2013;**50**:267–277.

Ognjanovic S, Bryant-Greenwood GD. Pre-B-cell colony-enhancing factor, a novel cytokine of human fetal membranes. *Am J Obstet Gynecol* 2002;**187**:1051–1058.

Olson DM. The role of prostaglandins in the initiation of parturition. *Best Pract Res Clin Obstet Gynaecol* 2003;**17**:717–730.

Osman I, Young A, Ledingham MA, Thomson AJ, Jordan F, Greer IA, Norman JE. Leukocyte density and pro-inflammatory cytokine expression in human fetal membranes, decidua, cervix and myometrium before and during labour at term. *Mol Hum Reprod* 2003;**9**:41–45.

Pan G, Tian S, Nie J, Yang C, Ruotti V, Wei H, Jonsdottir GA, Stewart R, Thomson JA. Whole-genome analysis of histone H3 lysine 4 and lysine 27 methylation in human embryonic stem cells. *Cell Stem Cell* 2007;**1**:299–312.

Roadmap Epigenomics C, Kundaje A, Meuleman W, Ernst J, Bilenky M, Yen A, Heravi-Moussavi A, Kheradpour P, Zhang Z, Wang J *et al*. Integrative analysis of 111 reference human epigenomes. *Nature* 2015;**518**:317–330.

Roh TY, Cuddapah S, Cui K, Zhao K. The genomic landscape of histone modifications in human T cells. *Proc Natl Acad Sci USA* 2006;**103**:15782–15787.

Romero R, Espinoza J, Kusanovic JP, Gotsch F, Hassan S, Erez O, Chaiworapongsa T, Mazor M. The preterm parturition syndrome. *BJOG* 2006;**113**:17–42.

Ruijter JM, Ramakers C, Hoogaars WMH, Karlen Y, Bakker O, van den Hoff MJB, Moorman AFM. Amplification efficiency: linking baseline and bias in the analysis of quantitative PCR data. *Nucl Acids Res* 2009;**37**: gkp045.

Schuettengruber B, Martinez AM, Iovino N, Cavalli G. Trithorax group proteins: switching genes on and keeping them active. *Nat Rev Mol Cell Biol* 2011;**12**:799–814.

Smith RD, Brown B, Ikonomi P, Schechter AN. Exogenous reference RNA for normalization of real-time quantitative PCR. *Biotechniques* 2003;**34**: 88–91.

Sun Z, Lei H, Zhang Z. Pre-B cell colony enhancing factor (PBEF), a cytokine with multiple physiological functions. *Cytokine Growth Factor Rev* 2013;**24**:433–442.

Teixeira FJ, Zakar T, Hirst JJ, Guo F, Sadowsky DW, Machin G, Demianczuk N, Resch B, Olson DM. Prostaglandin endoperoxide-H synthase (PGHS) activity and immunoreactive PGHS-1 and PGHS-2 levels in human amnion throughout gestation, at term, and during labor. *J Clin Endocrinol Metab* 1994;**78**:1396–1402.

Vastenhouw NL, Schier AF. Bivalent histone modifications in early embryogenesis. *Curr Opin Cell Biol* 2012;**24**:374–386.

Voigt P, Tee WW, Reinberg D. A double take on bivalent promoters. *Genes Dev* 2013;**27**:1318–1338.

Weber M, Hellmann I, Stadler MB, Ramos L, Paabo S, Rebhan M, Schubeler D. Distribution, silencing potential and evolutionary impact of promoter DNA methylation in the human genome. *Nat Genet* 2007;**39**: 457–466.

Xie W, Schultz MD, Lister R, Hou Z, Rajagopal N, Ray P, Whitaker JW, Tian S, Hawkins RD, Leung D *et al.* Epigenomic analysis of multilineage differentiation of human embryonic stem cells. *Cell* 2013;**153**:1134–1148.

Zhang H, Bradley A. Mice deficient for BMP2 are nonviable and have defects in amnion/chorion and cardiac development. *Development* 1996;**122**:2977–2986.